ESCUELA DE INGENIERÍA
DE TELECOMUNICACIÓN Y ELECTRÓNICA

TRABAJO FIN DE MÁSTER

DEVELOPMENT AND VALIDATION OF A MODEL FOR THE CHARACTERIZATION OF NEAR FIELD POWER FLUX OF OPTICAL SOURCES

Program: Máster Universitario en Ingeniería de Telecomunicación

Author: Carlos Guerra Yánez

Tutor: Dr. José A. Rabadán Borges

Dr. Víctor Guerra Yánez

Date: January 2021

Acknowledgements

I would like to express my most sincere gratitude to my tutors for their patience and implication in the development of this project.

I would also like to thank my dear ones, for the unconditional support that I have received in each and every new adventure that I decide to start.

Finally, I would like to show my gratitude to my colleagues at the EITE, for giving some life to these last years in the university.

Resumen en español

Uno de los aspectos fundamentales que se deben cubrir en el proceso de diseño de un sistema de comunicaciones es la caracterización del canal por el que se va a transmitir. En este trabajo se ha abordado el problema de la caracterización de canales ópticos de comunicaciones inalámbricas. Con el fin de obtener un modelo matemáico del comportamiento del canal óptico, se pueden utilizar ecuaciones radiométricas. Si se tienen en cuenta algunas consideraciones sobre la simetría de las fuentes, las ecuaciones radiométricas se pueden simplificar, obteniendo un conjunto de ecuaciones cerradas que se pueden implementar en un entorno de cálculo numérico para simular el comportamiento del canal. En este proyecto se obtienen estas ecuaciones cerradas para las situaciones de simetría de traslación plana, simetría cilíndrica y simetría esférica. Una vez obtenidos los modelos teóricos, para poder validarlos, fue necesario implementar un sistema de medida que permitiera tomar muestras de la señal recibida en diferentes posiciones del espacio. Para implementar este sistema, se utilizó la estructura y el sistema mecánico de una impresora 3D antigua y el sistema de adquisición de datos de un osciloscopio. Una vez implementado el sistema, se llevaron a cabo dos experimentos. Los resultados obtenidos validan el modelo matemático propuesto bajo las condiciones experimentales.

Abstract

Channel characterization is one of the critical steps in the design process of a communication system. In this work, the problem of channel characterization in Optical Wireless Communications is addressed. The optical channel can be modelled with the use of radiometric equations. These radiometric equations can be simplified under certain symmetry conditions to obtain a set of closed equations that can be implemented using a numerical analysis environment to simulate the behavior of the channel. Such a set of equations for the flat, cylindrical and spherical source scenarios is the main theoretical contribution of this project. On the other hand, in order to validate the obtained mathematical models, it was needed a measurement system that could sample the received signal in different spatial positions. This system was implemented using the mechanical system and the structure of a 3D printer and an oscilloscope as the data acquisition interface. After the system was implemented, two experiments were carried out in order to validate the behavior of the obtained mathematical models. The results obtained validate the mathematical model under the conditions of the experiments.

Index of contents

Index of figures

Chapter 1

Introduction

A communication process defines how information is transmitted from one point, the information source, to another, the information user. An effective communication is characterized by the following steps:

- Generation of a message in the source.

- Association of the messages with clearly defined symbols (source coding).

- Modification of the symbols in order to provide integrity, authentication and non-repudiation (encryption, optional).

- Application of an encoding that introduces redundancy in order to be able to detect and correct errors that may occur in the transmission through the medium (channel coding).

- Transmission of the encoded signal through the medium.

- Decoding of the received signal in order to recover the encrypted message.

- Decryption of the recovered code (only if previously encrypted).

- Reconstruction of an estimation of the original signal whose degree of resemblance to the transmitted signal depends on the quality of the system and the characteristics of the medium.

The elements used in each of the steps to achieve such an effective communication form the communication system, as shown in Figure 1.1. The main goal of the communication process is the transportation of some information from the transmitter to the receiver as was previously stated and a good communication system design enables this process. The nature of the information will influence the behavior of the communication system as well as its architecture. When the set of symbols used to represent the message signals is formed by a finite number of elements, the system is said to be a digital communication system.
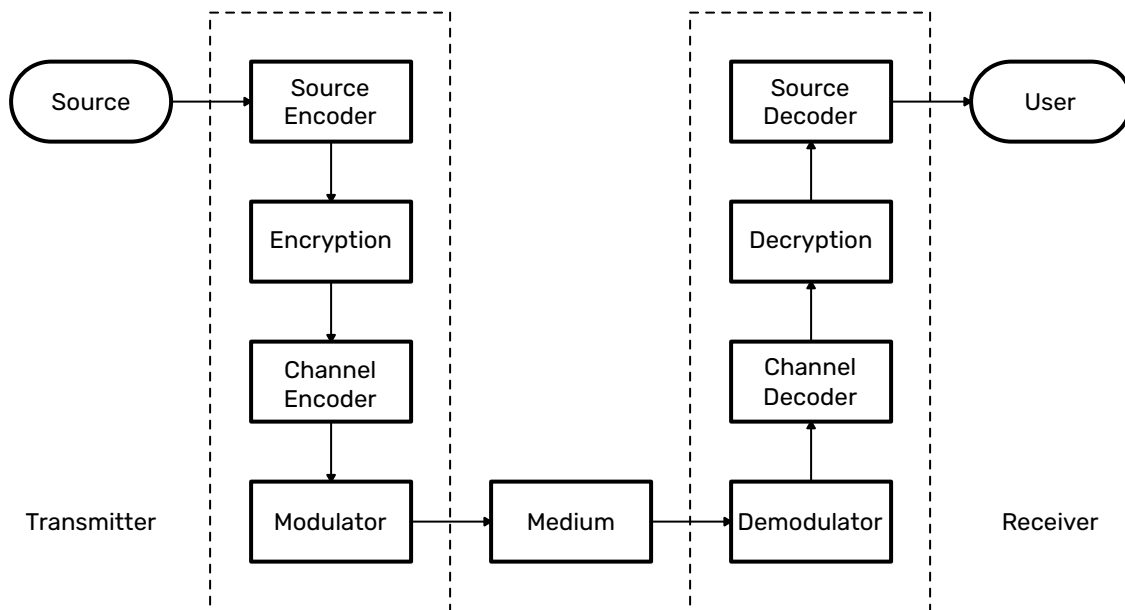
Figure 1.1: Block diagram of a communication system.

Communication processs have been present in an important part of daily life since the last quarter of the twentieth century, this fact and the constant progress in systems engineering justify the research of new paradigms in the design of communication systems and networks. This background has created a situation in which the user of a system expects a high degree of reliability that requires a deep understanding and expertise in the design process of the devices that are part of the communication system. As a consequence, to achieve this reliability demanded by the user, it is necessary to characterize the communication channel (among other aspects) in order to optimize the design or selection of the devices involved in the communication process. This necessity demands the execution of measurement plans and/or simulations of the behavior of the specific channel that will be involved in the communication. Measurement plans provide experimentally exact information about the state of the channel in a certain instant of time, but lack the generalization potential of a close mathematical model. Simulations, on the other side, enable the designer to establish a set of environmental conditions on the mathematical model without the need of investing large amounts of resources. It can be thus concluded that simulations based on good mathematical models of the channel are a basic tool for the engineer that is designing a communication system. When a signal is transported through the medium, it suffers a distortion that degrades the quality of the communication if the receiver is not able to estimate and correct the specific perturbations that have affected the original signal. This distortion is in general represented as an operator acting on the transmitted signal, and one of

the missions of the receiver is to find a way to reverse this degradation process in order to retrieve a signal as similar as possible to the transmitted signal. The space of time-dependent signals that is generally used when characterizing communication systems is the space of square-integrable signals, L^2. If the signal emitted by the transmitter is given the name $s_{Tx}(t)$, the received signal $s_{Rx}(t)$ is given by

$$s_{Rx}(t) = T\{s_{Tx}(t)\} \tag{1.1}$$

Where $T\{\cdot\}$ is the channel operator that was previously introduced. When the channel can be modelled as a linear, shift-invariant system, the $T\{\cdot\}$ operator becomes a convolution operator

$$T\{s_{Tx}(t)\} = \int_{\infty}^{\infty} h(t-\tau)\, s_{Tx}(\tau)\, \mathsf{d}\tau \tag{1.2}$$

and the behavior of the system is determined by the convolution kernel $h(t)$. In the general scenario, the waveform of the signal $s_{Tx}(t)$ depends on the used modulation scheme and coding, and it usually consists on a carrier signal whose parameters are modified to introduce the information of the source (modulation). The most widely used carriers signals in telecommunications are free and guided electromagnetic sinusoidal waves, which can be modulated by modifying their physical parameters, amplitude and instantaneous phase, for instance. Several different modulation schemes have been proposed over the history of telecommunications to deal with the problems inherent to every part of the electromagnetic spectrum and every specific scenario. In this work, the focus will be put on the optical region of the spectrum, where the generation and detection of phase and amplitude modulations becomes a hard task [1], with an exception on certain optical fiber systems which use interferometric tools to implement phase modulations.
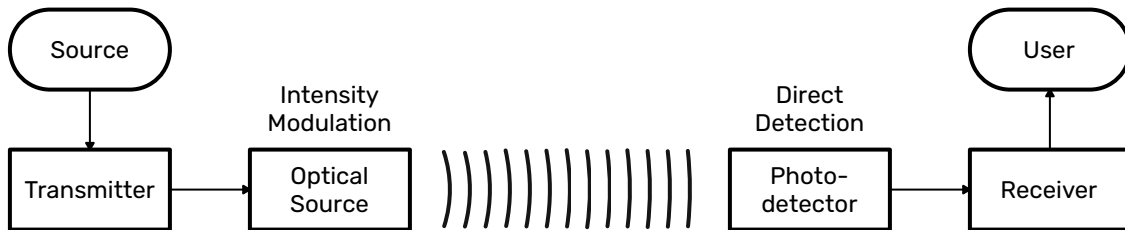
Figure 1.2: Block diagram of an IM/DD communication system.

Some of the most common modulation schemes in optical communications are based on the modification of the instantaneous power of the emitted optical

signal, which can be done by simply modifying the polarization of an electro-optic transducer. On the receiver side, this power can be directly recovered with the use of a photodetector. This scheme is called Intensity Modulation / Direct Detection (IM/DD), a block diagram for IM/DD is shown in Figure 1.2. The simplest modulation scheme in this scenario is called On-Off Keying (OOK) and is equivalent to a binary-ASK baseband signal with one of the amplitudes fixed to zero. The optical power of an OOK-modulated IM/DD signal is

$$P_{Tx}^n (t) = a_n P_0 \Pi \left(\frac{t - T/2}{T} \right)$$
(1.3)

Where a_n can take the values 0 or 1 depending on the symbol that is being transmitted, P_0 determines the optical power of the "On" symbol, T determines the duration of one symbol, and $\Pi(t)$ is a square pulse signal of unitary width and centered at zero. Additionally, it is a common practice to use multicarrier modulations with different wavelengths (multiple optical sources) in an scheme that is called Wavelength Division Multiplexing (WDM), as well as some modified versions of Orthogonal Frequency Division Multiplexing (OFDM) in order to achieve higher data rates [2, 3]. Several classifications of optical communication systems have been proposed according to different parameters, one of those classifications is based on the enabling technology. This classification acknowledges Visible Light Communications (VLC), Optical Camera Communications (OCC), Light Fidelity (LiFi), Free Space Optical Communications (FSOC) and Light Detection And Ranging (LiDAR) as the main underlying technologies of Optical Wireless Communications (OWC) and Positioning [4]. In particular, VLC is a potential solution to certain problems of current networks such as the congestion of the RF spectrum or the necessity of higher data rates and capacities of the systems [5]. Some of the main applications of VLC are in Vehicle-to-Vechicle (V2V) and underwater communications, network access and services in hospitals and healthcare environments, and as Wireless Local Area Network (WLAN) access technologies [6]. This work will be focused on the physical part of channel modelling for a certain kind of VLC systems, with a possible extension to OCC models. In the OWC scenario, the channel is formed by the different propagation paths and is dependent on the shape of the optical source and the shape of the active region of the photodetector, as well as the geometry of the environment where the communication is taking place. When the dimensions of the source and the receiver are negligible compared to the dimensions of the environment, the channel impulse response is characterized as

$$h(t) = h_{LoS}(t) + h_{NLoS}(t)$$
(1.4)

Where the direct link term is given by an attenuation and a delay

$$h_{LoS}(t) = \frac{A_{Rx}(m+1)}{2\pi R^2} \cos(\psi_{Tx})^m \cos(\psi_{Rx}) T_s(\psi_{Rx}) g(\psi_{Rx}) \delta\left(t - \frac{R}{c}\right)$$
(1.5)

and the NLoS term is an infinite sum of integrals that models the reflections produced on the room. In low bandwdith applications, only the DC term must be considered, and the received power can be calculated using the simple formula

$$P_{Rx} = P_{Tx} \left[H_{LoS} \left(0 \right) + H_{NLoS} \left(0 \right) \right] \tag{1.6}$$

Where the $H_{LoS} \left(0 \right)$ and the $H_{NLoS} \left(0 \right)$ are the path losses of the paths given by the DC term of the Fourier transform of the corresponding channel impulse responses. The study of OWC systems considering near field effects is in an initial stage, and the main focus of the available literature has been put in the behavior of optical sources at very short distances [7], and not in the characterization of the communication channel , this is one of the goals of the present work 1.3. The characterization of the physical behavior of the transmitter is a fundamental step in the design process of a communication system. In the field of optical communications, the characterization of these emitters encompasses the dynamic modelling of the device (time-response) and the spatial configuration of the emitted signal (directivity). The characterization of the dynamic behavior can be obtained by any of the methods that exist and have been traditionally used for communications systems. On the other hand, the measurement of the spatial distribution of the radiated energy poses a slightly more difficult problem because in order to obtain a faithful set of measures, it is necessary to develop an instrumentation system that allows a measurement process on a 3D-grid of the space. Some approximations can be done when the optical source is considered to be a point source, leading to a characterization of the source through the use of a radiant intensity function (which only depends on the direction towards where the source is radiating its energy), but this is not in general the case when dealing with sources consisting of large panels or rods, where the source cannot be modelled by a radiant intensity, and a radiance function must be defined.

1.1   Problem description

The main target of this work is to provide a characterization mechanism of the radiative power transfer produced by optical sources, defined over a 2-manifold in the near field 1.3, where the geometry of the source cannot be neglected (but ignoring the effects of reflective surfaces in the environment for simplicity) for different cases. The document will follow a deductive approach, stating at first the general time-dependent radiative transfer problem and assuming some key simplifications thereafter.
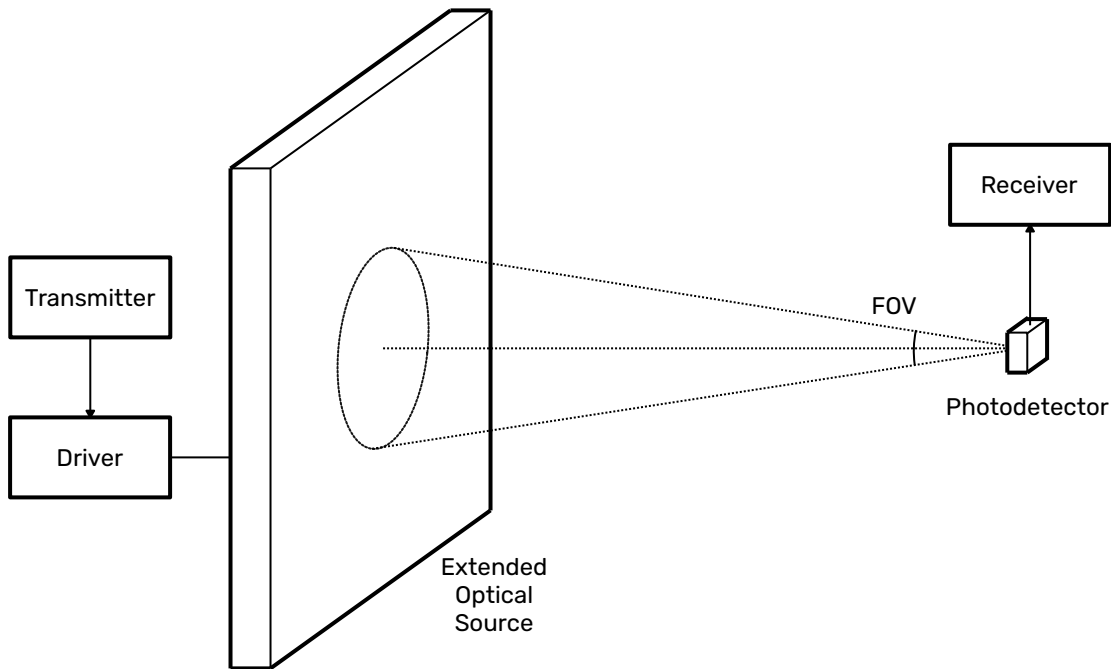
Figure 1.3: Schematic of the near field scenario.

In particular, the static scenario is of interest, as it can be used to determine the channel DC gain as a function of position for a point receiver. Those effects of the geometry of the source should be considered when analyzing certain near field OWC links. A brief description of some applications of the extended source model will be carried out in this work. The last part of this document consists on an exposition of the different experiments that are necessary in order to determine the validity of the mathematical models, as well as the obtained results for an implementation of one of those experimental systems.

1.2   Objectives

The general objectives of this project can be described briefly as: "to study the effects of the geometry of an optical source on the irradiance map and to design experimental procedures to verify the obtained models". The following numbered objectives give a more precise formulation of this idea.

01 To study the current methodologies used in the characterization of optical sources.

02 To study the theoretical background needed in order to confront the problem of the characterization of transmitted power using radiometric techniques.

03 To define a theoretical model for the transmission of optical power in different scenarios.

04 To propose the use of the obtained model as a framework to study certain characteristics of OWC channels.

05 To define a methodology for the characterization of the irradiance of constant optical sources in the near field.

06 To design an experimental system that partially implements the characterization methodology.

07 To obtain experimental data to contrast with the theoretical model.

1.3   Petitioner

The present document is claimed by the Universidad de Las Palmas de Gran Canaria as a requirement to the obtention of the title of Máster Universitario en Ingeniería de Telecomunicación as it is stated in the VERIFICA document of the degree. This document corresponds to the subject *Trabajo Fin de Master* of the second year of the program of this Master's degree.

1.4   Document structure

The document is structured as follows. In Chapter 1 the initial motivation of the project was presented and the objectives were stated. In Chapter 2, a literature review of channel characterization for OWC channels is exposed, focusing on indoor VLC systems and extended sources. In Chapter 3 the mathematical models for the different source geometries are developed. Chapter 4 focuses on potential applications for short range VLC communications that could make use of the proposed models. In Chapter 5 some designs of experimental validation systems are analyzed, comparing their advantages and disadvantages. In Chapter 6 a validation system is selected from the previous analysis and its implementation is documented, the study of the experimental error is also developed in this chapter. In Chapter 7 the obtained experimental results are shown and compared with the simulations done. Chapter 8 synthesizes the main results of this project, and some future lines are proposed.

Chapter 2

State of the art

Channel characterization is a well-studied field, and therefore the literature is extensive. Some of the classical techniques for channel characterization based on the excitation of the channel by a known signal [8–10] are being challenged by blind or AI-based methodologies [11, 12]. It is necessary to differentiate between SISO, MISO and MIMO channels when considering the channel characterization and estimation techniques to be used [13]. In this project, only SISO channels will be studied, but the model could be generalized to consider MISO or MIMO scenarios. The classical models for VLC channels usually consider point sources and receivers [14–17], which makes sense in far-field scenarios. Ray tracing algorithms are used in order to develop computer programs that simulate the behavior of VLC channels, but the associated computational complexity makes them impractical when the geometry of the environment is very complex or more than a few bounces are needed in order to obtain good results [18]. Some statistical models have been proposed for the main parameters of VLC channels [19, 20], and some models consider random orientation of the receiver [21, 22]. Covering a different range of situations, some adaptive models have been proposed for VLC scenarios where there are dynamical elements [23] as well as models that reduce the complexity by considering that each ray can only generate one scattered ray in each collision (photon mapping model) [24]. Three far field conditions have been determined for LED sources depending on technical parameters of the device such as lens and chip shape, the position of the chip or packaging errors [25, 26]. The determination of the far field conditions is essential for the analysis of arrays of optical sources, which behave as extensive sources. In this scenario, modelling the radiation pattern of the optical sources is the first step in the characterization of the array, which can be obtained by defining the radiance function. LED devices have been traditionally treated as generalized lambertian sources, but some studies have shown the error inherent in the far field lambertian approximation [27, 28], and some alternative radiation patterns have been proposed such as linear combinations of gaussian and cosine power functions [29]. The properties of the radiation pattern of optical sources have been shown to affect the performance of OWC channels [30]. An elementary analysis of the irradiance distribution of an LED in the near field has been recently

published [7]. Similar studies have been done in order to determine the radiation pattern of OLED sources, their impact on OWC channels and some applications in detection [31, 32], but these results should be analyzed with caution, because an extensive source cannot be characterized by a radiant intensity function, the radiant intensity function is defined for a point source, which is not the case. Regarding the design procedure of optical source arrays, some works have been published for LED arrays that generate uniform irradiance at a given distance, first in a general way [33], as well as considering imperfect radiation patterns [34], and spherical arrays [35, 36]. In addition, some procedures using mathematical programming techniques have been proposed [37–39]. In the case of nonuniform irradiance distributions, an elementary scheme was proposed [40], but no closed procedure has been presented, and no experimental results have been obtained. This is one of the main potential applications of the theoretical framework developed in this document. Some work has been published recently on the characterization of the received power from a distribution of tilted flat emitter surfaces [41], but further research is needed in order to develop models for scenarios where the dimensions of the optical source is not negligible, which is the focus of this work.

Chapter 3

Optical power transmission modelling

In this chapter, the power transmission problem is solved for several symmetrical scenarios. In the first section, the general problem is posed, and the fundamental equations are derived. In the rest of the chapter, the different symmetrical configurations are analyzed (flat, cylindrical and spherical sources), and the simplified equations are derived for every case. These simplified equations, which are based on the convolution of the functions that define the source with a kernel that can be defined through the parameters of the problem, are the main theoretical contribution of this work.

3.1   General description of the problem

When an IM/DD scheme is being used in an optical communications system, the electrical current generated in the photodetector, whose responsivity is given by the function $\Re(\lambda)$ can be modelled as [42]

$$I_{Rx}(t) = \int_0^\infty \Phi_{Rx}(\lambda, t)\, \Re(\lambda)\, \mathsf{d}\lambda \qquad (3.1)$$

The behavior of the channel depends on the optical power captured by the photodetector and the responsivity of the photodetector to every wavelength in the spectrum of the incident radiation. The received spectral power density, $\Phi_{Rx}(\lambda, t)$, in the general scenario (Figure 3.1) is given by

$$\Phi_{Rx}(\lambda, t) = \iint_{S_{Tx}(t)} \iint_{\Omega_{Rx}(t)} L_{Tx}\left(u, v, \psi_{Tx}, \xi_{Tx}, \lambda, t - \frac{R}{c}\right)\cos(\psi_{Tx})\,\mathsf{d}\Omega \mathsf{d}S \qquad (3.2)$$

Where L_{Tx} is the radiance of the source, S_{Tx} is the surface where the source is defined, Ω_{Rx} is the solid angle where the receiver is located with respect to every receiver position, u and v are the parameters used to define the positions of the source manifold, given by $\mathbf{r}' = x'(u, v)\,\mathbf{u}_x + y'(u, v)\,\mathbf{u}_y + z'(u, v)\,\mathbf{u}_z$, ψ_{Tx} is the angle
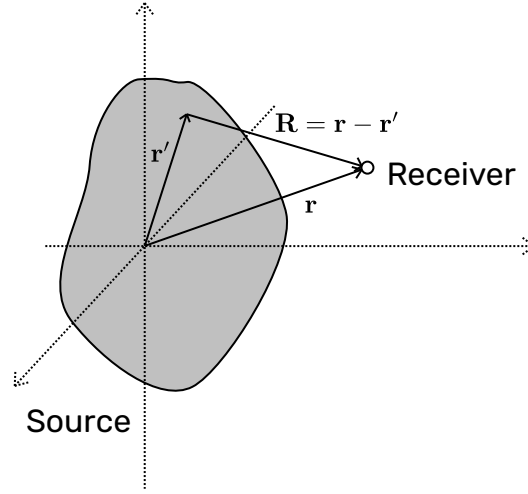
Figure 3.1: Geometric scenario for the radiometric problem.

between every ray and the normal direction at every point over the source and ξ_{Tx} is the azimuth angle for every ray respect to a reference direction which has to be established. If the surface of the receiver is well defined,S_{Rx} , the integral in (3.2) can be expressed alternatively as

$$\Phi_{Rx}\left(\lambda, t\right) = \iint_{S_{Tx}(t)} \iint_{S^{Rx}(t)} L_{Tx} \frac{\cos\left(\psi_{Tx}\right)\cos\left(\psi_{Rx}\right)\mathrm{d}S'\mathrm{d}S}{R^2} \tag{3.3}$$

where ψ_{Rx} is the angle of the ray respect to the normal at every point located on the receiver surface. The radiance of a given optical source is expressed as

$$L_{Tx}\left(u, v, \psi_{Tx}, \xi_{Tx}, \lambda, t\right)\cos\left(\psi_{Tx}\right) = M_{Tx}\left(u, v, \lambda, t\right)t_{Tx}\left(u, v, \psi_{Tx}, \xi_{Tx}, \lambda\right) \tag{3.4}$$

Where the term M_{Tx} defines the retarded exitance of the source and t_{Tx} defines the radiation pattern of the source. In this work, all sources will be considered generalized lambertian [43], so (3.3) reduces to

$$\Phi_{Rx}\left(\lambda, t\right) = \frac{m+1}{2\pi} \iint_{S_{Tx}(t)} \iint_{S_{Rx}(t)} M_{Tx} \frac{\cos^m\left(\psi_{Tx}\right)\cos\left(\psi_{Rx}\right)\mathrm{d}S\mathrm{d}S'}{R^2} \tag{3.5}$$

Equation (3.5) considers the temporal effects of propagation by introducing the retarded exitance of the source. When dealing with absorbent media with constant attenuation factor, (3.5) can be modified by adding an exponential attenuation factor with a wavelength dependent coefficient, $\alpha\left(\lambda\right)$, to include the effects predicted by Beer's law [44]

$$\Phi_{Rx}\left(\lambda, t\right) = \frac{m+1}{2\pi} \iint_{S_{Tx}(t)} \iint_{S_{Rx}(t)} e^{-\alpha(\lambda)R} M_{Tx} \frac{\cos^m\left(\psi_{Tx}\right)\cos\left(\psi_{Rx}\right)\mathrm{d}S\mathrm{d}S'}{R^2} \tag{3.6}$$

In the general scenario, the evaluation of (3.3) needs a cautious consideration of the shadowing effects that could occur (as well as diffraction if the dimensions of the problem are in the order of magnitude of the wavelength), the scattering processes, as well as the effects of the optical systems that could be used in the receiver side in order to increase the received power (optical gain). The effects of the optical systems will be considered in a function, $g\left(\psi_{Rx}, \xi_{Rx}\right)$, which will be in general symmetrical respect to rotations in the optical axis, thus eliminating the dependence on the ξ variable. In this work, the receiver surface will be considered to be small compared to the dimensions of the problem, so the point receiver approximation can be used. This situation leaves the problem reduced to the analysis of receivers considered as small open manifolds (with an optical system)

$$\Phi_{Rx}\left(\lambda, t\right) = \frac{A_{Rx}\left(m+1\right)}{2\pi} \iint_{S_{Tx}(t)} e^{-\alpha(\lambda)R} M_{Tx} \frac{\cos^{m}\left(\psi_{Tx}\right)\cos\left(\psi_{Rx}\right)g\left(\psi_{Rx}\right)\mathsf{d}S}{R^2} \quad (3.7)$$

and the analysis of receivers considered as small closed manifolds (any incident ray is normal to the receiver surface, and no optical system is considered)

$$\Phi_{Rx}\left(\lambda, t\right) = \frac{A'_{Rx}\left(m+1\right)}{2\pi} \iint_{S_{Tx}(t)} e^{-\alpha(\lambda)R} M_{Tx} \frac{\cos^{m}\left(\psi_{Tx}\right)\mathsf{d}S}{R^2} \quad (3.8)$$

In the following sections, some simplifications will be made in order to reduce (3.7) and (3.8) to more simple and practical expressions in specific scenarios. The analysis presented until now might seem incomplete because not every source can be considered a differentiable manifold. However, when discrete sources distributed along a 2D-mesh are considered, their positions are given by the pairs of points $\left(u_{(i,j)}, v_{(i,j)}\right)$ which define spatial points over the surface. In this case, the presented model is also applicable, considering an open manifold receiver, the total received power could be modelled as

$$\Phi_{Rx}\left(\lambda, t\right) = A_{Rx} \sum_{i}\sum_{j} P_{(i,j)}\left(\lambda, t - \frac{R_{(i,j)}}{c}\right) t_{Tx}\left(\psi_{(i,j)}, \xi_{(i,j)}\right) \frac{\cos\left(\psi_{(i,j)}\right)g\left(\psi_{(i,j)}\right)}{R^2_{(i,j)}} \quad (3.9)$$

By identification of (3.9) and (3.4), a radiance function can be defined for every source element as

$$L_{(i,j)} = \frac{P_{(i,j)}\left(\lambda, t - \frac{R_{(i,j)}}{c}\right) t_{Tx}\left(\psi_{(i,j)}, \xi_{(i,j)}\right)}{\cos\left(\psi_{(i,j)}\right)} \delta\left(u - u_{(i,j)}\right)\delta\left(v - v_{(i,j)}\right) \quad (3.10)$$

And the total radiance of the array of sources would be

$$L_{Tx} = \sum_{i}\sum_{j} L_{(i,j)} \quad (3.11)$$

In this work the behavior of discrete arrays of optical sources will be analyzed by considering an averaging process similar to the one used in electromagnetic theory to study macroscopic systems composed of microscopic elements. This model is justified whenever the distances between source elements are negligible compared to the distances between the source and the receiver. This would be the case of a LED display, a lighting panel or the surface of a hot body. In some practical scenarios, a single extended source could be considered to have independent time and spatial behavior, thus its time-varying exitance could be described as

$$M_{Tx}(u, v, \lambda, t) = P_{Tx}(\lambda, t) I_{Tx}(u, v) \tag{3.12}$$

Where the term P_{Tx} describes the time behavior of the source and I_{Tx} describes its spatial power distribution, with the following normalization condition

$$\iint_{S_{Tx}} I_{Tx}(u, v) \, \mathsf{d}S = 1 \tag{3.13}$$

Considering this and fixing the source in a certain position in space (static source), (3.7) can be expressed as

$$\Phi_{Rx}(\lambda, t) = P_{Tx}(\lambda, t) * h(\lambda, t) \tag{3.14}$$

Where $h(\lambda, t)$ is a convolution kernel given by

$$h(\lambda, t) = \frac{A_{Rx}(m+1)}{2\pi} \iint_{S_{Tx}} e^{-\alpha(\lambda)R} I_{Tx} \frac{\cos^m(\psi_{Tx}) \cos(\psi_{Rx}) g(\psi_{Rx})}{R^2} \delta\left(t - \frac{R}{c}\right) \mathsf{d}S \tag{3.15}$$

The DC gain of the channel can be calculated then as

$$H(\lambda, 0) = \frac{A_{Rx}(m+1)}{2\pi} \iint_{S_{Tx}} e^{-\alpha(\lambda)R} I_{Tx} \frac{\cos^m(\psi_{Tx}) \cos(\psi_{Rx}) g(\psi_{Rx})}{R^2} \mathsf{d}S \tag{3.16}$$

If the behavior of the channel can be approximated by the DC response, the received power flux would simply be

$$\Phi_{Rx}(\lambda, t) = P_{Tx}(\lambda, t) H(\lambda, 0) \tag{3.17}$$

And the channel delay spread

$$\tau_{RMS}(\lambda) = \sqrt{\frac{\int_0^\infty (t - \bar{\tau}(\lambda))^2 h(\lambda, t) \, \mathsf{d}t}{\int_0^\infty h(\lambda, t) \, \mathsf{d}t}} \tag{3.18}$$

with

$$\bar{\tau}(\lambda) = \frac{\int_0^\infty t h(\lambda, t) \, \mathsf{d}t}{\int_0^\infty h(\lambda, t) \, \mathsf{d}t} \tag{3.19}$$

Equation (3.15) shows that the dynamic behavior of the channel depends on the characteristics of the medium, as well as the position and orientation of the source and the receiver, and the geometry of the receiver, thus a simulation model to obtain the channel parameters could be implemented taking this into considerations. A further approach to a complete model would include the behavior of the photodiode as a part of the communication channel. The implemented model in this point would be a very complex one, but in the following sections, some simplifications that can be applied in certain scenarios will be derived and explained. There is a simplification that will be applied to every model obtained in the following sections, the source will be considered to be monochromatic, and thus, the wavelength will not be considered as a parameter of the model. This can be done without loss of generality, if the spectral behavior of the source needs to be considered, the only changes that would The main result of this section is the set of mathematical models that can be obtained for the different source geometries and receiver orientations.

3.2   Sources defined by monge coordinates

Consider that the manifold that defines the optical source is given as a vector of monge coordinates, $\boldsymbol{r}_{Tx} = (x', y', f(x', y'))$ as shown in Figure 3.2 (for further detail refer to Appendix A.
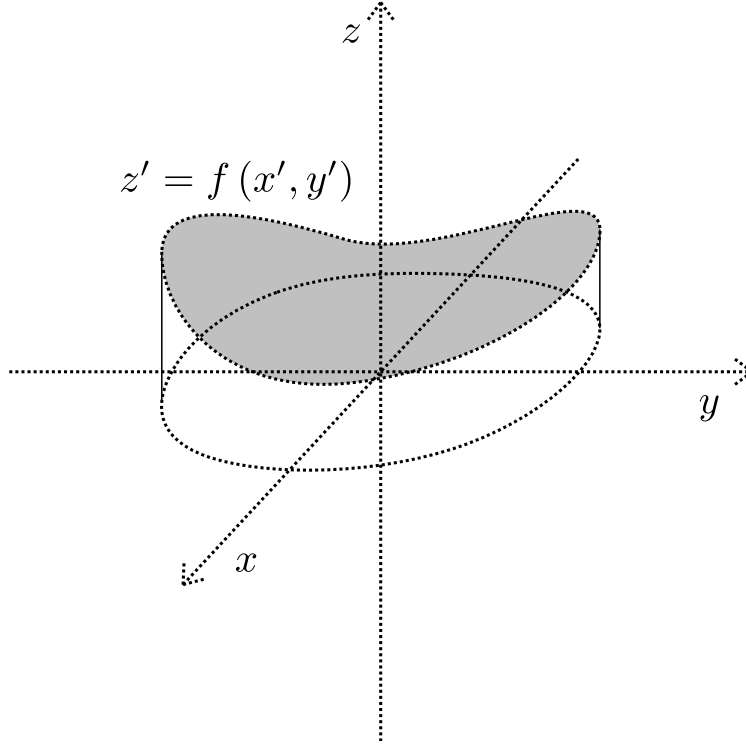
Figure 3.2: Manifold defined by a set of monge coordinates.

The receiver is in the position given by $\boldsymbol{r}_{Rx} = (x, y, z)$ and the orthogonal vector of the source manifold can be calculated as

$$\boldsymbol{n}_{Tx} = \frac{\boldsymbol{u}_z - f_{x'}\boldsymbol{u}_x - f_{y'}\boldsymbol{u}_y}{\sqrt{1 + (f_{x'})^2 + (f_{y'})^2}} \tag{3.20}$$

The cosine of the incident angle of the ray along the source is given by

$$\cos(\psi_{Tx}) = \boldsymbol{n}_{Tx} \cdot \frac{\boldsymbol{r}_{Rx} - \boldsymbol{r}_{Tx}}{||\boldsymbol{r}_{Rx} - \boldsymbol{r}_{Tx}||} \tag{3.21}$$

The orientation of the receiver is given by the following unitary vector

$$\boldsymbol{n}_{Rx} = \sin(\alpha)\cos(\beta)\boldsymbol{u}_x + \sin(\alpha)\sin(\beta)\boldsymbol{u}_y - \cos(\alpha)\boldsymbol{u}_z \tag{3.22}$$

And the cosine of the incident angle of the ray on the receiver can be expressed as

$$\cos\left(\psi_{Rx}\right) = \boldsymbol{n}_{Tx} \cdot \frac{\boldsymbol{r}_{Tx} - \boldsymbol{r}_{Rx}}{||\boldsymbol{r}_{Rx} - \boldsymbol{r}_{Tx}||} \tag{3.23}$$

The geometry of the surface also has a direct effect on the integral as a deformation of the differential area element. The transformation of the area element respect to the euclidean case is given by the determinant of the first fundamental form, and in the case of a manifold given by a set of monge coordinates it can be computed as

$$\mathsf{d}S = \sqrt{g_{11}g_{22} - g_{12}^2}\mathsf{d}x'\mathsf{d}y' = \left(1 + (f_{x'})^2 + (f_{y'})^2\right)\mathsf{d}x'\mathsf{d}y' \tag{3.24}$$

With all this in mind, the convolution kernel (3.15) can be expressed in closed–form as a function of the receiver position, orientation and time, the only requisite is that the expression that defines the source's surface as a function of the monge coordinates x' and y' must be known.

3.2.1 Flat sources

In the case of a flat source located on the plane $z' = 0$, the monge coordinates are given by a local coordinate system of the form

$$f\left(x', y'\right) = 0 \tag{3.25}$$

the geometry of the source is shown in Figure 3.3. The cosine of the elevation angle from the source is given by

$$\cos\left(\psi_{Tx}\right) = \frac{z}{\sqrt{z^2 + \left(x - x'\right)^2 + \left(y - y'\right)^2}} \tag{3.26}$$

The surface differential in this case is given as

$$\mathsf{d}S = \mathsf{d}x'\mathsf{d}y' \tag{3.27}$$

Then the integral operator in (3.15) becomes shift-invariant along the plane where the source is defined, and this enables a further simplification of the integral to a 2D-convolution operator over the x and y variables which can be efficiently computed using classical image processing techniques

$$h\left(x, y, z, \boldsymbol{n}_{Rx}, t\right) = I_{Tx}\left(x, y\right) * k\left(x, y, z, \boldsymbol{n}_{Rx}, t\right) \tag{3.28}$$

The convolution kernel $k\left(x, y, z, \boldsymbol{n}_{Rx}, t\right)$ is given by

$$k\left(x, y, z, \boldsymbol{n}_{Rx}, t\right) = \frac{A_{Rx}\left(m + 1\right)}{2\pi}\frac{\cos\left(\psi_{Tx}\right)^m \cos\left(\psi_{Rx}\right)g\left(\psi_{Rx}\right)}{||\boldsymbol{r}^{Rx}||}\delta\left(t - \frac{||\boldsymbol{r}^{Rx}||}{c}\right) \tag{3.29}$$
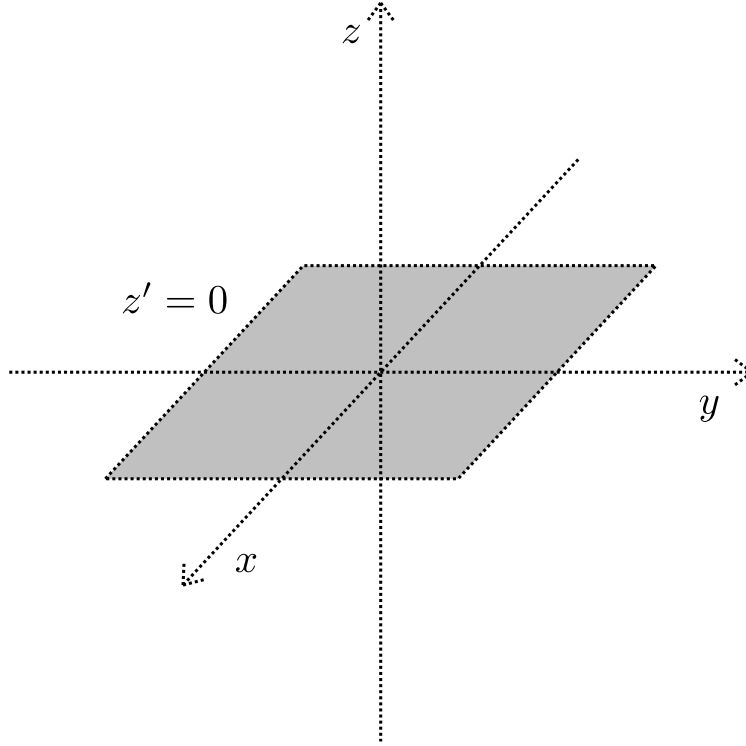
Figure 3.3: Geometry of a flat source.

In a low rate communication scenario, the behavior of the system can be modelled considering a slow varying approximation, and (3.29) can be integrated in time to obtain an even simpler expression

$$K\left(x, y, z, \boldsymbol{n}_{Rx}\right) = \frac{A_{Rx}\left(m+1\right)}{2\pi} \frac{\cos\left(\psi_{Tx}\right)^{m} \cos\left(\psi_{Rx}\right) g\left(\psi_{Rx}\right)}{||\boldsymbol{r}^{Rx}||} \tag{3.30}$$

The DC response can be obtained as a function of the receiver position and orientation.

$$H\left(x, y, z, \boldsymbol{n}_{Rx}, 0\right) = I_{Tx}\left(x, y\right) * K\left(x, y, z, \boldsymbol{n}_{Rx}\right) \tag{3.31}$$

The irradiance generated by a stationary source (no dynamic behavior) over a plane located at a distance z respect to the source plane can be easily calculated using this expression

$$E\left(x, y, z\right) = \frac{P_{Tx} H\left(x, y, z, \boldsymbol{n}_{Rx}, 0\right)}{A_{Rx}} \tag{3.32}$$

The scenario where the receiver is directly pointed towards the source is of particular interest, $\boldsymbol{n}_{Rx} = -\boldsymbol{u}_z$, in this case (3.29) reduces to

$$k\left(x,y,z,t\right) = \frac{A_{Rx}\left(m+1\right)}{2\pi}\frac{z^{m+1}g\left(x,y,z\right)}{\left[z^2+x^2+y^2\right]^{\frac{m+3}{2}}}\delta\left(t-\frac{\sqrt{z^2+x^2+y^2}}{c}\right) \tag{3.33}$$

and thus (3.30) reduces to

$$K\left(x,y,z\right) = \frac{A_{Rx}\left(m+1\right)}{2\pi}\frac{z^{m+1}g\left(x,y,z\right)}{\left[z^2+x^2+y^2\right]^{\frac{m+3}{2}}} \tag{3.34}$$

With the use of the expressions obtained in this section, the problem of estimating the received power or the irradiance map for a slow-varying flat source is reduced to the convolution of the kernel defined by equation (3.29) with the normalized exitance function of the source, $I_{Tx}\left(x,y\right)$ to obtain the DC response. After this convolution has been calculated, using direct computation methods, or taking advantage of the properties of the Fourier Transform, the received power and the irradiance map can be estimated through equations (3.17) and (3.32).

3.2.2 Cylinder-section sources

Now consider a source with nonzero curvature along one axis (this could be an advertising panel or an OLED TV) whose monge coordinates are given by

$$f\left(x',y'\right) = \sqrt{R^2-x'^2}-a \tag{3.35}$$

The shape of this kind of source is shown in Figure 3.4. It can be noticed that $a < R$, and the source is only defined inside the strip $|x'| \le \sqrt{R^2-a^2}$ and the normal vector is given by

$$\boldsymbol{n}_{Tx} = \frac{\sqrt{R^2-x'^2}}{R}\boldsymbol{u}_z + \frac{x'}{R}\boldsymbol{u}_x \tag{3.36}$$

the cosine of the elevation angle from the source is given by

$$\cos\left(\psi_{Tx}\right) = \frac{\sqrt{R^2-x'^2}\left(z-f\left(x',y'\right)\right)+x'\left(x-x'\right)}{R\sqrt{\left(z-f\left(x',y'\right)\right)^2+\left(x-x'\right)^2+\left(y-y'\right)^2}} \tag{3.37}$$

The area differential in the cylindrical scenario is given as

$$\mathsf{d}S = \frac{R}{\sqrt{R^2-x'^2}}\mathsf{d}x'\mathsf{d}y' \tag{3.38}$$

The invariance on the x-coordinate of the source has been broken by the presence of a curvature along that dimension in the surface defined by the source. However, in this case, there exists invariance in the y-axis, and the integral operator can be reduced to an integral of the result of a convolution in the y-axis.

$$h\left(x,y,z,\boldsymbol{n}_{Rx},t\right) = \int_{-\sqrt{R^2-a^2}}^{\sqrt{R^2-a^2}}\left[I_{Tx}\left(x',y\right)*k\left(x',x,y,z,\boldsymbol{n}_{Rx},t\right)\right]\mathsf{d}x' \tag{3.39}$$
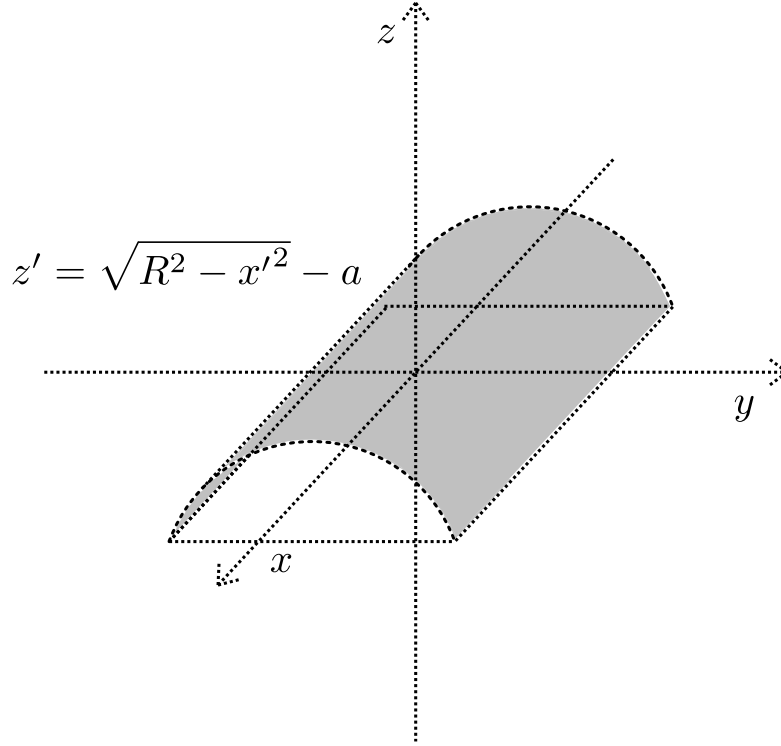
Figure 3.4: Geometry of a cylinder section source.

Where the function $k\left(x', x, y, z, \boldsymbol{n}_{Rx}, t\right)$ is the same as (3.29) but considering the new cylindrical geometry described, the integral left lies in a bounded interval, so any numerical integration method can be used to evaluate it after calculating the convolutions in the y-axis.

3.2.3   Sphere-section sources

Now consider a source with spherical shape (which could be the lighting source of a room), in this case, the set of local coordinates of the source woud be of the form

$$f\left(x', y'\right) = \sqrt{R^2 - x'^2 - y'^2} - a \tag{3.40}$$

With $a < R$, the source is defined inside the circle $x'^2 + y'^2 \leq R^2 - a^2$. The geometry would be as shown in Figure 3.5 and the normal vector from the source is given by

$$\boldsymbol{n}_{Tx} = \frac{\sqrt{R^2 - x'^2 - y'^2}}{R}\boldsymbol{u}_z + \frac{x'}{R}\boldsymbol{u}_x + \frac{y'}{R}\boldsymbol{u}_y \tag{3.41}$$

The cosine of the elevation angle is then given by
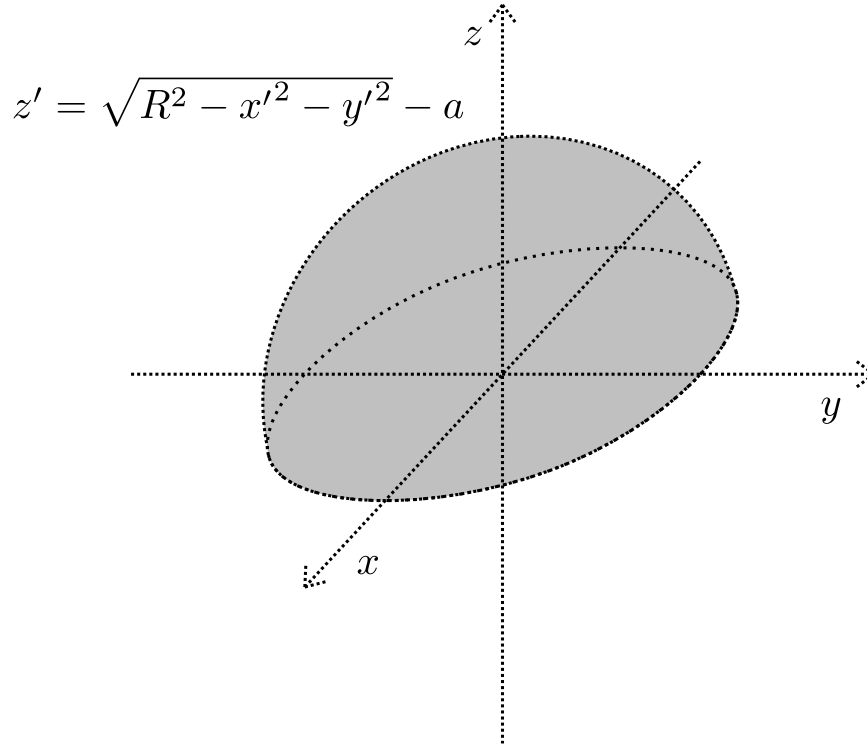
Figure 3.5: Geometry of a spherical section source.

$$\cos\left(\psi_{Tx}\right) = \frac{\sqrt{R^2 - x'^2 - y'^2}\left(z - f\left(x', y'\right)\right) + x'\left(x - x'\right) + y'\left(y - y'\right)}{R\sqrt{\left(z - f\left(x', y'\right)\right)^2 + \left(x - x'\right)^2 + \left(y - y'\right)^2}} \tag{3.42}$$

The area differential in the spherical scenario is given as

$$\mathsf{d}S = \frac{R}{\sqrt{R^2 - x'^2 - y'^2}}\mathsf{d}x'\mathsf{d}y' \tag{3.43}$$

In this case, there is no invariance in the model, but the source lies in a bounded region of space, so a numerical integration scheme can be proposed in order to calculate the received power for any position and orientation of the receiver.

$$h\left(x, y, z, \boldsymbol{n}_{Rx}, t\right) = \int_{-\sqrt{R^2-a^2}}^{\sqrt{R^2-a^2}} \int_{-\sqrt{R^2-a^2-x'^2}}^{\sqrt{R^2-a^2-x'^2}} I_{Tx}\left(x', y'\right) k\left(x', x, y', y, z, \boldsymbol{n}_{Rx}, t\right) \mathsf{d}x'\mathsf{d}y'$$

$$\tag{3.44}$$

This integral could be simplified by transforming it into polar coordinates over the surface of the source.

3.3   Sources defined by an implicit equation

In these scenarios, the surface of the source will be defined by an implicit equation, and the receiver will be considered to be pointed towards the center of symmetry of the source (which will be defined when the source is specified). Only stationary behavior will be analyzed in this work, but the dynamic equations for time-varying sources can be obtained by following the same procedure that was proposed for sources defined by monge coordinates

3.3.1   Cylindrical source

In this case, the manifold of the source is given implicitly by the equation

$$x'^2 + y'^2 = a^2 \tag{3.45}$$

this expression defines a cylinder on the space (considering the variable z' as a free variable, as it does not appear in (3.45)). The natural coordinates in this case are cylindrical coordinates, and (3.45) becomes

$$\rho' = a \tag{3.46}$$

Two scenarios can be considered with this geometry, in the first one, the receiver is outside the cylinder, and the unitary normal vector varies along the surface of the source with following expression

$$\boldsymbol{n}_{Tx} = \cos\left(\phi'\right)\boldsymbol{u}_x + \sin\left(\phi'\right)\boldsymbol{u}_y \tag{3.47}$$

The orientation vector of the receiver will be considered to be in this case

$$\boldsymbol{n}_{Rx} = -\cos\left(\phi\right)\boldsymbol{u}_x - \sin\left(\phi\right)\boldsymbol{u}_y \tag{3.48}$$

The distance between a position of the receiver and a point over the source is

$$R = \sqrt{\rho'^2 + \rho^2 - 2\rho'\rho\cos\left(\phi - \phi'\right) + \left(z - z'\right)^2} \tag{3.49}$$

The received optical power can be obtained with equation (3.5) and can be expressed as

$$\Phi_{Rx} = \iint_{S_{Tx}} M_{Tx}\left(\phi', z'\right) h\left(\rho, \phi - \phi', z - z'\right) \mathsf{d}\phi'\mathsf{d}z' \tag{3.50}$$

Where the function $h\left(\rho, \phi, z\right)$ is given by

$$h\left(\rho, \phi, z\right) = \frac{\rho' A_{Rx}\left(m + 1\right)\left[\rho\cos\left(\phi\right) - \rho'\right]^m \left[\rho - \rho'\cos\left(\phi\right)\right] g\left(\rho, \phi, z\right) \prod\left(\frac{\phi - \phi'}{\phi^C}\right)}{2\pi\left[\rho^2 + \rho'^2 - 2\rho'\rho\cos\left(\phi\right) + z^2\right]^{\frac{m+3}{2}}} \tag{3.51}$$

And the exitance function $M^{Tx}(\phi', z')$ is periodified in the ϕ' dimension. The angle ϕ^C is the angle where the ray path between the source and the receiver is tangent to the cylindrical surface as can be shown in Figure 3.6, and it is given by

$$\phi^C = \arccos\left(\frac{\rho'}{\rho}\right) \tag{3.52}$$
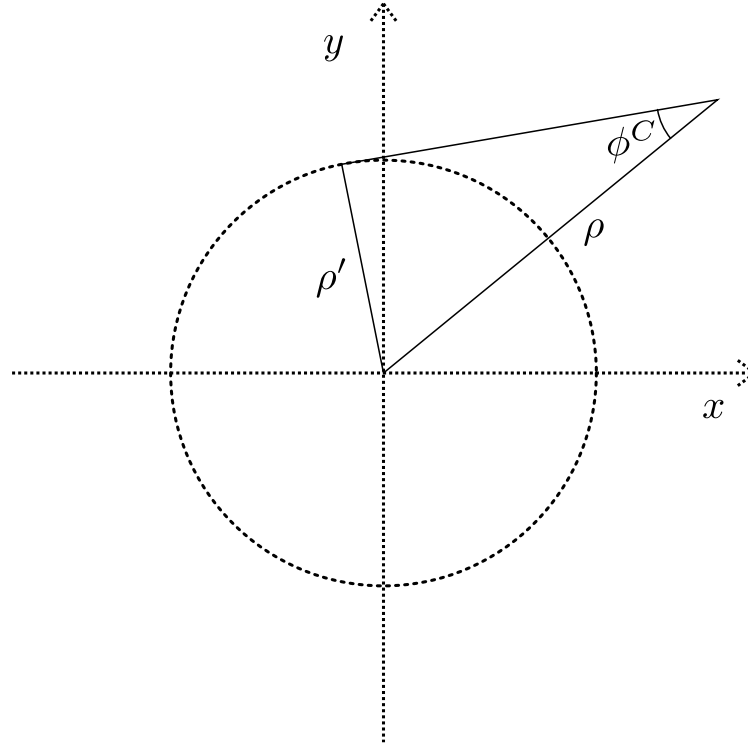
Figure 3.6: Critical angle for the cylinder source.

Equation (3.50) represents a convolution along a cylindrical domain, one of the variables is defined over an infinite straight line, and the other one is defined over a circumference. The received power is then expressed as

$$\Phi_{Rx} = M_{Tx}(\phi, z) * h(\rho, \phi, z) \tag{3.53}$$

3.3.2 Spherical sources

The source can be represented with the following implicit equation

$$x'^2 + y'^2 + z'^2 = a^2 \tag{3.54}$$

The spherical symmetry suggests the use of spherical coordinates to simplify the analysis in this case, the resulting expression for the surface in spherical coordinates is

$$R' = a \tag{3.55}$$

Analogue to the cylindrical source, two scenarios can be considered, in the first one, the receiver is located outside the spherical source, oriented towards the center of the sphere of the source, the unitary normal vector of the source could be expressed as

$$\boldsymbol{n}_{Tx} = \boldsymbol{u}_R \tag{3.56}$$

and the orientation vector of the receiver can be modelled as

$$\boldsymbol{n}_{Rx} = -\boldsymbol{u}_R \tag{3.57}$$

The procedure that will be used to obtain the power flux at every position outside the sphere of the source will be the following: first, the expression for the received power along the positive z axis will be obtained, then, the kernel, which must have azimuthal symmetry, will be identified, once the convolution kernel is known, the axis where the receiver lies will be rotated (this corresponds to a rotation of the kernel). This is the definition of the spherical convolution.

The received power over the positive z axis will be

$$\Phi_{Rx} = \iint_{S_{Tx}} M_{Tx}\left(\theta', \phi'\right) h\left(r, \theta'\right) \mathsf{d}\theta' \mathsf{d}\phi' \tag{3.58}$$

The kernel $h\left(r, \theta'\right)$ can be identified as

$$h\left(r, \theta'\right) = \frac{r'^2 \sin\left(\theta'\right) A_{Rx}\left(m+1\right)\left[r\cos\left(\theta'\right)-r'\right]^m\left[r-r'\cos\left(\phi'\right)\right]g\left(r,\theta'\right)\prod\left(\frac{\theta'}{\theta^C}\right)}{2\pi\left[r^2+r'^2-2r'r\cos\left(\theta'\right)\right]^{\frac{m+3}{2}}} \tag{3.59}$$

Where θ^C is the maximum angle to consider in the integration due to the curvature of the source. The situation is analogue to Figure 3.6, and it is given by

$$\theta^C = \arccos\left(\frac{r'}{r}\right) \tag{3.60}$$

The kernel function is independent of the azimuth coordinate, ϕ, thus, the invariance condition holds. the power flux at every position can be obtained by rotating the kernel function. Defining the rotation operator as $\rho_{R(\theta,\phi)}\left[\cdot\right]$, with θ and ϕ representing the angular positions of the receiver, the power flux for every position in space can be obtained as

$$\Phi_{Rx} = \iint_{S_{Tx}} M_{Tx}\left(\theta', \phi'\right) \rho_{R(\theta,\phi)}\left[h\left(r, \theta'\right)\right] \mathsf{d}\theta' \mathsf{d}\phi' \tag{3.61}$$

The expression in (3.61) can be interpreted as a spherical convolution [45], and thus, the receiver power can be expressed as

$$\Phi_{Rx} = M_{Tx}\left(\theta, \phi\right) \circledast h\left(r, \theta\right) \tag{3.62}$$

The spherical convolution can be computed as the inverse spherical harmonic transform of the product of the spherical harmonic coefficients of the exitance function, the eigenvalues λ_l and the spherical harmonic coefficients of the kernel function. The eigenvalues are given by

$$\lambda_l = \sqrt{\frac{4\pi}{2l+1}} \tag{3.63}$$

3.4   Numerical analysis considerations

To compute the irradiance maps using numerical methods, it is necessary to distinguish between the convolution methods, and the direct integration methods.   For the convolution, it could be evaluated directly, or using the convolution property of the Fourier Transform.   In the case of spherical images (spherical symmetry), the Fourier Transform will decompose the function as a linear combination of spherical harmonic functions. The numerical evaluation of the Fourier Transform can be performed in the case of flat sources through the use of the Fast Fourier Transform (FFT) algorithm.
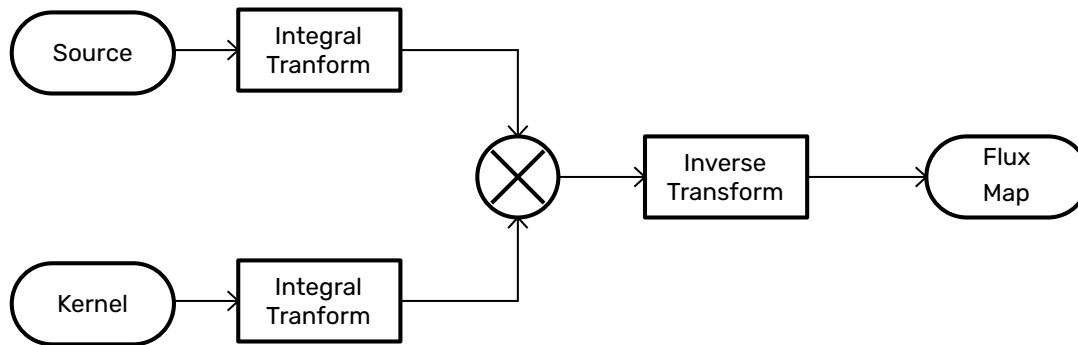
Figure 3.7: Block diagram of the transform-based method used to evaluate power flux maps.

When the irradiance map or the received power is being evaluated using direct integration, the domain of the integral must be clearly defined, and a discretization method must be studied prior to the evaluation of the integral. Once the discretization method has been determined, then the integral can be evaluated with a precision given by the level of detail that the discretization and the number of evaluation points allow.

Chapter 4

Potential applications

In this chapter, some potential applications of the models developed in Chapter 3 are described. The main idea of this chapter is to show some possible use cases of the mathematical models that were described in the previous chapter. The first application that will be introduced in this chapter is related to the system design problem. The models could be used to predict the effects of the channel, and thus, to make rational decisions in the design process. The power transmission models could also be used to estimate the coverage areas and bandwidths of different OWC links if the parameters of the channel are known. The fourth application is the design of Visible Light Positioning (VLP) algorithms based on the properties of the channel. The last two applications are related to the development of theoretical models for two different research fields. In the first case, the models of the previous chapter are proposed as a theoretical framework that could be used to analyze the light distribution inside a cylindrical photobioreactor. There are commercial photobioreactors with cylindrical shape, but the design of the illumination systems is commonly left to a second plane, the cylindrical source model with a closed surface receiver could be used as an estimation of the behavior of light propagation and attenuation inside the photobioreactor. The last application is related to OCC. The characterization of the OCC channel is an active area of research, and maybe some modified version of the models proposed in Chapter 3 could be used to obtain an estimation of the behavior of the channel.

4.1   Design of optical source arrays satisfying a given power flux constraint

In some situations, the desired power flux pattern is known and the goal is to obtain an optical source that generates that pattern at a given distance.
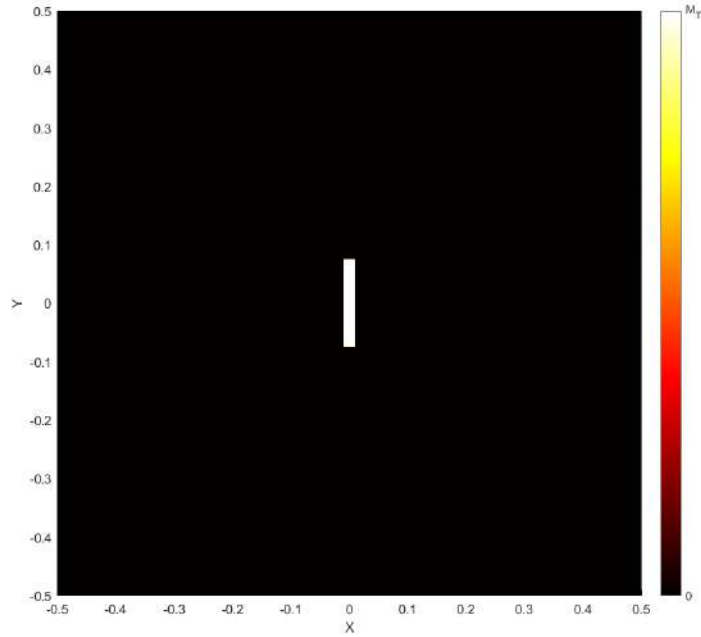
Figure 4.1: Described source exitance distribution.

When the optical source consists on an array of N unitary elements, the optimal configuration can be calculated as a solution for the following optimization problem

$$\min_{M_{Tx}} ||\Phi_{Obj} - \Phi|| \qquad (4.1)$$

Where M_{Tx} is the exitance distribution of the whole optical source, which consists on the sum of the exitances of the individual elements, Φ_{Obj} is the desired power distribution in the receiver plane and Φ is the received power at every point in the receiver plane, calculated using the source distribution and the equations of Chapter 3. The number of elements, as well as some geometric considerations may be introduced as parameters of the optimization model. Another approach for this optimization problem would be to evaluate the deconvolution of the desired irradiance to obtain the exitance distribution that would generate it, and then optimize the source distribution using the ideal exitance function that would generate the irradiance map. To give an example of this kind of application, consider a rectangular strip source with 15 cm of length, 2 cm of width and an uniform exitance M_{Tx} that will be obtained. If a 15° AoA and 1 cm² active area

receiver is used, and a square shaped 10 mW uniform power map with a side length of 2 m is desired at a distance of 2 m from respect the source plane, the power map generated at 2 m by one of the sources can be obtained through the convolution method described in Chapter 3, the shape of the source can be seen in Figure 4.1 and the estimated received power can be seen in Figure 4.2. The desired power map can be approximated by a linear combination of shifted versions of the map shown in 4.2. The number of sources, shifts and exitance values might me obtained by the use of any optimization method. In this case, the array shown in Figure 4.3 was obtained as the source of the corresponding power map shown in Figure 4.4. The generated array has 96 elements, the source elements are separated 20 cm in the horizontal dimension and 30 cm in the vertical dimension.
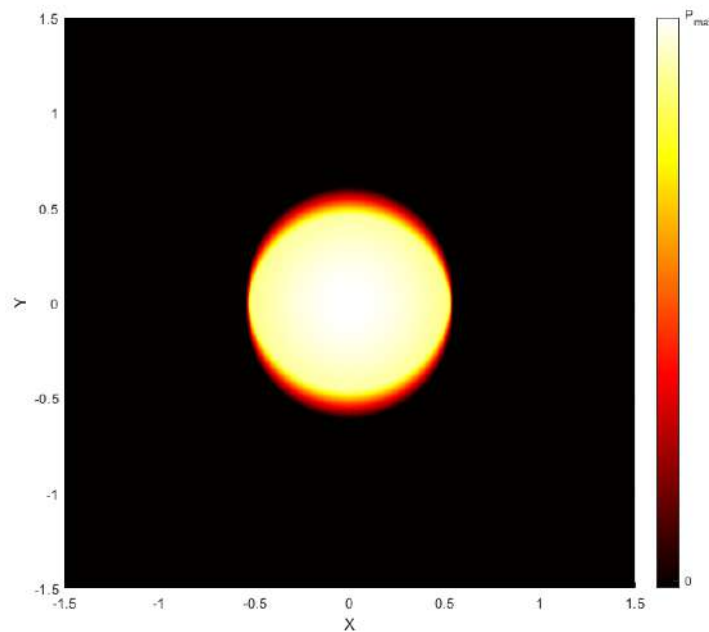
Figure 4.2: Power map generated by the described source at a distance of 2 m.

More sophisticated design procedures can be used, but this would lie out of the scope of this work, the objective of this section is just to demonstrate the applicability of the models derived in Chapter 3 to some practical scenarios.
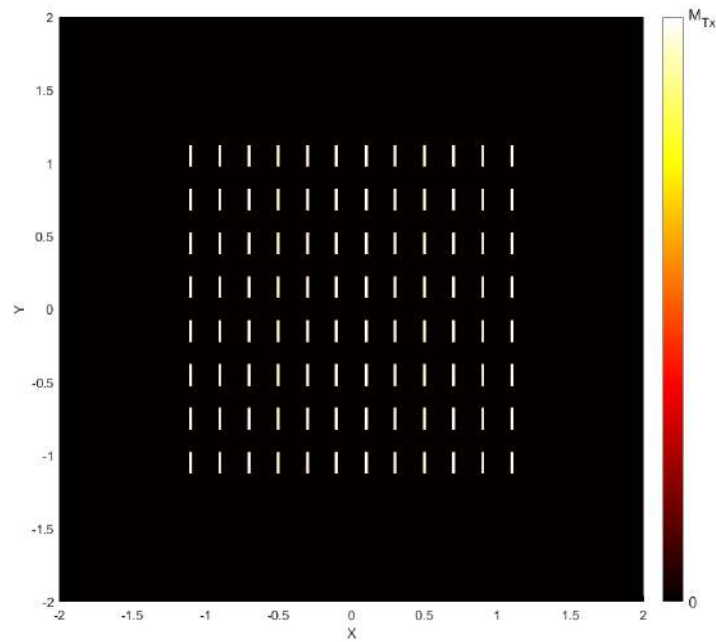
Figure 4.3: Obtained source array to generate an approximation of the desired power map.
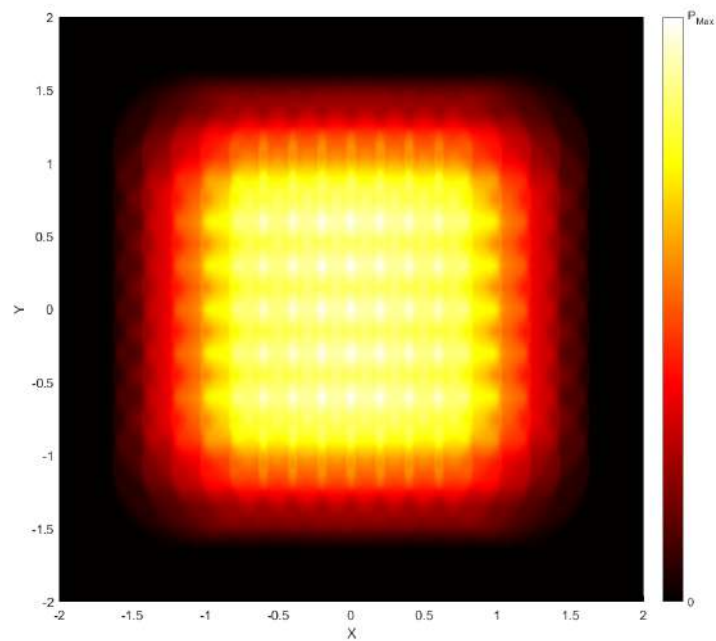

Figure 4.4: Simulated power map of the rectangular array.

4.2   VLP algorithms and systems

The spatial behavior of the OWC link for some specific source and receiver configurations enable the development of positioning applications.A positioning scheme can be proposed using the one-to-one property of the flux profile for certain exitance functions along the source and considering a receiver positioned on the optical axis.   This kind of positioning scheme depends on the characteristics of the receiver and is sensitive to perturbations in the tilt of the receiver because the cylindrical symmetry is a fundamental characteristic of this scheme, the geometric configuration for this positioning scheme is shown in Figure 4.5. The received power in this scenario can be modelled as

$$\Phi_{Rx}\left(z\right) = P_{Tx}A_{Rx}\left(m+1\right)\int_0^\infty I_{Tx}\left(\rho'\right)\frac{z^{m+1}\rho'g\left(\rho',z\right)}{\left(z^2+\rho'^2\right)^{\frac{m+3}{2}}}\mathsf{d}\rho' \tag{4.2}$$

This expression can be regarded as an integral transform whose kernel is given by

$$K\left(\rho',z\right) = \frac{z^{m+1}\rho'g\left(\rho',z\right)}{\left(z^2+\rho'^2\right)^{\frac{m+3}{2}}} \tag{4.3}$$

The simplest scenario that could be used for optical axis positioning is given by a sawtooth radial profile in the source, the source profile and the expected received power is shown in Figure 4.6 for a source with a Lambertian index of 1 whose geometry is given by an annulus and considering a perfect occlusion function $g\left(\rho',z\right)$ given by a step function.

The behavior of the received power along the optical axis can be approximated in this case by a linear function near the center of the interval $(\rho_1/\tan\left(AoA/2\right),\rho_2/\tan\left(AoA/2\right))$, and the designer can modify the values of ρ_1, ρ_2 and the AoA in order to define the region of operation of the positioning system. The error generated by displacement and orientation respect to the optical axis can be predicted using the model proposed in Chapter 3. These two errors have been obtained for the case of $rho_1 = 5cm$, $rho_2 = 10cm$, $I_{max} = 1$, $P_{Tx} = 1W$ and $A_{Rx} = 1m^2$. These results are shown in Figure 4.7 and Figure 4.8.

The power profile of the source can be adjusted to obtain other power distributions along the optical axis, and the effects of positioning and orientation errors can be analytically and experimentally studied, but this work would be out of the scope of this project.

Another positioning scheme can be proposed for a 2D plane surface using 3 channels. An increasing function along one of the axes of the plane is used in one channel over the emitter, over other channel, an increasing function over the second axis, and the third channel with a constant exitance acting as a power level reference. In this scheme, the only dependence on the characteristics of the receiver is related to its Angle of Acceptance (AoA) and its responsivity to the three channels. If both parameters are known, this scheme would give an easy positioning system for a 2D plane.
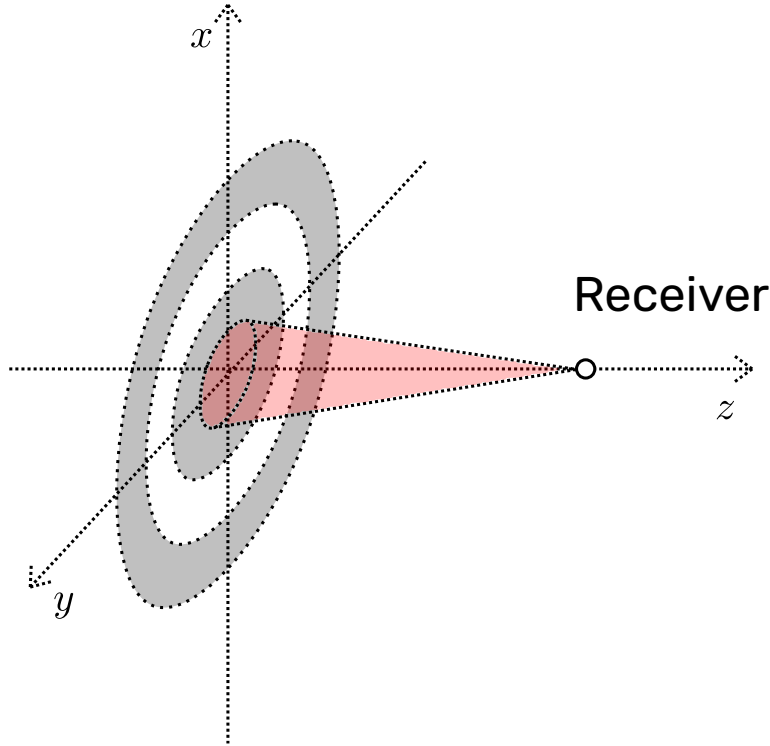
Figure 4.5: Geometric configuration of the line positioning scheme proposed.

4.3   Other proposed applications

Other applications that would involve a deeper study could be developed for the models of Chapter 3. In this section, some of those applications are briefly discussed.

4.3.1   Coverage simulation in OWC links

The power flux equations described in Chapter 3 combined with the specifications of a certain receiver enable the construction of a coverage map for the given communication system. In this case it is also customary to carry a detailed analysis of the noise in the receiver to determine the positions in space where communication can happen. The noise in an optical receiver has to be analyzed according to the shot noise model and the Johnson–Nyquist model. The thermal noise in a photodiode is given by

$$\sigma_{Th}^2 = \frac{4k_B T_e q F_n B}{R_L} \tag{4.4}$$
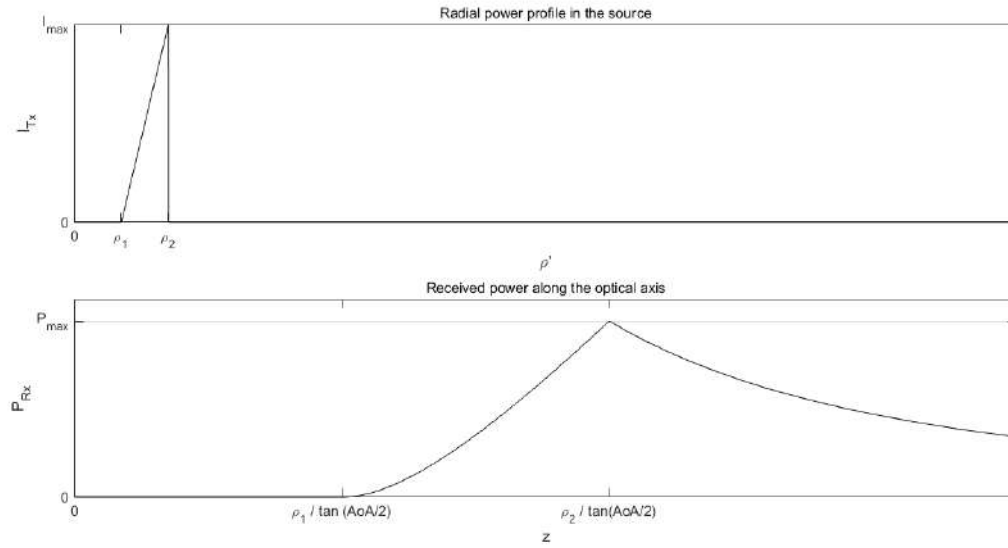
Figure 4.6: Radial power profile in the source against received power in the optical axis.
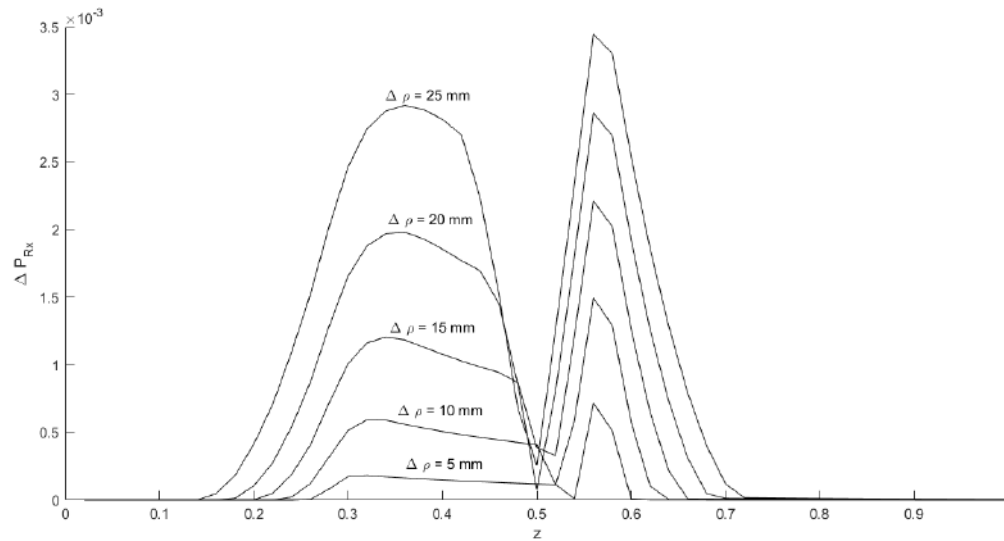
Figure 4.7: Power error for different displacements of the receiver axis.

Which does not depend on the nature of the receiver. The shot noise, on the other hand, depends on the type of receiver being used. In the case of a pin photodiode, the shot noise power can be modelled as follows

$$\sigma_{Sh}^2 = 2q \left(\Re \Phi_{Rx} + I_D \right) B \tag{4.5}$$

while in the case of an APD, the expression of the power of the shot noise must be modified to include the effects of impact ionization
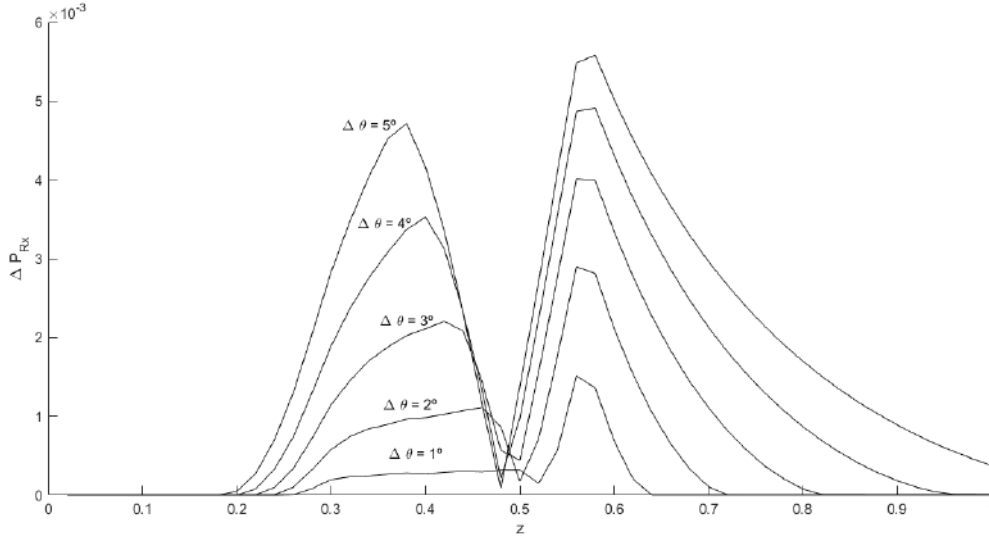
Figure 4.8: Received power error for different pointing errors.

$$\sigma_{Sh}^2 = 2qM^2F_A\left(\Re\Phi_{Rx} + I_D\right)B \tag{4.6}$$

Taking this into account, the coverage region for a given OWC link can be calculated with the inequality given by

$$\frac{\Re^2\Phi_{Rx}{}^2}{2q\left(\Re\Phi_{Rx} + I_D\right)B + \frac{4k_BT_eqF_nB}{R_L}} \geq \mathsf{SNR}_{Min} \tag{4.7}$$

for a pin photodiode, and

$$\frac{M^2\Re^2\Phi_{Rx}{}^2}{2qM^2F_A\left(\Re\Phi_{Rx} + I_D\right)B + \frac{4k_BT_eqF_nB}{R_L}} \geq \mathsf{SNR}_{Min} \tag{4.8}$$

for an APD.

4.3.2   Dependence of link bandwidth on the AoA of the receiver

If the time-dependent equations of the radiometric model are used, the channel impulse response can be derived for any position in space. Something to take into account is the fact that the temporal behavior of the system depends strongly on the shape of the emitter, and thus the temporal term in the flux equation forms part of the kernel of the integral transform, and not of the geometrical term. This translates into a link bandwidth map for every position which can be easily obtained using the proposed model, and experimentally tested using the right instrumentation equipment.   If the channel impulse reponse $h(t)$ can be estimated, the delay spread, τ_{RMS} can be calculated as was shown in Chapter 3. The bandwidth can be estimated once the delay spread is known by using, for example, the following estimation

$$B \approx \frac{0.2}{\tau_{RMS}} \tag{4.9}$$

4.3.3   Power propagation in a cylindrical container under the scattering of particles

The propagation of power through a medium has been modelled using Beer's Law. In the equation of Beer's Law the attenuation coefficient contemplates the absorption of power by the medium as well as the losses due to scattering (this approximation can only be done when the scattering is highly directive). If the receiver is modelled as an isotropic receiver (closed surface) and the medium is considered to be populated with small particles that absorb and scatter the light, then (3.8) can be used to estimate the power arriving to a specimen situated at an specified position.

4.3.4   Characterization of OCC channels

If every pixel of a camera is considered to be a directive receiver with a limited AoA, then the image generated by a camera in different positions in space can be simulated by using the proposed mathematical model for different receivers with different orientation angles. This approach considers the camera system as an array of directive receivers, and could be used as a framework to analyze MIMO systems. The main drawback of this model is that it is necessary to evaluate the power distribution for every possible orientation, and then the whole image can be recovered by assigning the obtained value for every orientation to its associated pixel.
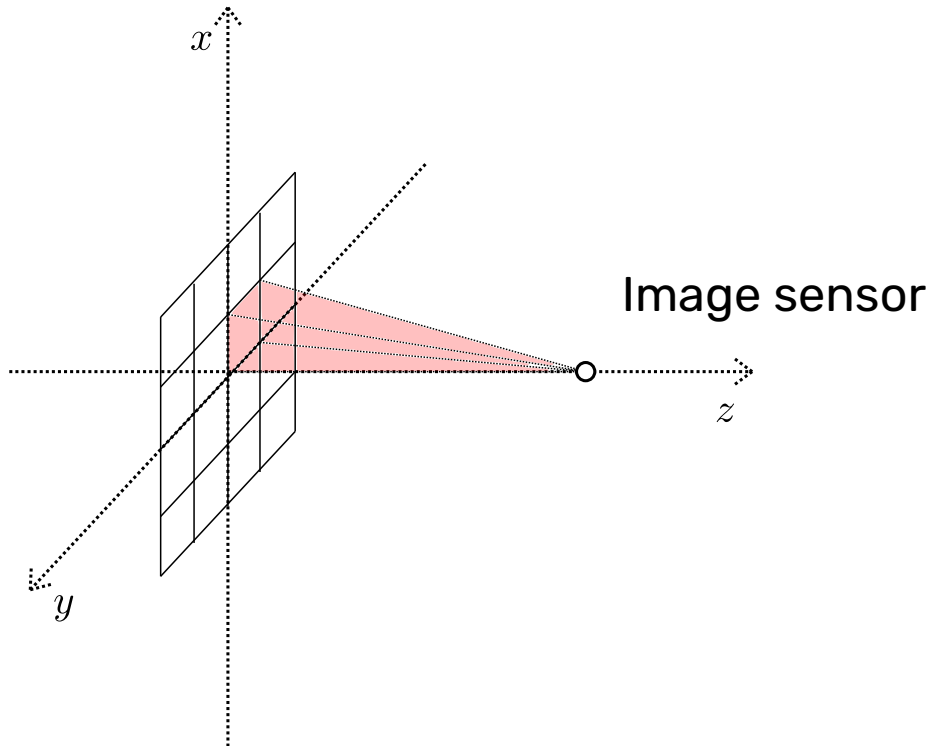
Figure 4.9: Configuration for the proposed OCC model application.

Chapter 5

Design of an automatic measurement system

In order to obtain an experimental validation of the results of Chapter 3, it is necessary to develop a measurement system. The design of the measurement system with all of its subsystems is the goal of this chapter.
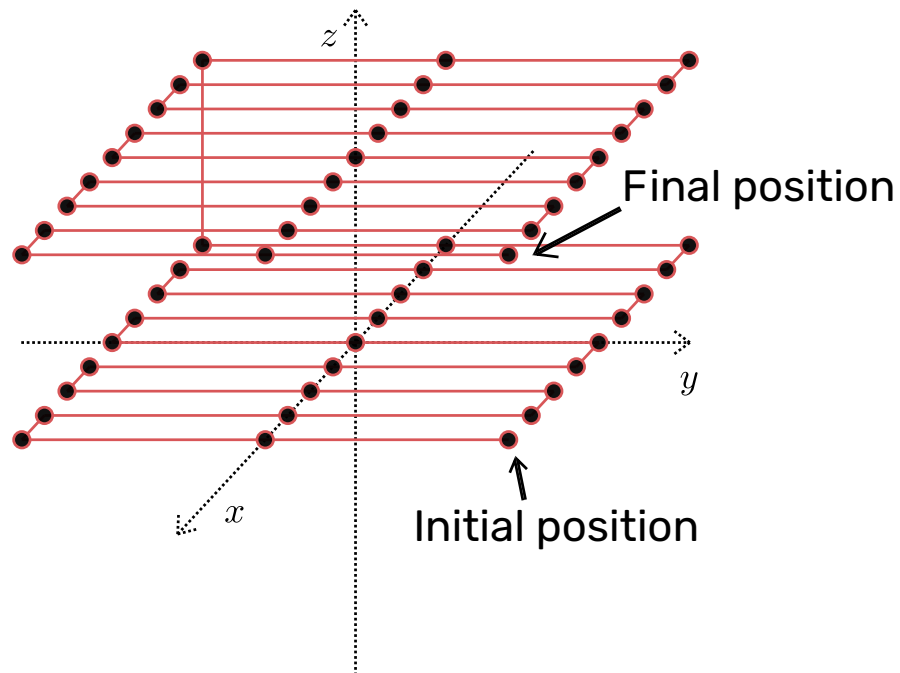
Figure 5.1: Example of a spatial sampling path that could be used to characterize the near-field behavior of an optical source.

5.1   Spatial sampling scheme

In order to obtain a balanced sample along a cubic region in space, the adopted sampling scheme is a linear path that traverses the cube describing a meander-like trajectory.

The way to define this spatial grid will be to specify the distances between adjacent points and the region of space (a convex region) that will be analyzed. The position of the optical source should also be specified in order to have the information about the relative positions between source and probe. In order to generate the ordered triplets of coordinates that define this kind of path, the following algorithm can be used. Suppose that the minimum an maximum value that every coordinate will take is known, as well as the number of points that will be evaluated for every coordinate. In this case, the points of the first coordinate will be repeated in alternating increasing and decreasing order until the spatial grid has been completely explored. The second coordinate will only change its value when a complete increment or decrease of the first coordinate has occurred. The third coordinate will increment its value when a complete increment or decrease of the second coordinate has taken place. This set of ordered points can be stored in a temporal variable or in a file until it is needed.
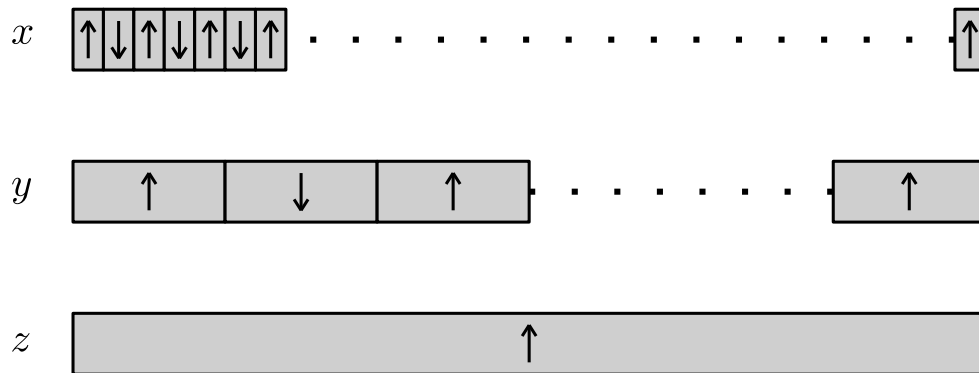

Figure 5.2: Structure for the generation of the coordinate triplets, an arrow pointing upwards means an increasing value of the specified coordinate, while an arrow pointing downwards means a decreasing value.

5.2   Mechanical subsystem modelling

The objective of this section is to define some mechanical systems that could be used to generate a spatial sampling grid, the first will be a complete and precise system that would be used to obtain a full 3D characterization of the scenario, considering both the position and the tilt of the receiver, and the second model would be a simplified one that only considers the positions of the receiver, with a fixed tilt and can thus be implemented using the mechanical structure of a 3D printer.

5.2.1   5-DoF mechanical system

The 5 mechanical variables in this model are the 3 cartesian coordinates, that can be controlled with three linear motion mechanisms, and the other two variables are the tilt angles of the receiver, that could be controlled with two independent angular motion mechanisms (motors). The linear motion mechanisms must be implemented using a motor and a mechanism that converts the rotary motion of the motor into a linear motion such as those shown in 5.3.
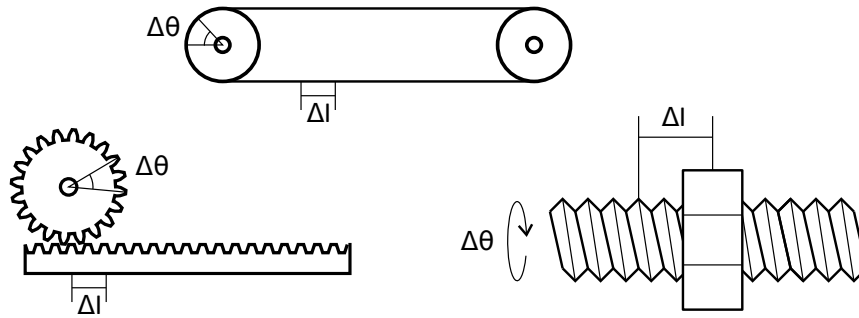

Figure 5.3: Some mechanisms that enable rotary to linear motion conversion, from left to right: rack and pinion, drive belt and screw–nut mechanism.

The angular motion mechanisms that determine the orientation of the receiver could be two motors assembled in a header whose position is determined by the previous linear actuators. Considering that the three motors used for the linear movement have angular positions θ_x, θ_y and θ_z, the position of the header can be determined as

$$\boldsymbol{r}_h = (x_0 + K_x (\theta_x - \theta_{x0})) \, \boldsymbol{u}_x + (y_0 + K_y (\theta_y - \theta_{y0})) \, \boldsymbol{u}_y + (z_0 + K_z (\theta_z - \theta_{z0})) \, \boldsymbol{u}_z \quad \text{(5.1)}$$

where x_0, y_0 and z_0 are the initial positions of the header, K_x, K_y and K_z are the conversion factors of the rotary to linear motion mechanisms in the three

directions and θ_{x0}, θ_{y0} and θ_{z0} are the initial angular positions of the three motors. In addition, the other two motors, used for the orientation of the photodiode have angular positions α and β, the exact position of the photodiode is given by

$$\boldsymbol{r}_{pd} = \boldsymbol{r}_h + \Delta\boldsymbol{r} \tag{5.2}$$

where Δr is given by

$$\Delta\boldsymbol{r} = R_{pd}\boldsymbol{n}_{Rx} \tag{5.3}$$

where R_{pd} is the radius of the sphere defined by this part of the mechanism and the photodiode orientation is given by $\boldsymbol{n}_{Rx}$, which is an unitary vector

$$\boldsymbol{n}_{Rx} = \sin{(\alpha)}\cos{(\beta)}\boldsymbol{u}_x + \sin{(\alpha)}\sin{(\beta)}\boldsymbol{u}_y - \cos{(\alpha)}\boldsymbol{u}_z \tag{5.4}$$

5.2.2   3-DoF simplified mechanical system

The only variables that will be retained in this simplified model will be the three coordinates of the position. The orientation of the receiver will be fixed in this case.

Considering that three motors are being used with angular positions θ_x, θ_y and θ_z, the position of the photodiode can be determined as

$$\boldsymbol{r}_{pd} = \left(x_0 + K_x\left(\theta_x - \theta_{x0}\right)\right)\boldsymbol{u}_x + \left(y_0 + K_y\left(\theta_y - \theta_{y0}\right)\right)\boldsymbol{u}_y + \left(z_0 + K_z\left(\theta_z - \theta_{z0}\right)\right)\boldsymbol{u}_z \tag{5.5}$$

which is algebraically similar to (5.1) but in this case the constants x_0, y_0 and z_0 directly include the offset of the position of the photodiode respect to the position of the header.

5.2.3   Other possible geometries

Two remarkable alternative geometries can be considered, but will not be used in this work, a spherical system with fixed orientation towards the center, and a similar cylindrical system. In these scenarios, the main difference is that one or two of the rotary to linear motion mechanisms will be substituted by rotary to rotary motion mechanisms with one of the circumferences moving inside the other as shown in 5.5.
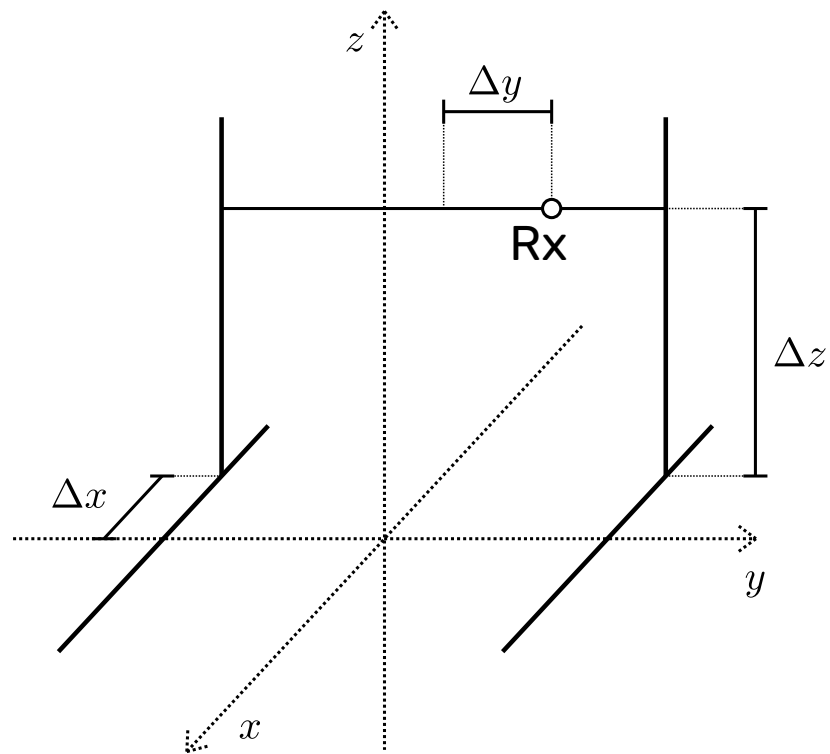
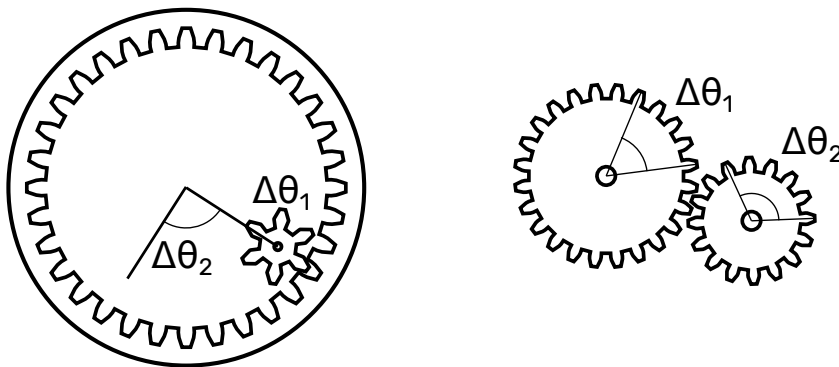Figure 5.4: Schematic diagram of the mechanical system for the 3 DOF configuration.

Figure 5.5: Some mechanisms that enable transformation of rotary motions.

5.3   Control and measurement subsystem

The motors of the mechanical system must be controlled externally by another subsystem that generates the needed control signals. In the case of stepper motors, a microcontroller can be used to generate digital control signals. In addition to the control of the state of the motors, the control system must be capable of communicating with the measurement subsystem, which will take samples of the received power value when the photodiode is correctly positioned. In Figure 5.6, a block diagram illustrating the relation between the mechanical and control subsystems is shown.
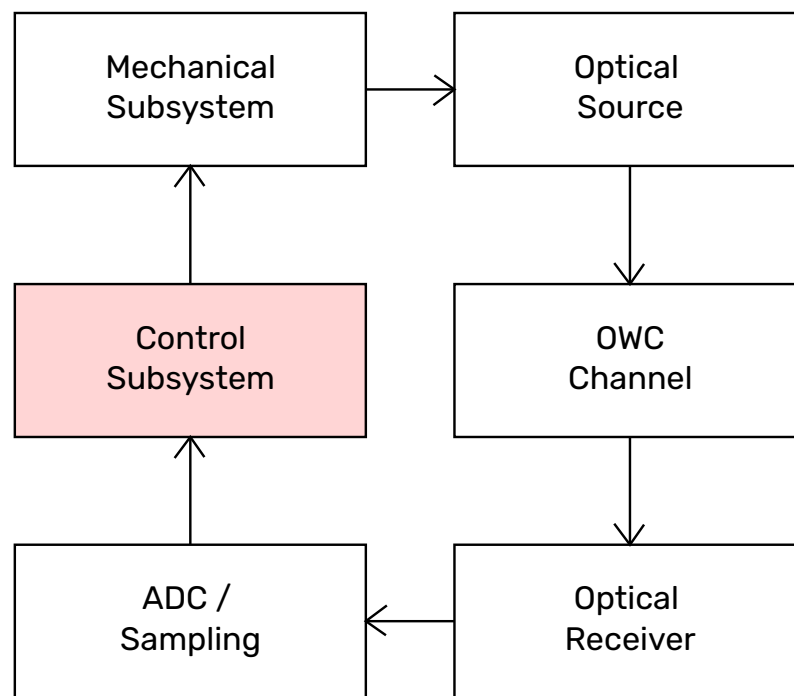
Figure 5.6: Block diagram of the relationship between the control subsystem and the measurement device.

5.4   Additional mechanical parts

In order to couple the photodiode to the header of the 3D printer, it is needed to design a mechanical adapter with the mechanical interfaces of both the header and the photodiode (Figure 5.7).
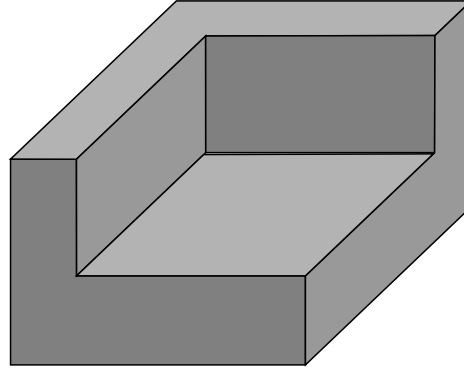

Figure 5.7: Schematic of the mechanical interface used to fix the photodiode to the printer header.

Furthermore, in order to be able to limit the AoA of the photodetector, some optical elements would be needed, in this case, after considering all the possible optical elements that could be used, the AoA will be limited by occlusion, and thus some mechanical parts that will act as occluders with different AoA values will be used (Figure 5.8).
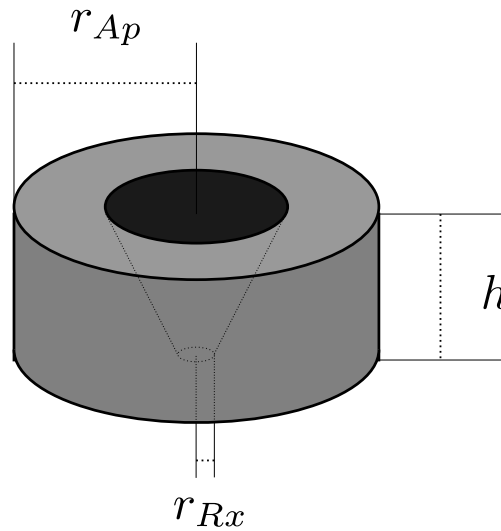

Figure 5.8: Geometry of the proposed optical occluders.

Chapter 6

Experimental methodology

In this chapter, the experimental setup is presented and explained. The operation of the mechanical system of the 3D printer is described, as well as the dimensions of the occluders and the spatial sampling grids used in the measurement routine. The steps followed in the execution of the experiment are stated clearly, and after that, a brief statistical analysis is performed to justify the averaging to reduce the effects of noise in the results.

6.1 Description of the experiments

An implementation of the measurement system described in Chapter 5 will be used to perform a validation protocol on two different optical sources. In this work, only static behavior will be considered, and the measurement system will be used to obtain irradiance maps for the different source and receiver configurations. The two different extended sources that will be used are a 1080x1920 screen (Figure 6.1) from a Huawei P9 smartphone and a LED lamp formed by an array (Figure 6.2). The purpose of introducing the LED lamp is to introduce a source whose geometry is not as simple as that of the smartphone screen. Nonetheless, if only the bare LED lamp was considered, the geometry could be assumed to be even simpler than the rectangular screen. To generate a more complex source, a diffuser was placed on top of the LED lamp. This way, the radiance of the diffuser when it is being illuminated by the source is more difficult to estimate theoretically, and it is necessary to characterize it empirically in order to simulate the behavior of the source. The LED lamp with the diffuser on top can be seen in Figure 6.3. Two different experiments will be proposed for the validation of the the mathematical model. In both experiments, different optical occluders such as those described in Chapter 5 will be used to limit the AoA of the receiver (Figure 6.4). The radius of the receiver end of the occluders will be 0.27 cm. The aperture and the height of the occluders, as well as the AoV are shown in Table 6.1. The spatial grid where the power is measured will be different for every experiment. Once the spatial grid is fixed, the receiver is transported along it with the use of a 3 DoF mechanical system, just as described in Chapter 5.

The mechanical system of a Robo3D R1+ 3D printer will be used, and its mechanical operation will be described in the following.

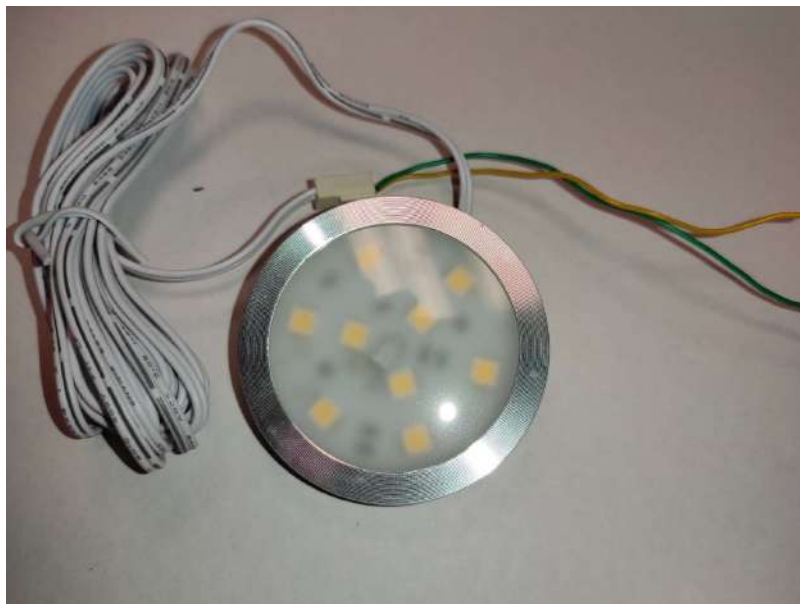Figure 6.1: Smartphone used as an extended source.

Figure 6.2: LED array used in the experiment.

The movement along the three spatial axes is based on the use of three different mechanisms that transform the rotary movement of a stepper motor. The mechanism used to move along the x axis is a drive belt as can be appreciated in Figure 6.5, the movement along the z axis is obtained by the rotation of a screw

Figure 6.3: LED lamp with the diffuser placed over it to generate a complex source.

Table 6.1: Geometrical parameters of the designed occluders.

AoV	h	r_{Ap}
41.49°	1.54 cm	1.37 cm
23.52°	2.16 cm	0.94 cm
13.78°	2.16 cm	0.53 cm

as depicted in Figure 6.6. The movement of the y axis is obtained by the displacement of the base, this is obtained through the use of a transmission band whose terminals are fixed to the borders of the base, this is shown in Figure 6.7, and the mechanism that enables this movement is just a pair of pulleys that transform the rotary movement of a stepper motor into the linear movement of the base, as shown in Figure 6.8.

The receiver device that will be used in these experiments will be an amplified Positive-Intrinsic-Negative (pin) photodiode (Figure 6.9).

To fix the photodiode to the header of the 3D printer, a mechanical adapter such as the one defined in Chapter 5 was fabricated (Figure 6.10). The photodiode mounted on the adapter can be seen in Figure 6.11. This mechanical adapter has a screw opening with the same diameter of the printer nozzle. The socket of the printer nozzle, where the mechanical adapter with the photodiode mounted will be screwed can be seen in Figure 6.12.

The instrumentation equipment that is needed in order to perform the experiment is an oscilloscope that can be controlled through an USB interface, a voltage source and a signal generator that can be controlled through an USB interface. The full setup can be seen on Figure 6.13

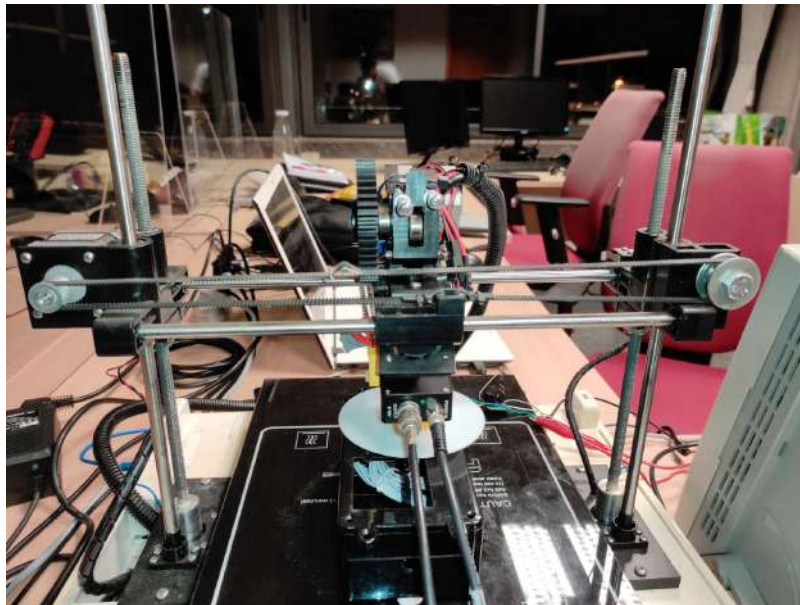Figure 6.4: Optical occluders used in the experiment.

Figure 6.5: Transmission band enabling the movement in the x axis.
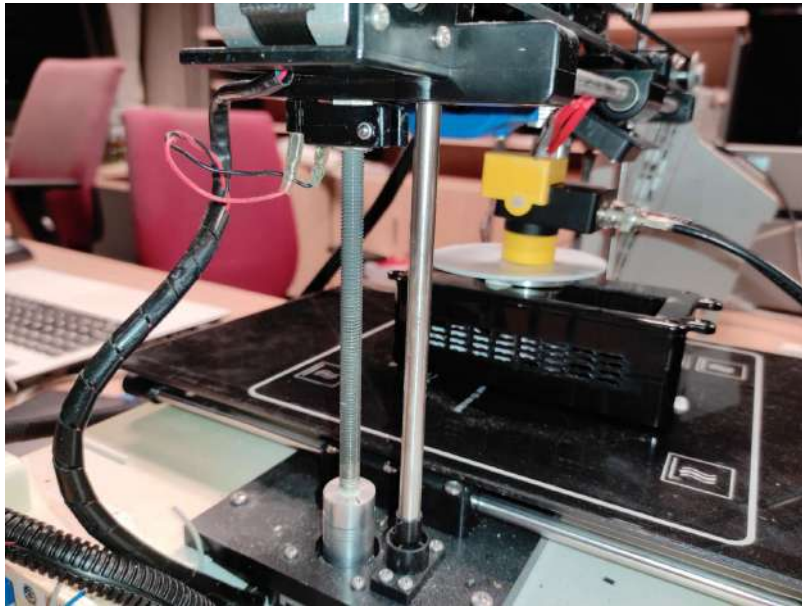
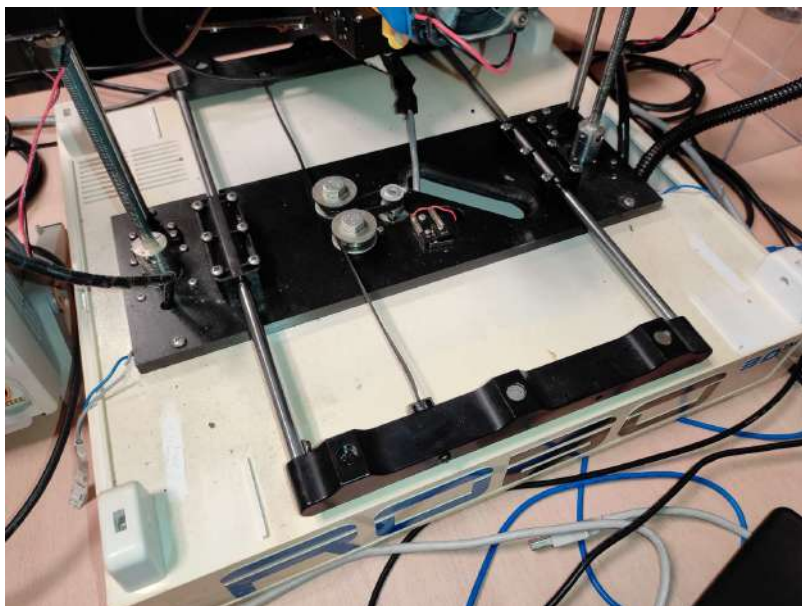Figure 6.6: Screw mechanism that enables the movement on the z axis.

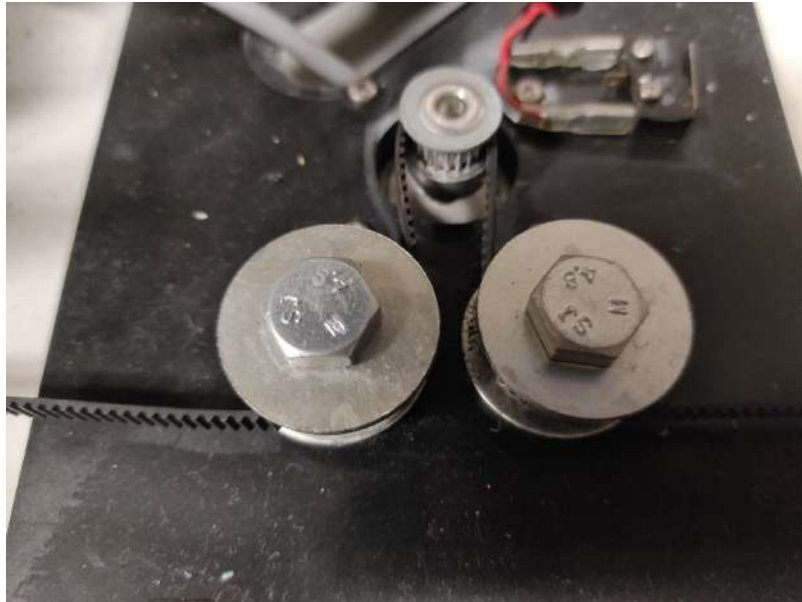Figure 6.7: Mechanism that enables the movement of the base on the y axis.

Figure 6.8: Detail of the pulley mechanism that transforms the rotary motion of the stepper motor into the linear movement of the base.

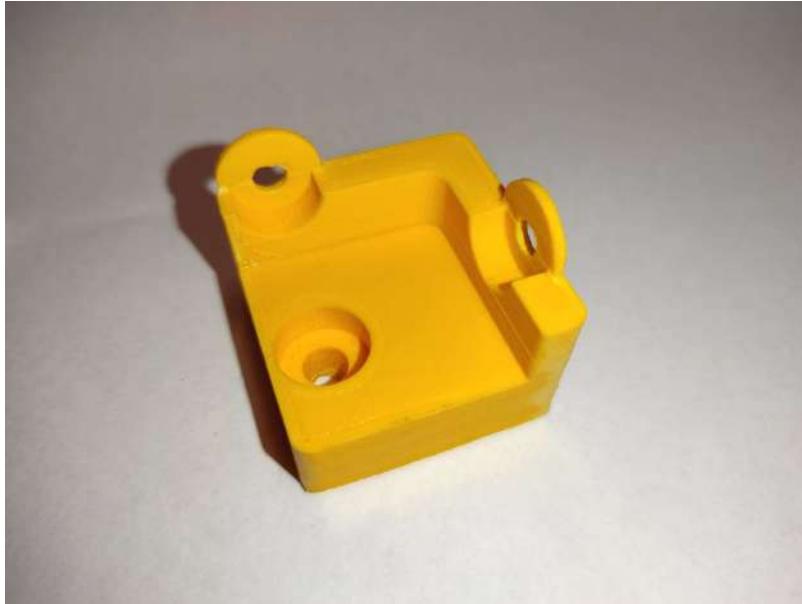Figure 6.9: Photodiode that will be used as the receiver in the experiments.

Figure 6.10: Mechanical adapter for the photodiode.

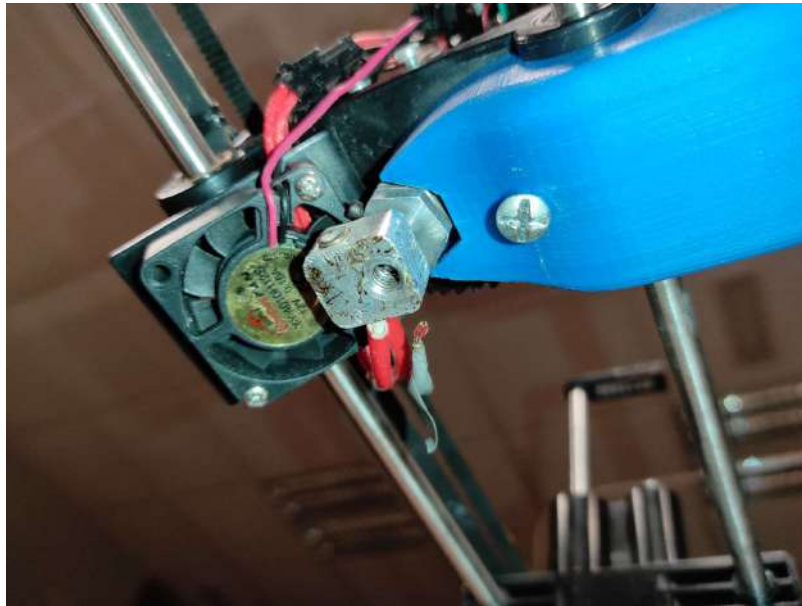Figure 6.11: Photodiode mounted on the mechanical adapter.

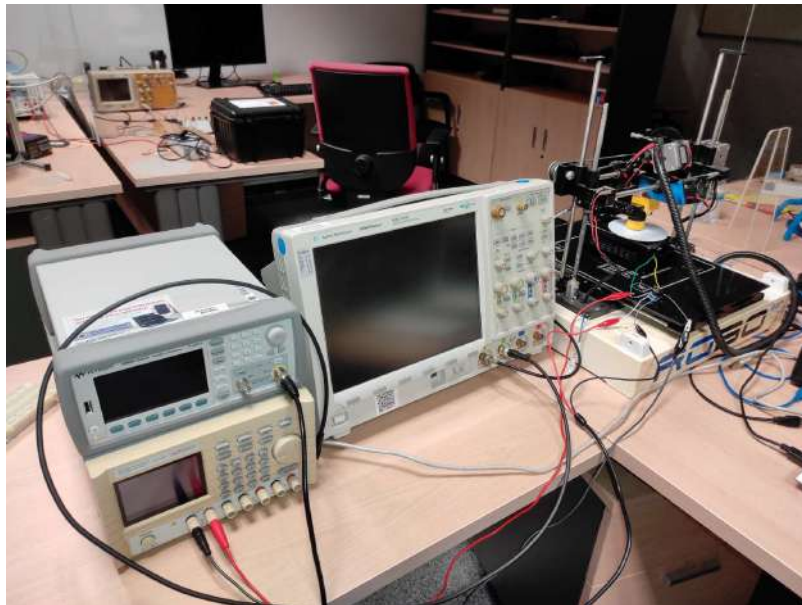Figure 6.12: Nozzle socket of the 3D printer.

Figure 6.13: Image of the full setup for the experiment.

6.2   Sampling routine and preliminary analysis

The header of the 3D printer with the mounted photodiode will traverse across a spatial path that will cross every measure point of the grid as stated in Chapter 5. In order to obtain a coherent dataset, the sampling must be synchronized with the movement of the header. The firmware of the 3D printer does not notify the controller when the header arrives to the specified position (it just interprets the SCPI command that is issued through the serial port). However, there is a SCPI command that allows the controller to query for the current position of the header. This way, a synchronization subroutine can be implemented by asking for the position of the header until it arrives to its destination. Once the header has arrived to the desired position, the measure can be taken by issuing a sequence of SCPI commands to the oscilloscope. The measured data will be stored locally in the computer where an averaging filter will be applied to reduce the effects of noise (this will be treated in the next section. The values obtained by the oscilloscope are samples of a voltage signal that is proportional to the current generated in the photodiode as a response to the incident optical power (see Figure 6.14)
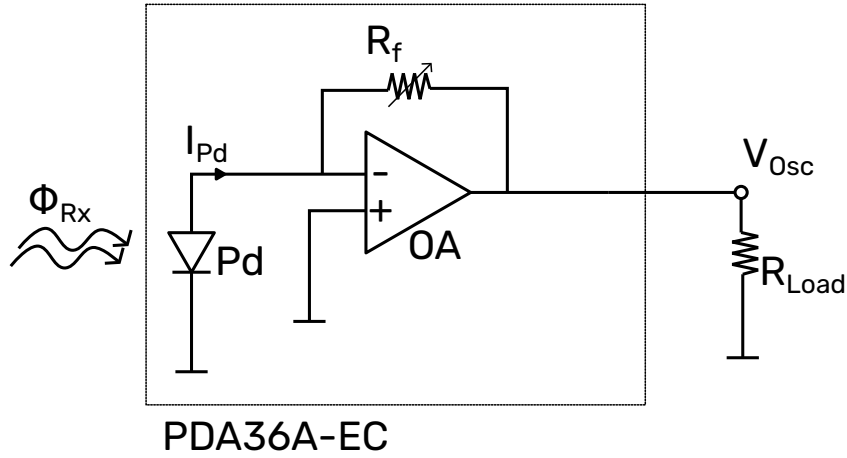

Figure 6.14: Circuit schematic of the receiver used in the experiment.

By taking this into account, the received power in every position can be estimated through the measurement of the voltage in the oscilloscope. The current generated in the photodiode can be calculated as

$$I_{pd} = I_{Rx} + I_D + I_{sh} + I_{th}$$ (6.1)

The term I_{Rx} is described in Equation 3.1, I_D is the dark current of the photodiode, and the terms I_{sh} and I_{th} are the shot and thermal noise currents in the receiver. The voltage at the output of the receiver is given by

$$V_o = R_f I_{pd} \tag{6.2}$$

Where R is the transimpedance gain of the amplifier. This will be the voltage measured in the oscilloscope, taking into account its input impedance (1 M). The received optical power can be recovered from the measured voltage easily with the following expression.

$$\Phi_{Rx} \approx \frac{\bar{V}_o}{R_f \mathfrak{R}} \tag{6.3}$$

The flowchart of Figure 6.15 depicts the relationship between the different steps that have been explained in this section, which describe the experiment.

6.3   Error analysis

When the computer issues a movement command to the 3D printer, the movement of the header is performed using a feedback loop (this loop is programmed in the firmware of the printer). Even though this feedback loop reduces the deviations from the desired position, there always exists a precision error in the measurement of the position that generates a positioning error every time the header is moved. Because of this, the position of the header will be considered a random variable for every sample taken in the experimental process. However, the dominant source of error is not the deviations from the expected position of the header, but the electrical noise that is generated in the photodiode and the amplifier in the reception process.

6.3.1   Positioning error analysis

The position of the header after every movement command is a normal random variable whose mean is the desired position on the grid, and its variance models the positioning error. The algorithm which implements the movement in the 3D printer uses a feedback loop and obtains a precision of 10^{-2} mm. This precision is the same that can be obtained for the measurements of the position in real-time. The standard deviation of this error is thus small enough to neglect the effects of this source of error in the rest of the work. In order to correct or analyze the positioning error in this case, more precise equipment would be needed, and this would be out of the scope of the project, because the current considerations are enough to validate the theoretical model.

6.3.2   Received signal error analysis

Both I_{sh} and I_{th} in 6.1 are zero-mean stochastic processes, while I_{Rx} and I_D are constant (slowly varying) signals. Hence, by averaging the obtained results, the variance of the noise terms can be reduced. If N samples are obtained for every

measure taken in the experiment, the sample mean can be used as an estimator of the mean of the obtained measures.

$$\bar{V}_o = \frac{1}{N}\sum_{n=0}^{N-1} V_o^n = R_f I_{Rx} + R_f I_D + \frac{R_f}{N}\sum_{n=0}^{N-1} I_{sh}^n + I_{th}^n \tag{6.4}$$

V_0^n denotes the n-th oscilloscope voltage sample, and I_{sh}^n and I_{th}^n denote the shot noise and thermal noise currents taken in the n-th sample. The photodiode will be detecting optical signals that will generate currents that are several orders of magnitude greater than the dark current, so it can be neglected. The random variables I_{th}^n are all independent and normally distributed variables with variance given by

$$\sigma_{I_{th}}^2 = \frac{4kTB}{R_f} \tag{6.5}$$

It can be proved that the sum of all of them will be a normally distributed random variable as well, with a variance given by the sum of all the variances. And taking into account the multiplicative factor before the sum, the variance of the voltage signal generated by the thermal noise can be estimated as

$$\sigma_{\bar{V}_{th}}^2 = \frac{4kTBR_f}{N} \tag{6.6}$$

Shot noise, on the other hand, is a Poisson process, but the Poisson distribution will approximate a normal distribution when the photoelectron events cannot be individually detected (which will be the case, because the optical signal will carry a large amount of photons). The variance of the current generated by shot noise in this case can be calculated as

$$\sigma_{I_{sh}}^2 = 2qI_{Rx}B \tag{6.7}$$

Taking this into account, and performing the same analysis that was performed for the thermal noise, the variance of the

$$\sigma_{\bar{V}_{sh}}^2 = \frac{2qI_{Rx}BR_f^2}{N} \tag{6.8}$$

Both noise sources are independent, and thus, the variances can be added, resulting in a total noise voltage signal that can be estimated as

$$\sigma_{\bar{V}_0}^2 = \frac{\left(4kTR_f + 2qI_{Rx}R_f^2\right)B}{N} \tag{6.9}$$

In this work, 200 samples are taken for every measurement, thus reducing by a factor of 200 the variance of the voltage noise.

6.4   Data analysis

After all the measurements of the experiment have been obtained, the experimental power map will be compared to the simulated power map for the corresponding distribution. The exitance function of the mobile phone has been approximated as a rectangle of constant exitance, where the exitance is measured experimentally using a power meter. The exitance distribution of the diffuser excited by the LED lamp was measured directly over the surface of the diffuser using a narrow occluder (0.5° of Angle of View (AoV)), and the distribution shown in Figure B.25 was obtained. These exitance functions are used to simulate the power map at the distances where the measures were taken. The validation of the theoretical model will be based on the evaluation of a similarity metric between the experimental results and the simulated results. To evaluate the similarity between two 2D signals, several metrics could be used, such as the Structural Similarity Index Metric (SSIM), the Wasserstein metric (also called Earth mover's distance) or the Pearson correlation coefficient. The evaluation metric that will be used in this work to validate the model will be the Pearson correlation coefficient, because it is invariant under linear transformations of the images. For images (2D signals), this coefficient is defined as

$$\rho = \frac{\sum_i \sum_j \left(\Phi_{sim} - \bar{\Phi}_{sim} \right) \left(\Phi_{exp} - \bar{\Phi}_{exp} \right)}{\sqrt{\left(\sum_i \sum_j \left(\Phi_{sim} - \bar{\Phi}_{sim} \right)^2 \right) \left(\sum_i \sum_j \left(\Phi_{exp} - \bar{\Phi}_{exp} \right)^2 \right)}} \tag{6.10}$$

A correlation value close to 1 will mean that the simulated and the measured power maps have a similar distribution, any correlation coefficient over 0.95 will be considered to show the similarity between the two images being compared. The correlation coefficient will be evaluated by calculating the cross correlation matrix between both power maps, and then extracting the maximum value. This value will be used in the formula of the Pearson coefficient to obtain the metric. This evaluation will be performed for every pair of simulated and experimental power maps.
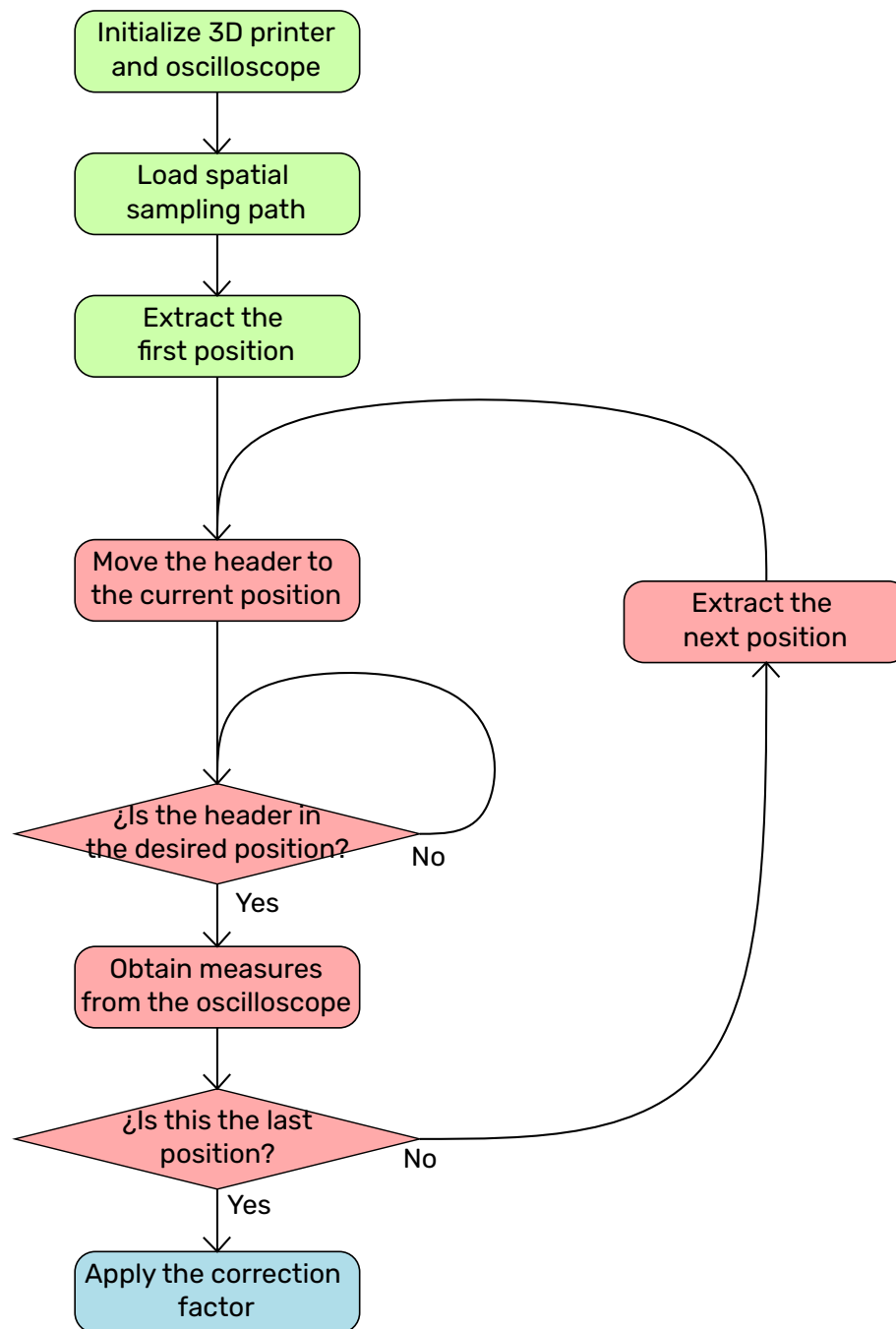
Figure 6.15: Flowchart of the experiment. The actions in green correspond to the initialization phase, the actions in red form the sampling routine, and the blue action is the multiplicative correction that must be applied to the sample.

Chapter 7

Results

In this chapter, the analysis of the comparison between the experimental and the simulated power maps will be presented. In addition, some considerations that were not taken into account in the description of the system will be discussed here.

7.1 Maximum shifted correlation as a function of distance

The Pearson correlation coefficient has been evaluated for the power maps obtained when the smartphone screen and the LED lamp are used as the source.

7.1.1 Smartphone screen

In Figure 7.3, the maximum correlation coefficients when no occluder is being used is shown (see Figures B.1, B.2, B.3, B.4, B.5 and B.6). When the 41.49° occluder is being used (scenario shown in Figures B.7, B.8, B.9, B.10, B.11 and B.12), the correlation is shown in Figure 7.4. The results for the 23.52° occluder (Figures B.13, B.14, B.15, B.16, B.17 and B.18), are shown in Figure 7.5. The last experiment of this batch was performed with the 13.78° occluder (Figures B.19, B.20, B.21, B.22, B.23 and B.24), and the correlation results are shown in Figure 7.6. As an example, the comparisons between simulated and experimental results are shown for the 23.52° occluder at a distance of 8.39 cm (Figure 7.1 and for the 13.78° occluder at a distance of 12.39 cm (Figure 7.2). The experimental values in the 13.72° scenario are affected by the precision of the measurement system.

The correlation values lie above the 0.95 threshold, which means that the simulated and measured power maps are almost the same (at least locally), the model has been proven to be close to the experimental results in this scenario. The source has been simulated from scratch (the exitance function was estimated to be a rectangular window). In the next section, the exitance function of the
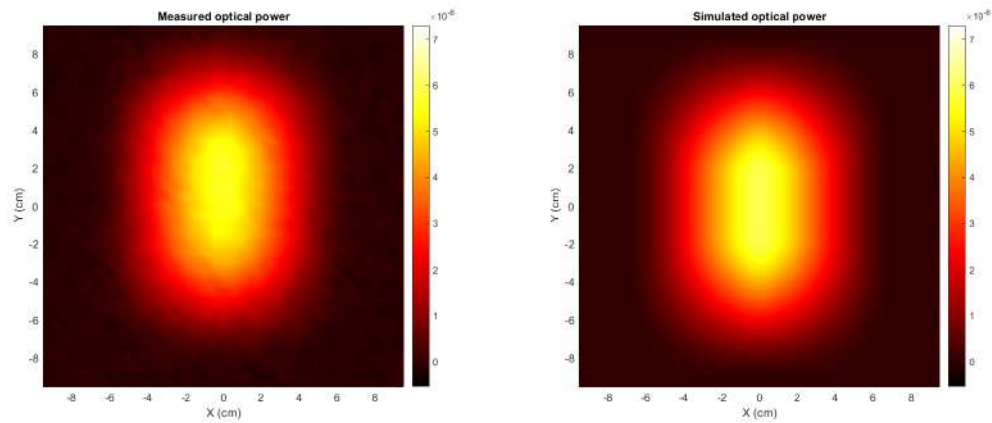
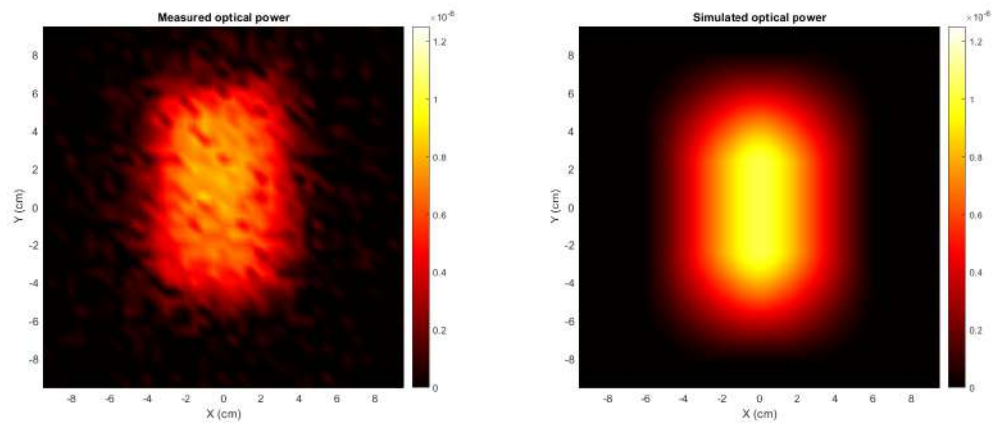Figure 7.1: Comparison between the experimental and simulated power with a 23.52° occluder at 8.39 cm.

Figure 7.2: Comparison between the experimental and simulated power with a 13.78° occluder at 12.39 cm.

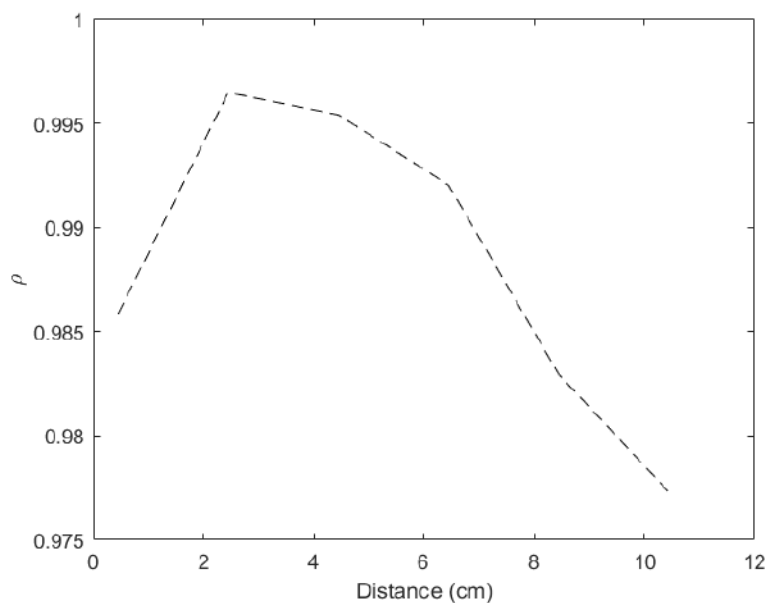source is obtained first, and this exitance is used as an input to the model to obtain the power maps.

Figure 7.3: Correlation of the power maps for the smartphone screen without occluder
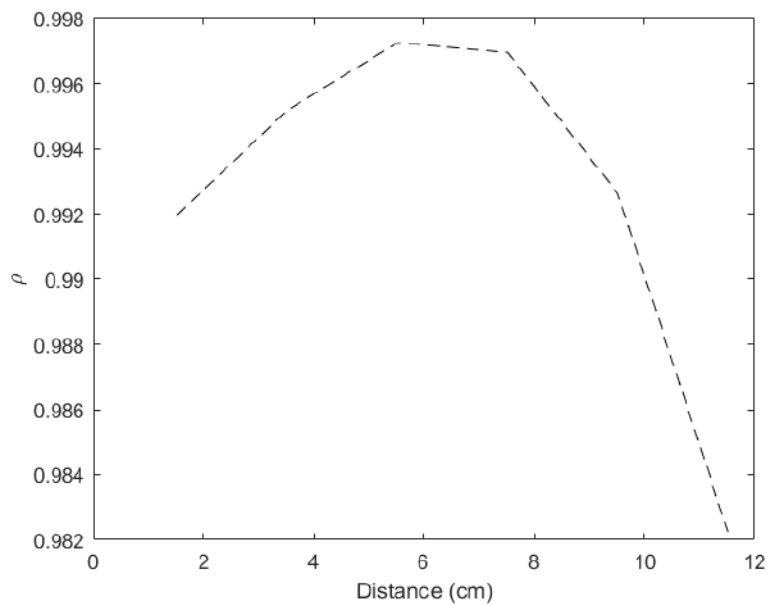

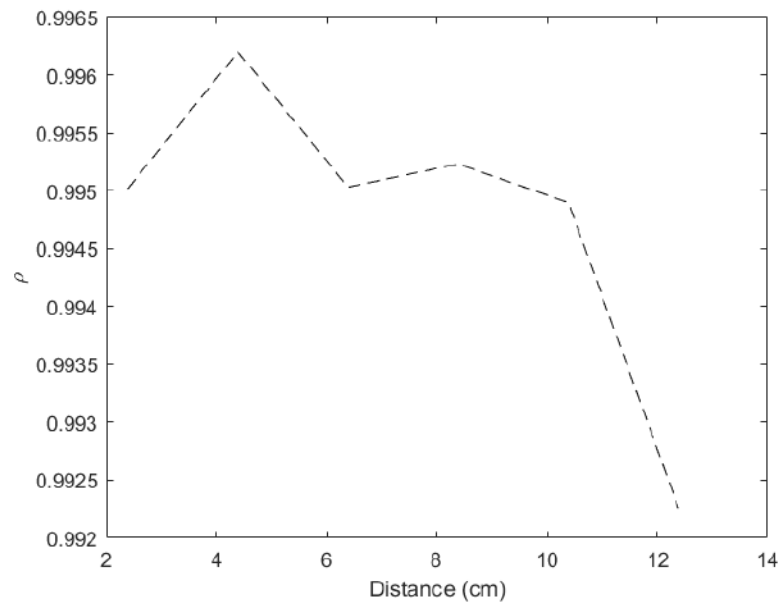Figure 7.4: Correlation of the power maps for the smartphone screen with the 41.49° occluder.

Figure 7.5: Correlation of the power maps for the smartphone screen with the 23.52° occluder.
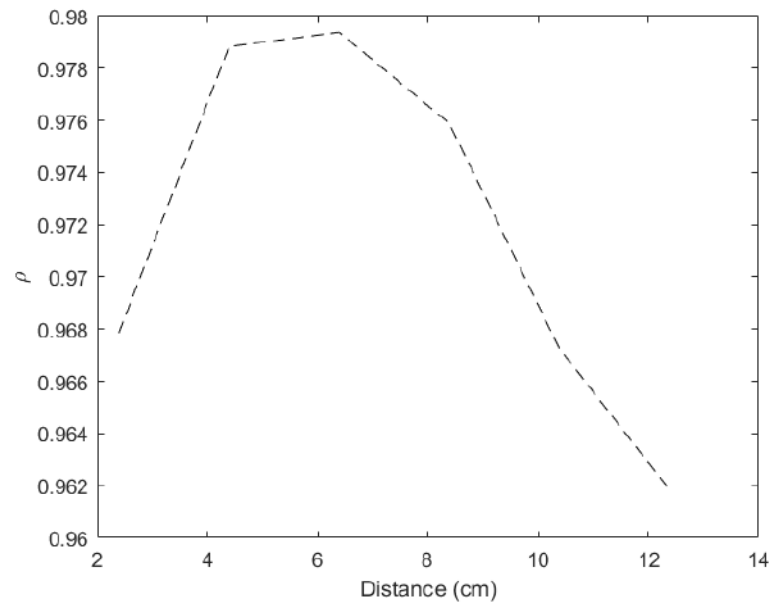
Figure 7.6: Correlation of the power maps for the smartphone screen with the 13.78° occluder.

7.1.2   LED array

In this scenario, the estimation of the behavior of the source was not as direct as in the smartphone screen case. The approach used in this work was to obtain a first measure of the exitance distribution over the diffuser slab (Figure 6.3. The result of this measurement is shown in Figure 7.7.
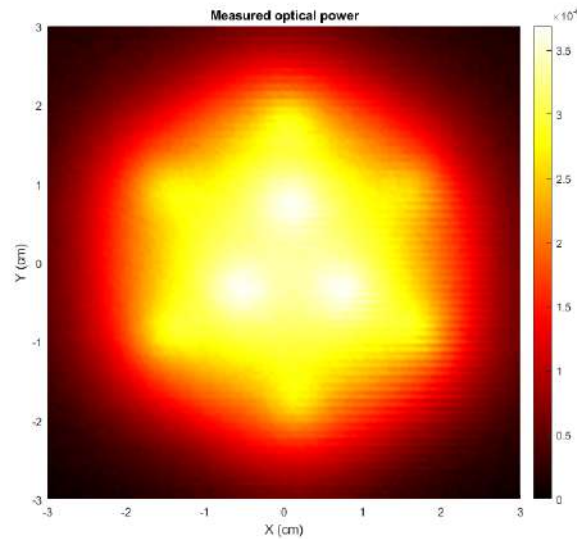
Figure 7.7: Power density near the diffuser excited with the LED lamp described in 6.

The same measurement protocol used for the screen was then executed and the results obtained are shown in Figures B.26 to B.43. The correlation values obtained in this experiment are above the threshold of 0.95 that was fixed in Chapter 6, except for the scenario without occluder at a distance of 10.45 cm, and the case where the 23.52° occluder was used, and a distance of 12.39 cm, these two scenarios are shown in Figures 7.8 and 7.9 respectively. However, the simulations in this experiment are based on an exitance function that was estimated with an experimental procedure, and this additional measurement is an additional source of error for the experiment that should be considered when the results are analyzed.
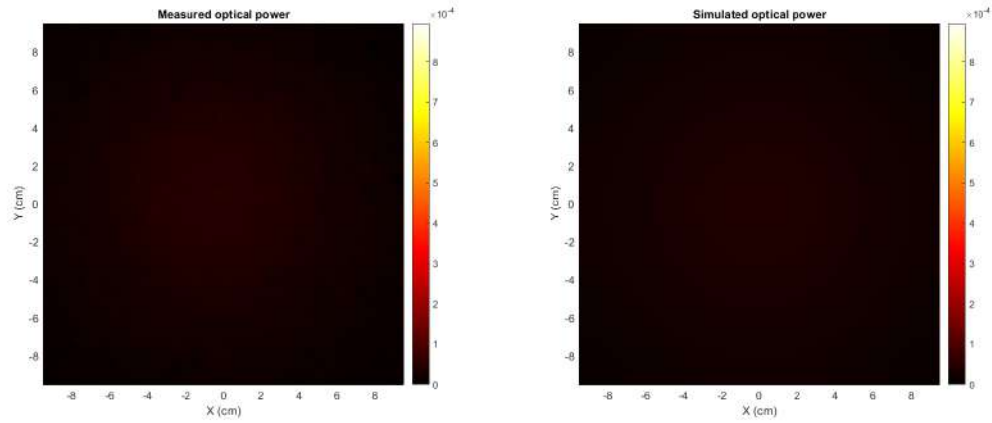
Figure 7.8: Comparison between the experimental and simulated power without occluder at 10.45 cm for the LED lamp
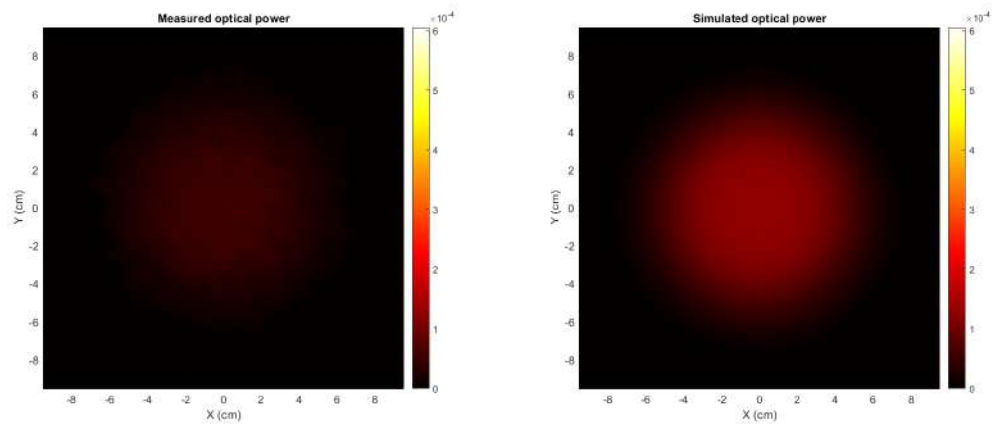

Figure 7.9: Comparison between the experimental and simulated power with a 23.52° occluder at 12.39 cm for the LED lamp
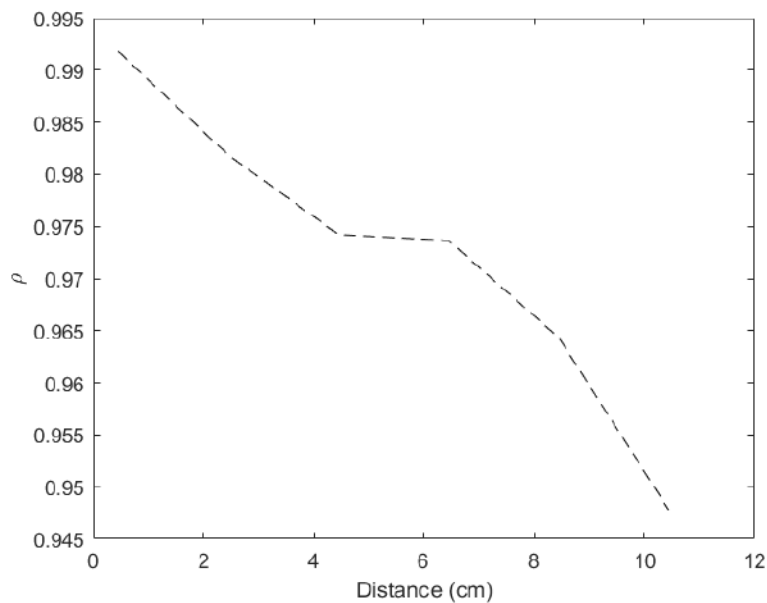
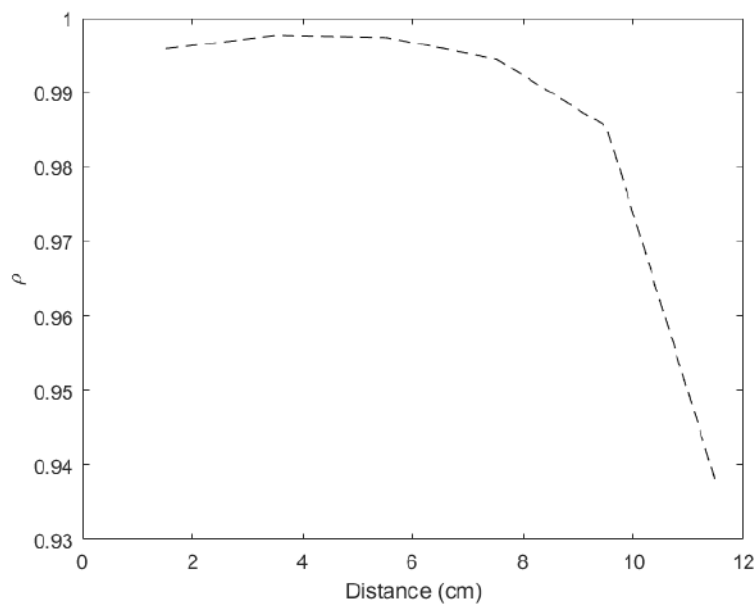Figure 7.10: Correlation of the power maps for the LED lamp without occluder.

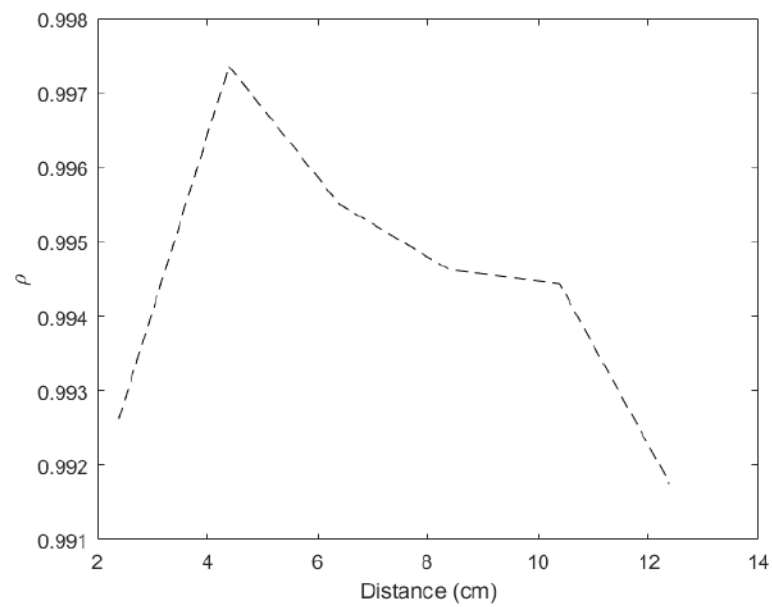Figure 7.11: Correlation of the power maps for the LED lamp with the 41.49° occluder.

Figure 7.12: Correlation of the power maps for LED lamp with the 23.52° occluder.

7.2   Issues with the occluder model

The analysis presented in the previous section used simulation results where the $g\left(\psi_{Rx}\right)$ function was approximated to be a step function, as shown in Figure 7.13.
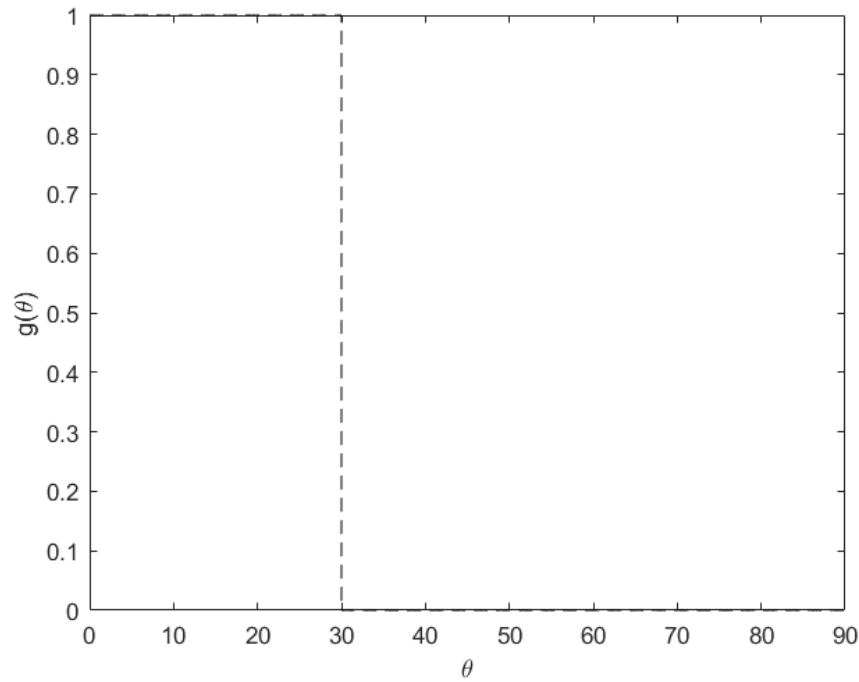
Figure 7.13: Ideal power transfer function (step function).

This will not be the behavior of the $g\left(\psi_{Rx}\right)$ in a real power transfer scenario, the truth is that the shape of this function will depend on the kind of optical system being used to limit the AoV of the receiver. In the case of the geometrical occluders used in this work, the following analysis considering incident plane waves coming from an infinite source can be performed (this will be a higher order approximation than the step function approach). The system has azimuthal symmetry, and because of this, only the elevation angle of incident rays must be considered. Suppose a source in the infinity radiation light that arrives at the geometrical occluder with an elevation angle θ. The aperture of the occluder will generate a shadow over the active area of the receiver (which will be considered circular for simplicity). The occluder will show three different behaviors depending on the angle of incidence of the light rays. If the angle of incidence is such that the aperture of the occluder does not generate any shadow on the active area, the received light will be maximum (there will be no losses, and $g\left(\theta\right) = 1$). If the incidence angle is such that the aperture generates a partial shadow, the received power will be proportional to the illuminated area of the receiver, this is, $g\left(\theta\right) = A_{illuminated}/A_{Rx}$. In the last region, if the aperture completely blocks the incident light, there will be no generated power, and thus, $g\left(\theta\right) = 0$. This way, the

behavior of the geometrical occluder will be approximated as

$$
g\left(\theta\right) = \begin{cases} 1 & \theta \leq \theta_1 \\ 1 - \dfrac{\text{arccos}\left(1-\frac{x_{Oc}}{r_{Rx}}\right)+\left(1-\frac{x_{Oc}}{r_{Rx}}\right)\sqrt{2x_{Oc}(r_{Rx}-x_{Oc})}}{\pi} & \theta_1 < \theta \leq \theta_2 \\ 0 & \theta_2 < \theta \end{cases} \tag{7.1}
$$

where

$$
x_{Oc} = h\tan\left(\frac{\pi}{2} - \theta\right) + r_{Rx} - r_{Ap}
$$

$$
\theta_1 = \text{arctan}\left(\frac{r_{Ap} - r_{Rx}}{h}\right)
$$

and

$$
\theta_2 = \text{arctan}\left(\frac{r_{Ap} + r_{Rx}}{h}\right)
$$

Where h is the height of the geometrical occluder, r_{Ap} is the radius of the aperture, and r_{Rx} is the radius of the active area of the receiver. For the occluders used in the experiment (and the geometrical occlusion generated by the photodiode), the $g\left(\psi_{Rx}\right)$ functions are shown in Figure 7.14
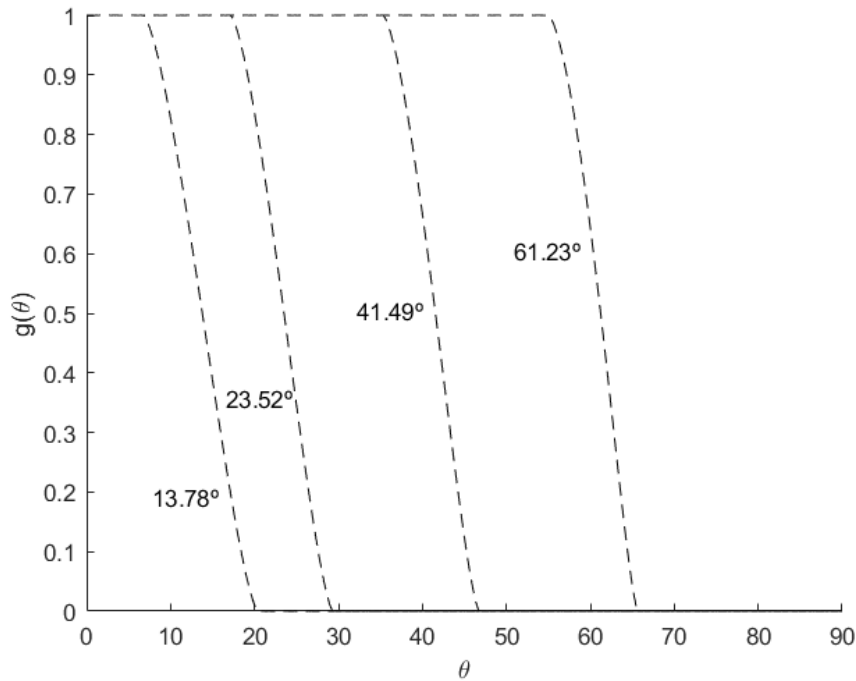
Figure 7.14: Power transfer functions of the studied scenarios.

7.3 Correlation using the corrected model of the occluder

In order to compare the results using the corrected occluder model with the results obtained with the step model, the simulations were performed and compared with the experimental data, and the correlation coefficient has been calculated. The correlation coefficients using the corrected occluder model are shown in Figures 7.15 to 7.18.
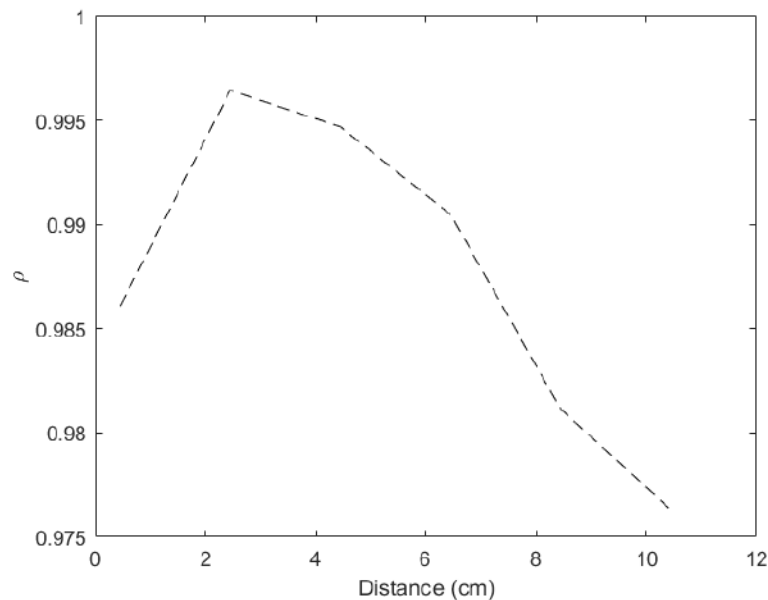

Figure 7.15: Correlation of the power maps for the smartphone screen without occluder, but considering the geometrical shadowing of the photodiode.

The values of the correlation coefficient suggest that the effects of approximating the behavior of the occluder as a step function are negligible (the values change slightly). The comparison between the experimental power maps and the simulated ones using the corrected occluder method are shown in Figures B.44 to B.67.
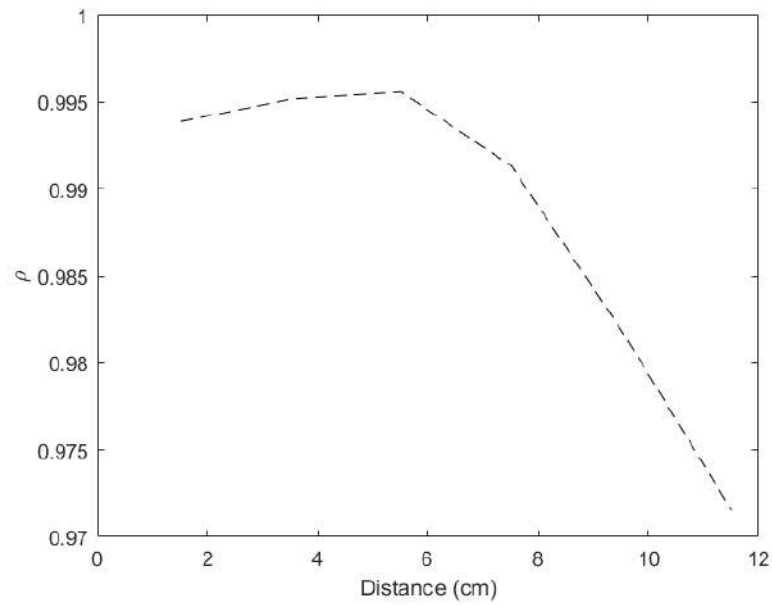
Figure 7.16: Correlation of the power maps for the smartphone screen with the 41.49° occluder using the shadowing model.
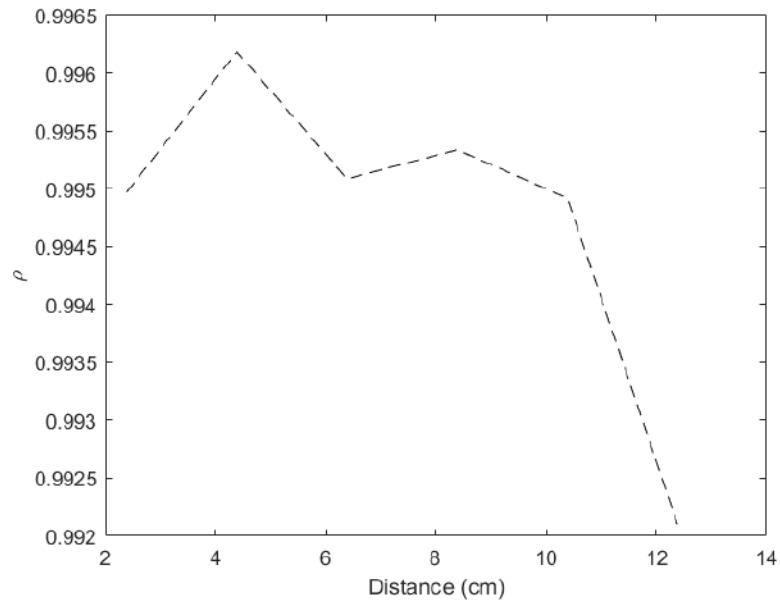
Figure 7.17: Correlation of the power maps for the smartphone screen with the 23.52° occluder using the shadowing model.
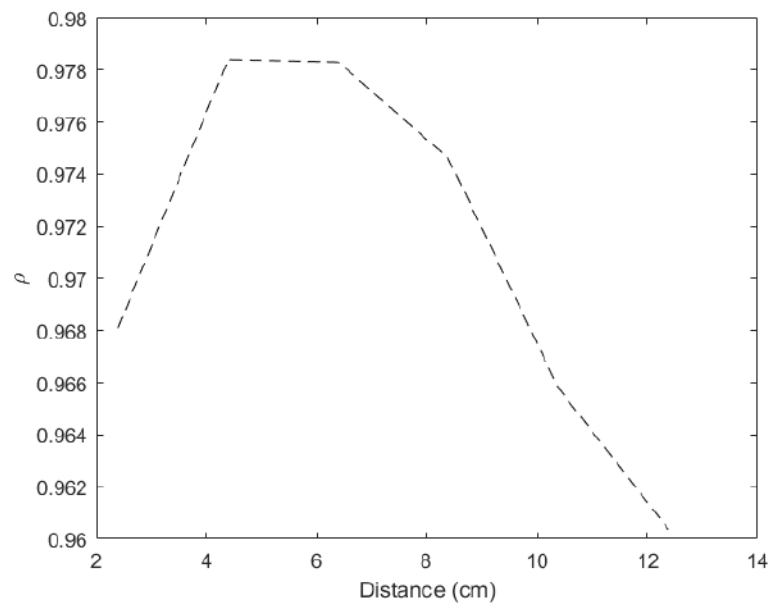
Figure 7.18: Correlation of the power maps for the smartphone screen with the 13.78° occluder using the shadowing model.

7.4   Constant power regions

The obtained power maps for the smartphone screen show an interesting property related to the spatial variation of the received optical power. In the regions of space where the source covers the Field of View (FoV) of the receiver, the integrated optical power shows a small variation. The geometry of this quasi-constant power region related to the geometry of the source, its lambertian coefficient m and the $g\left(\Phi_{Rx}\right)$ function of the receiver (which defines the AoV). Figures B.19 to B.24 give some insight about the existence of this constant power region (the yellow area in the center of the power maps). The precise mathematical relationship between the parameters of the source and the receiver that define this region has not been found in this work (it was not an objective of this project), but could be proposed as a future line. The interest in the existence of these constant power regions lies in the fact that it could be a powerful tool for the design engineer. If there is a coverage requisite in the design of an OWC system where the results of this work can be applied (direct link, control of the AoV and extended sources), the distribution of sources could be easily determined by setting the constant power region to be the desired coverage area, and then, through the mathematical relationship mentioned before, the distribution of the sources could be determined by posing an optimization problem.

7.5   General discussion

In brief, only two correlation values fall below the 0.95 threshold, and they are related to the experiment where the LED lamp excited diffuser was used. To obtain the exitance distribution in this case, an additional measurement was necessary, and this experimental distribution could be part of the explanation of the error obtained in this case. In Figures B.26 to B.43 (the diffuser experiment), it can be appreciated that there exists a slight difference in intensity between the experimental and simulated power maps, this could be caused by an error in the measurement of the distance respect to the source plane. Relative to the temporal duration of the experiments, in the first iterations of the measurement system, an experiment lasted for 4 hours, but by minimizing the idle times of the oscilloscope and the mechanical system, the measurement routine duration could be reduced to around 1 hour to obtain the power maps at six different distances. This was the case for every source and receiver configuration, except for the routine used to evaluate the exitance of the LED excited diffuser, which required a finer sampling along the source plane, and the experiment had a duration of 3 hours (after the optimization of the idle times). A further optimization of the duration of the experiment could be obtained by using more sophisticated synchronization schemes between the oscilloscope and the 3D printer, but it would involve modifying the firmware of the printer, and this was avoided in this work because it would fall out of the scope of the project.

Chapter 8

Conclusions

In this chapter, some comments about the applicability and the generalization potential of the models obtained in this work are presented, as well as a brief analysis of the main limitations of this work. After that, some future lines are proposed as a continuation to the work of this project, and in the final section, some final remarks are stated about the project.

8.1 Generalizations

According to the results exposed in the previous chapter, the mathematical models of Chapter 3 can be used to approximate the behavior of the DC component of an OWC channel if the AoV of the receiver is known, the source can be modelled as a surface in any of the ways described in this work and behaves like a lambertian radiator, and only the direct link component is of interest. The model was tested with two different sources which fulfill the mentioned conditions: a smarphone screen and a LED lamp with a diffuser. Further aspects could be introduced in the models of Chapter 3 to include more complex situations (shadowing, complex catadioptric systems, or the existence of a refractive index gradient, which would curve the light rays, could be some examples of phenomena that could be included in the models after doing some modifications).

8.2 Limitations

Even though the obtained results are mainly positive, there are some aspects that must be addressed about this work. In first place, real-world optical sources do not always fulfill the separability condition given by (3.12). This would be the case of a TV screen, which could be approximated as a continuous surface distribution according to the arguments given at the beginning of Chapter 3, but the exitance distribution will have local time variations. In this case, equation (3.15) would have to be modified to include the local time variations of the source, and the rest of the results of Chapter 3 would have to be analyzed again. Another flaw is also

related to the integral in (3.15). The integration in this equation is very complex in a general way, and would require heavy computation to obtain results. On the other hand, the measurement system was built using an existing 3D printer, and the design was conditioned to the operation of this part of the system. The 3D printer implements a 3 DoF mechanical system, and this conditions the measurements that could be taken. A 5 DoF system would be needed in order to validate the spherical and cylindrical models with normal receiver orientation described in Chapter 3. Another aspect that must be taken into account is the selection of the similarity measure. In this work, Pearson correlation coefficient was selected, but there could exist better measures of the similarity of the experimental and simulated power maps.

8.3   Future work

Taking into account the obtained results and the limitations of the models and the implemented system, the following future research lines are proposed as a continuation to the work presented in this report:

- Study of the effects of shadowing due to an obstacle in the power transfer problem.

- Development of a MIMO model for multiple extended sources.

- Development and implementation of positioning schemes based on the properties of the obtained models.

- Development of detection and ranging schemes based on the properties of the model.

- Application of the model in the design of physical experiments.

- Modification of the model to the OCC scenario (this is related to the development of a MIMO model).

- Development of a 5 DoF mechanical system to allow the validation of the circular and cylindrical models.

- Development of a measurement system that allows the validation of the time-dependant model.

- Design of a larger mechanical system to allow the evaluation of power maps in indoor scenarios.

8.4 Final remarks

In this work, a thorough analysis of some particular cases of the optical power transmission problem has been presented. After a general introduction, some closed–form expressions have been derived for the flat source, spherical source and cylindrical source scenarios, and possible applications have been briefly described. In the second half of this work, the focus was the validation of the flat source model. With this in mind, a measurement system based on the mechanical structure of a 3D printer was implemented, and three experiments were carried out when the implementation was finished. The results of the experiment told that the mathematical models described in Chapter 3 conform a close approximation to the actual received power maps, at least in the studied scenarios. This report concludes with the certainty that each and every of the goals stated for this project have been successfully fulfilled.

Appendices

Appendix A

Differential geometry fundamentals

Chapter 3 makes an extensive use of differential geometry jargon and results. In order to make the derivations easier to understand, in this appendix, some of the basic terminology and results of differential geometry are shown.

A.1 Basic definitions

A n-manifold A is a topological space that behaves locally as the space $\mathbb{R}^n$. This means that there exists a family of injective maps that transform a subset of $\mathbb{R}^n$ into a subset of A. One of those maps is said to be a Monge chart (or explicit chart) if one of the coordinates is described as a function of the other coordinates, which are the cartesian coordinates of the manifold. In the case of a surface in $\mathbb{R}^3$, this would mean that one of the cartesian coordinates of the surface is a function of the two other coordinates. If the free coordinates are named x and y, the position of any point over the surface can be described using a vector $\boldsymbol{r} = (x, y, f(x, y))$. The normal vector of the surface can be calculated in this case as

$$\boldsymbol{n} = \frac{\boldsymbol{r}_x \times \boldsymbol{r}_y}{|\boldsymbol{r}_x \times \boldsymbol{r}_y|} \tag{A.1}$$

The vector product of the partial derivatives can be obtained as

$$\boldsymbol{r}_x \times \boldsymbol{r}_y = (\boldsymbol{u}_x + f_x \boldsymbol{u}_z) \times (\boldsymbol{u}_y + f_y \boldsymbol{u}_z) = \boldsymbol{u}_z - f_x \boldsymbol{u}_x - f_y \boldsymbol{u}_y \tag{A.2}$$

And then, the normal vector can be obtained as

$$\boldsymbol{n} = \frac{\boldsymbol{u}_z - f_x \boldsymbol{u}_x - f_y \boldsymbol{u}_y}{\sqrt{1 + (f_x)^2 + (f_y)^2}} \tag{A.3}$$

The cosine of the angle formed by a straight line and the normal vector of a surface can be obtained if the unit vector of the line, $\boldsymbol{u}_d$, is known

$$\cos(\theta) = \boldsymbol{u}_d \cdot \boldsymbol{n} \tag{A.4}$$

The measures along the surface (distances, areas, angles) are related to a bilinear form that receives the name of first fundamental form. The coefficients of the matrix of the first fundamental form depend on the choice of coordinates of the manifold. For a given coordinate chart r, the matrix of the first fundamental form is

$$I_P = \begin{pmatrix} \boldsymbol{r}_x \cdot \boldsymbol{r}_x & \boldsymbol{r}_x \cdot \boldsymbol{r}_y \\ \boldsymbol{r}_y \cdot \boldsymbol{r}_x & \boldsymbol{r}_y \cdot \boldsymbol{r}_y \end{pmatrix} \tag{A.5}$$

The area of an infinitesimal region of the surface can be obtained as

$$\mathsf{d}S = |\boldsymbol{r}_x \times \boldsymbol{r}_y|\,\mathsf{d}x\mathsf{d}y = \sqrt{|\boldsymbol{r}_x|^2 + |\boldsymbol{r}_y|^2 - (\boldsymbol{r}_x \cdot \boldsymbol{r}_y)^2}\mathsf{d}x\mathsf{d}y = \sqrt{\mathsf{det}\,(I_P)}\mathsf{d}x\mathsf{d}y \tag{A.6}$$

A.2   Integration over manifolds

For a function $h(u,v)$ defined over a manifold, the integral of this function along a region of the manifold can be expressed as

$$\iint_{S_o} h(u,v)\,\mathsf{d}S \tag{A.7}$$

In order to express the area differential as a product of u and v differentials, the first fundamental form must be calculated. Once it has been calculated, the area differential can be expressed as

$$\mathsf{d}S = \sqrt{\mathsf{det}\,(I_P)}\mathsf{d}u\mathsf{d}v \tag{A.8}$$

In the case of a monge chart, the square root of the determinant of the fundamental form can be expressed as

$$\mathsf{d}S = \sqrt{1 + (f_u)^2 + (f_v)^2}\mathsf{d}u\mathsf{d}v \tag{A.9}$$

Thus, the integral of the function along a certain region of the surface can be expressed as

$$\iint_{S_o} h(u,v)\,\mathsf{d}S = \iint_{S_o} h(u,v)\sqrt{1 + (f_u)^2 + (f_v)^2}\mathsf{d}u\mathsf{d}v \tag{A.10}$$

Appendix B

Measurements and simulations

In this appendix, the measured and simulated power values will be shown as a support for the results and conclusions stated in the main document. The format of all the figures in this appendix is the same (experimental data at the left, and simulated data at the right), except for Figure B.25, which only shows the measured exitance of the LED array.

B.1 Smartphone screen

B.1.1 Receiver without occluder
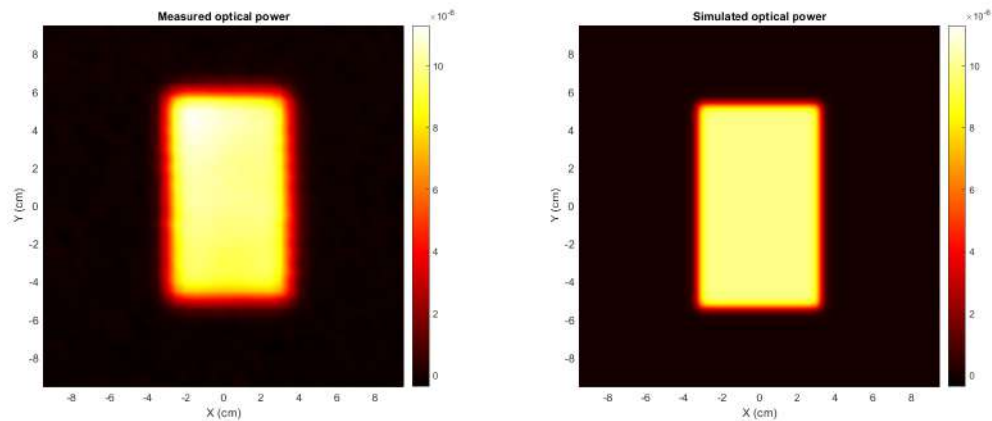
Figure B.1: Comparison between the experimental and simulated power without occluder at 0.45 cm.
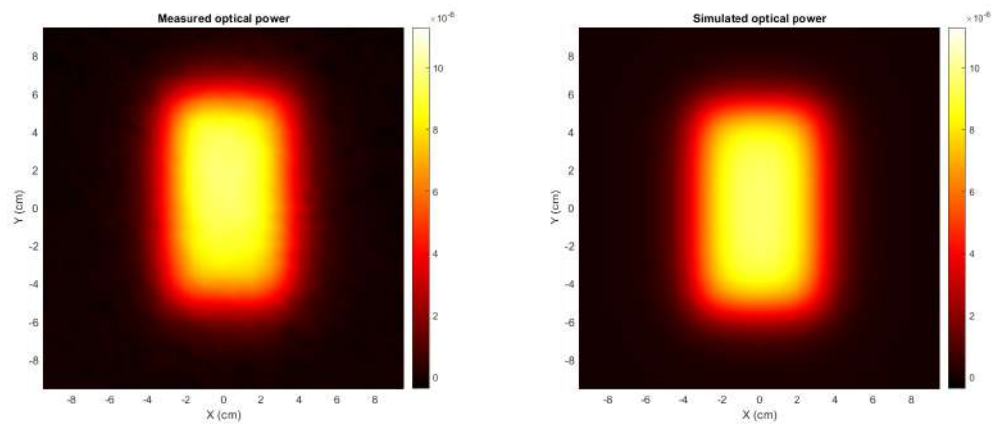
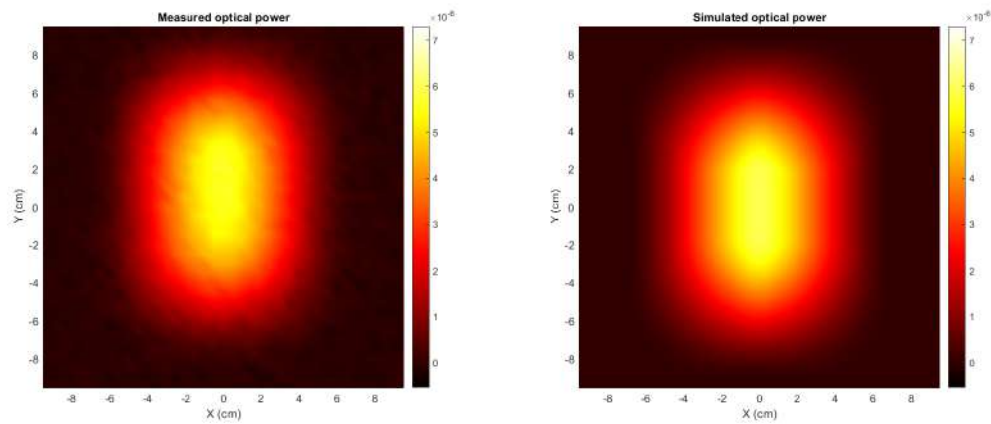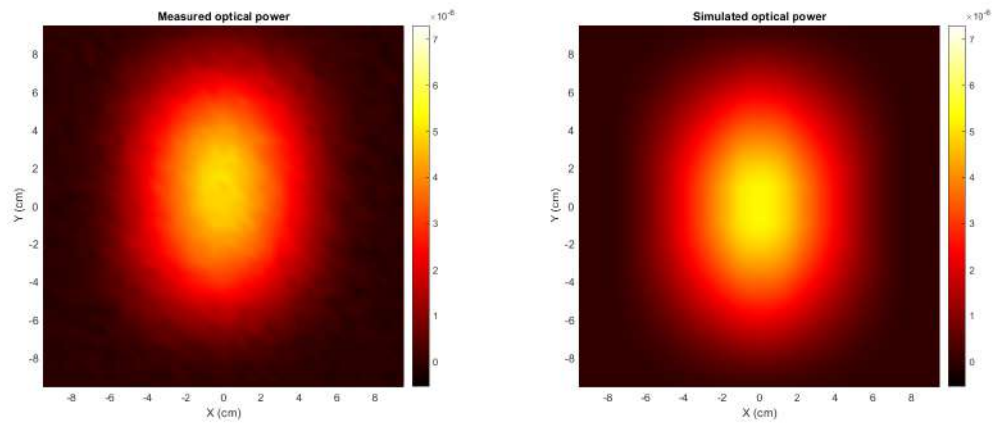
Figure B.2: Comparison between the experimental and simulated power without occluder at 2.45 cm.
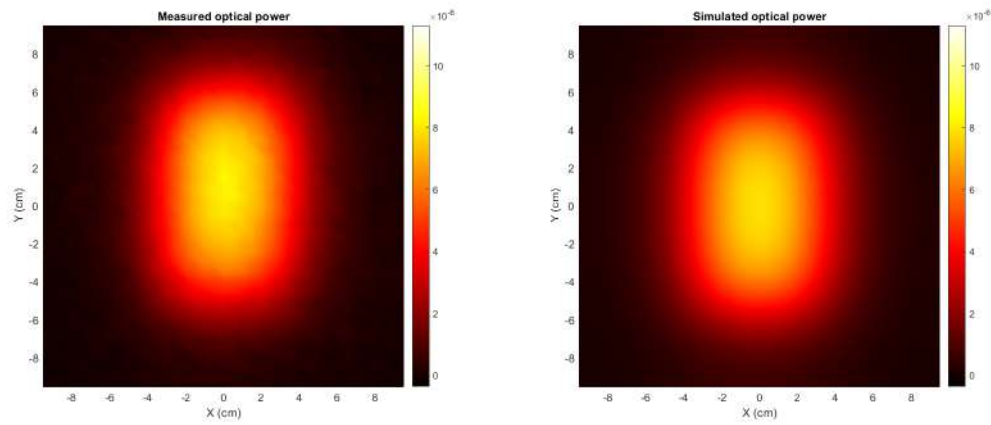
Figure B.3: Comparison between the experimental and simulated power without occluder at 4.45 cm.
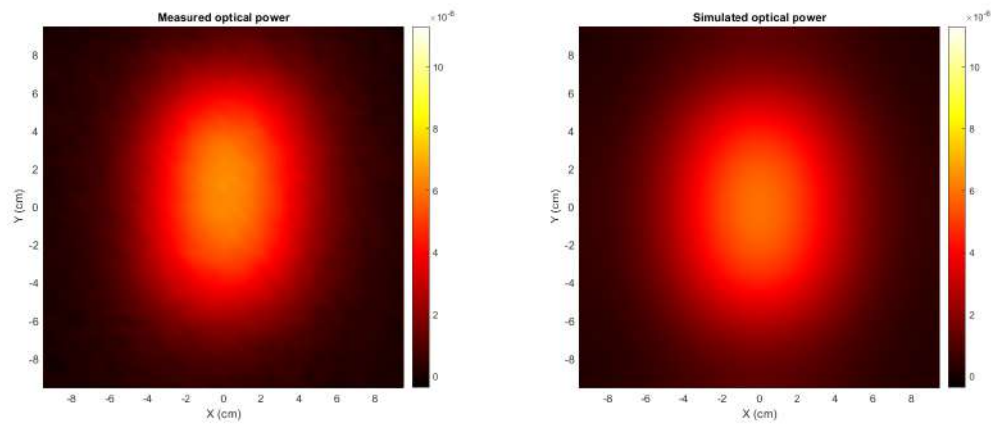
Figure B.4: Comparison between the experimental and simulated power without occluder at 6.45 cm.
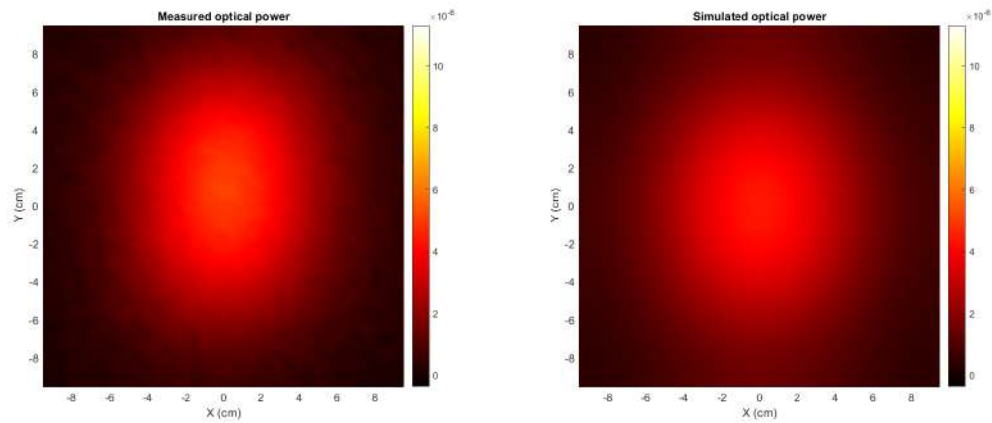
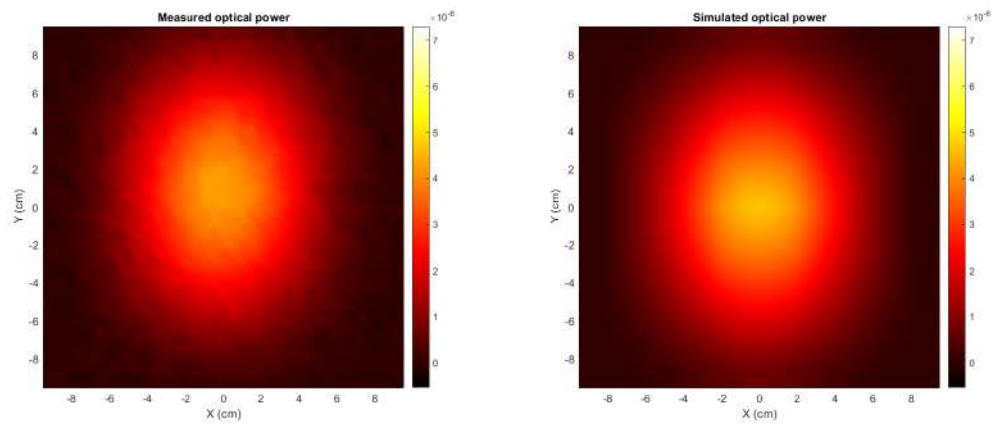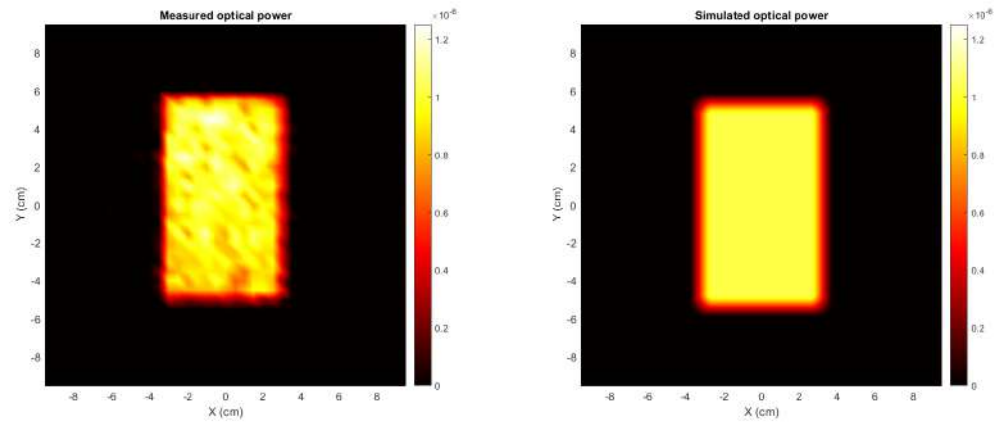Figure B.5: Comparison between the experimental and simulated power without occluder at 8.45 cm.
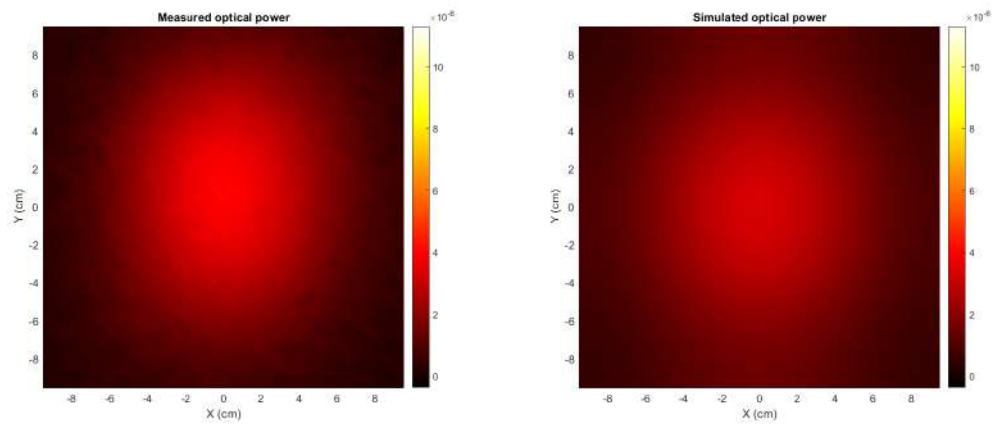
Figure B.6: Comparison between the experimental and simulated power without occluder at 10.45 cm.
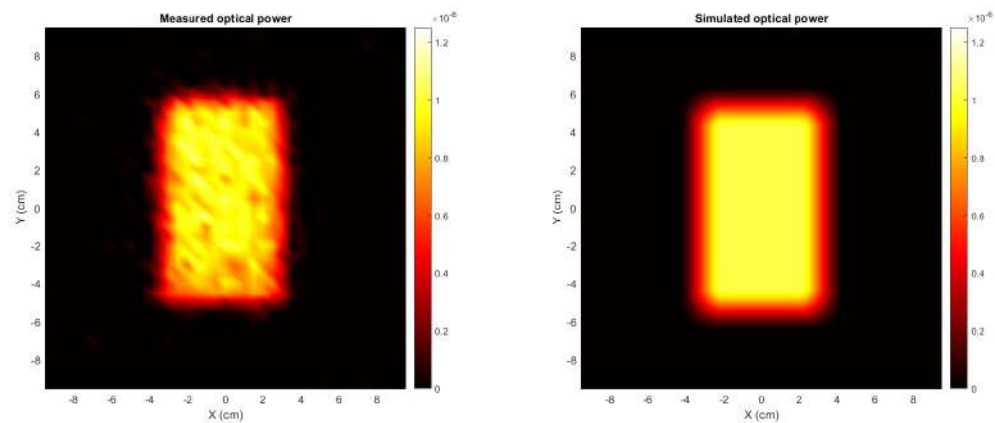
B.1.2   Receiver with 41° occluder
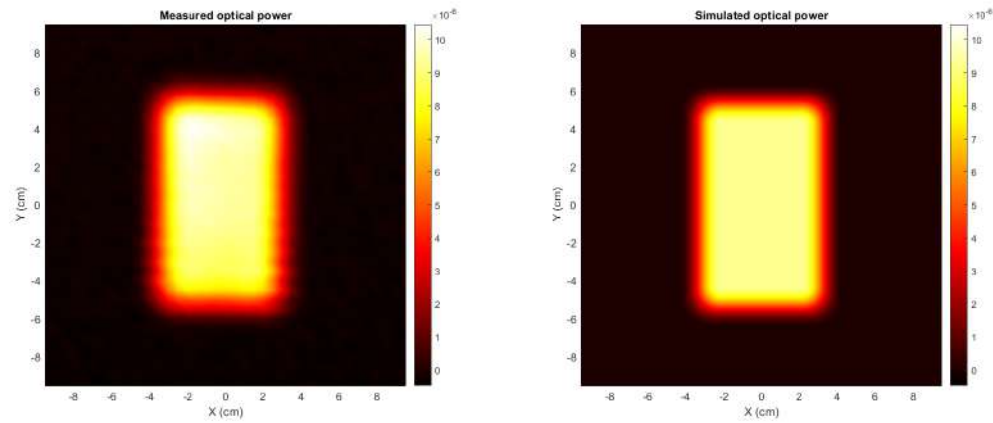
Figure B.7: Comparison between the experimental and simulated power with a 41.49° occluder at 1.52 cm.
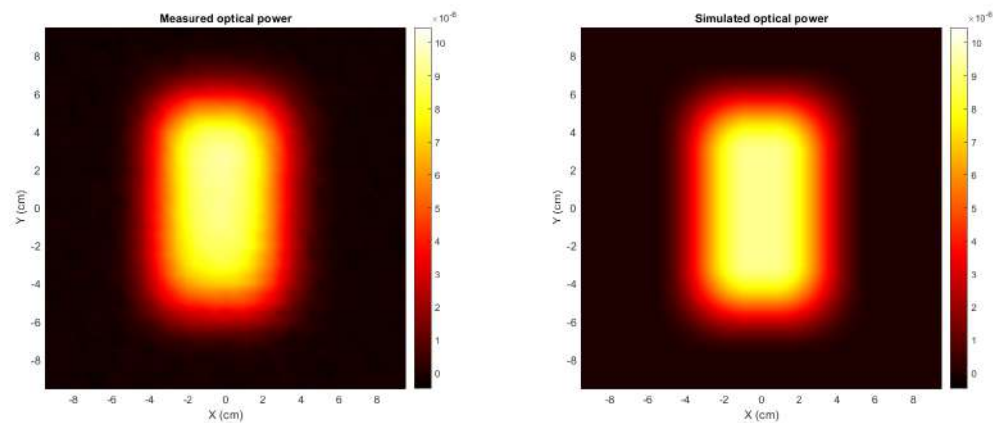
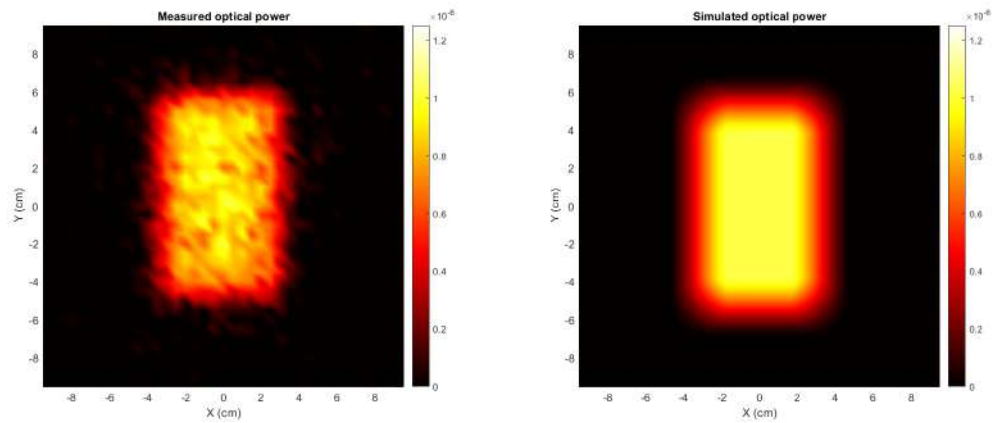Figure B.8: Comparison between the experimental and simulated power with a 41.49° occluder at 3.52 cm.
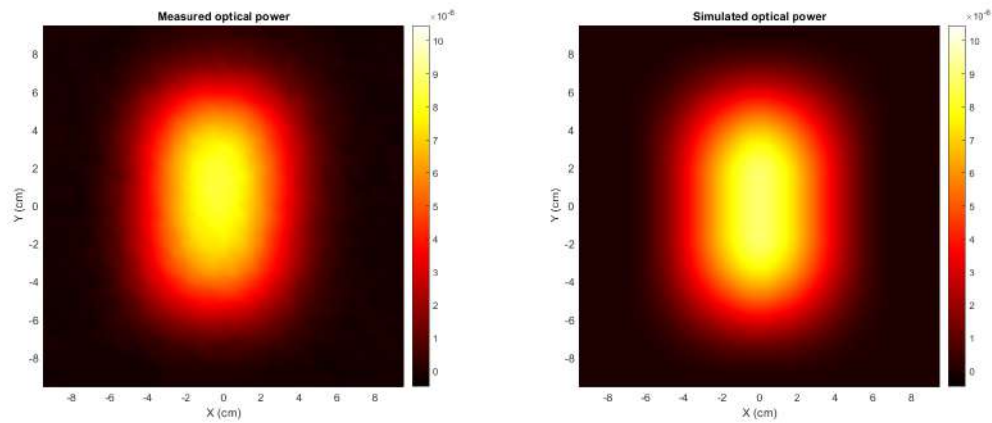
Figure B.9: Comparison between the experimental and simulated power with a 41.49° occluder at 5.52 cm.
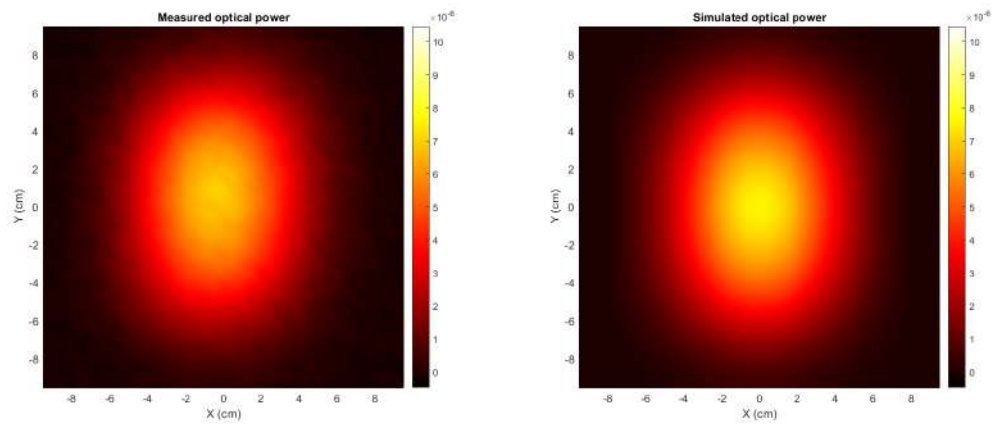
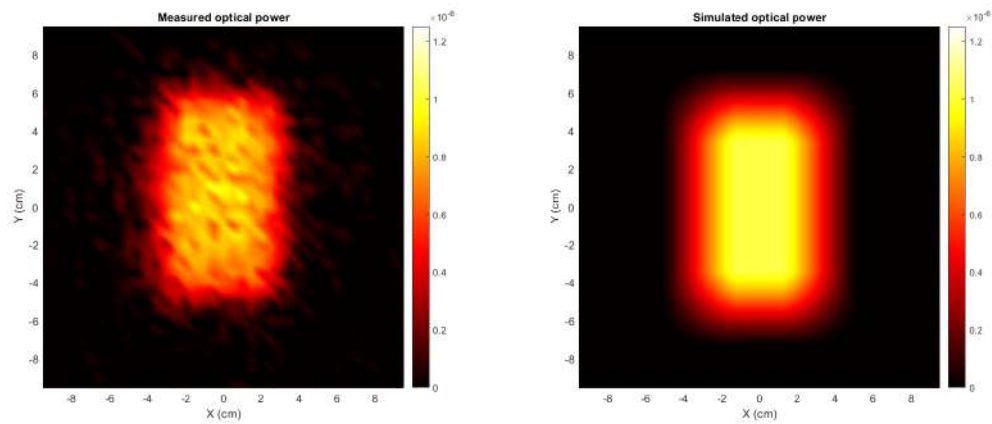Figure B.10: Comparison between the experimental and simulated power with a 41.49° occluder at 7.52 cm.
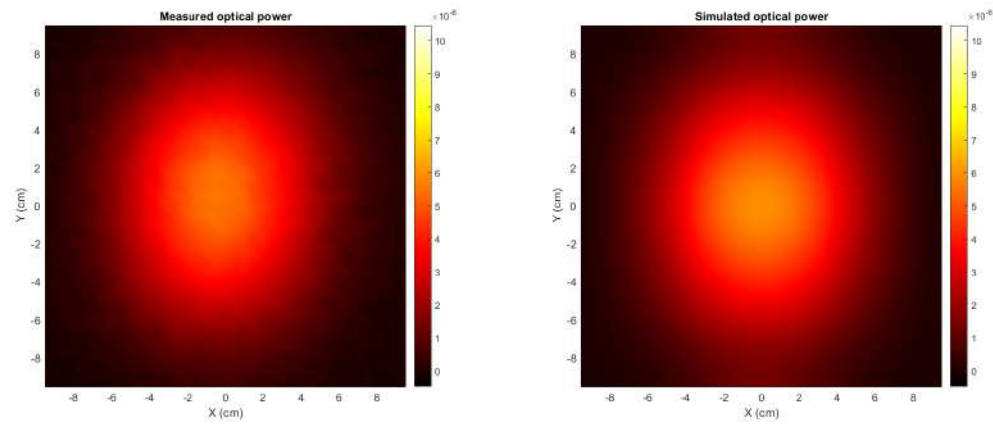
Figure B.11: Comparison between the experimental and simulated power with a 41.49° occluder at 9.52 cm.
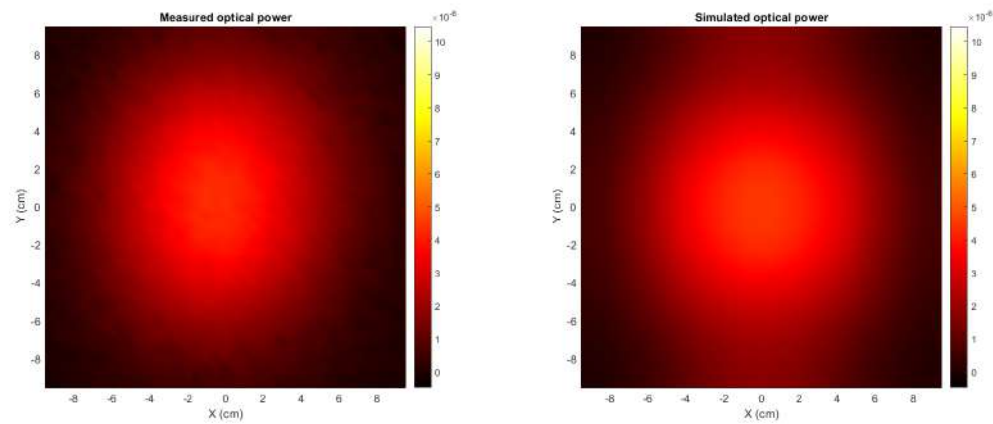
Figure B.12: Comparison between the experimental and simulated power with a 41.49° occluder at 11.52 cm.
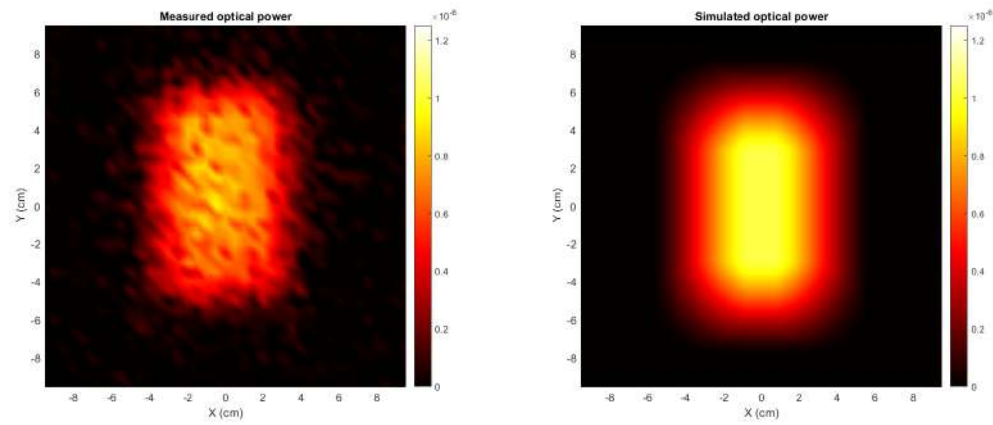
B.1.3   Receiver with 23° occluder
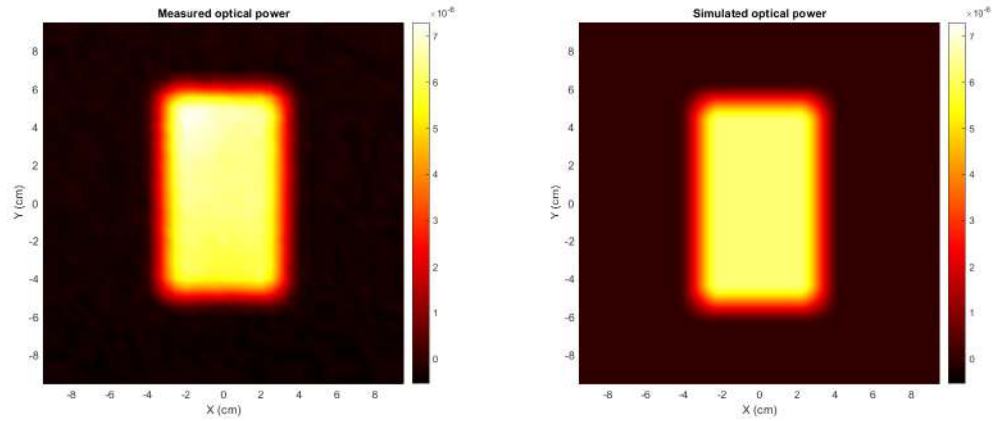
Figure B.13: Comparison between the experimental and simulated power with a 23.52° occluder at 2.39 cm.
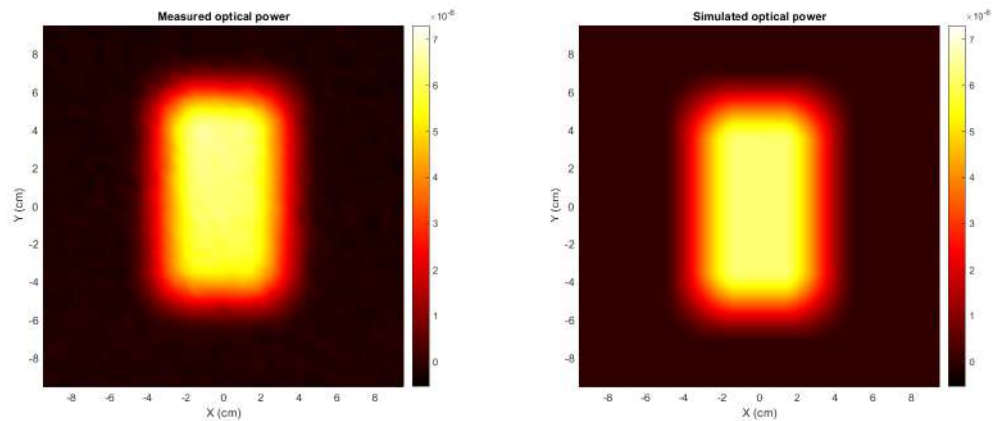
Figure B.14: Comparison between the experimental and simulated power with a 23.52° occluder at 4.39 cm.
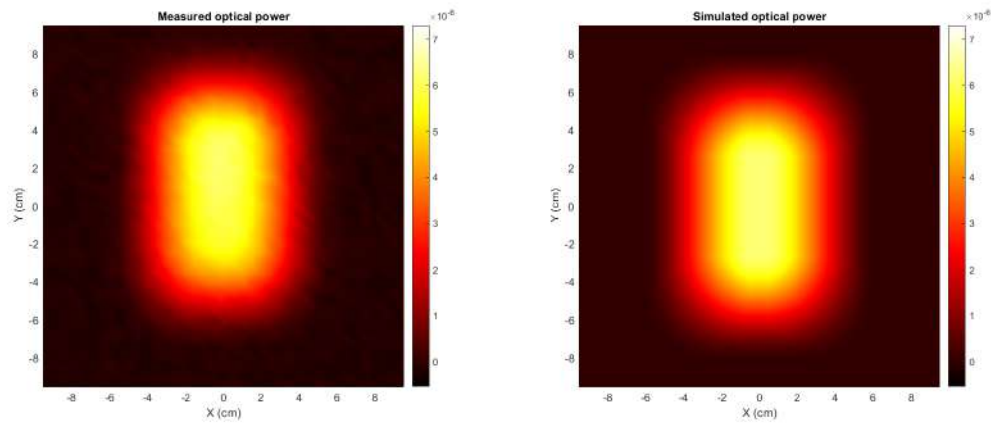
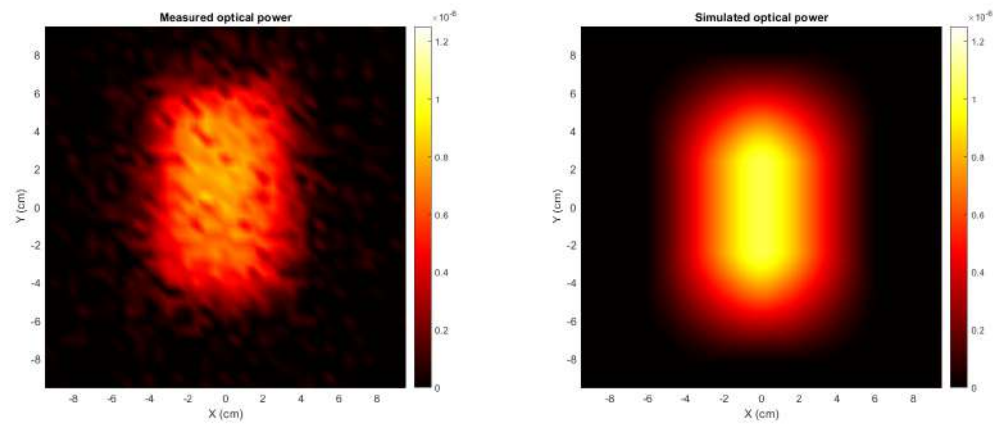Figure B.15: Comparison between the experimental and simulated power with a 23.52° occluder at 6.39 cm.

Figure B.16: Comparison between the experimental and simulated power with a 23.52° occluder at 8.39 cm.

Figure B.17: Comparison between the experimental and simulated power with a 23.52° occluder at 10.39 cm.

Figure B.18: Comparison between the experimental and simulated power with a 23.52° occluder at 12.39 cm.

B.1.4   Receiver with 13° occluder

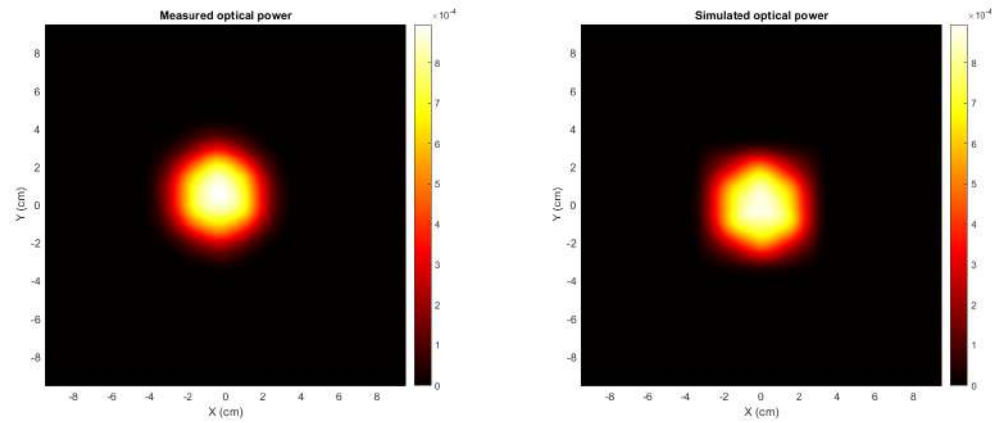Figure B.19: Comparison between the experimental and simulated power with a 13.78° occluder at 2.39 cm.

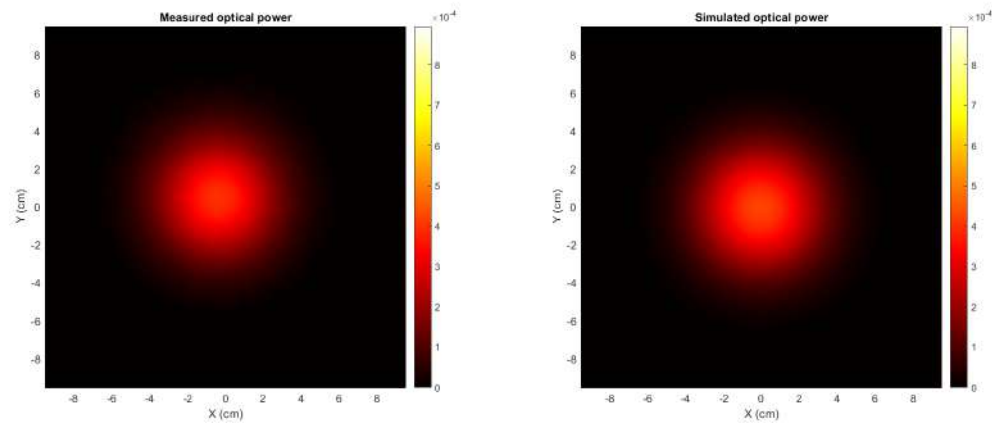Figure B.20: Comparison between the experimental and simulated power with a 13.78° occluder at 4.39 cm.

Figure B.21: Comparison between the experimental and simulated power with a 13.78° occluder at 6.39 cm.

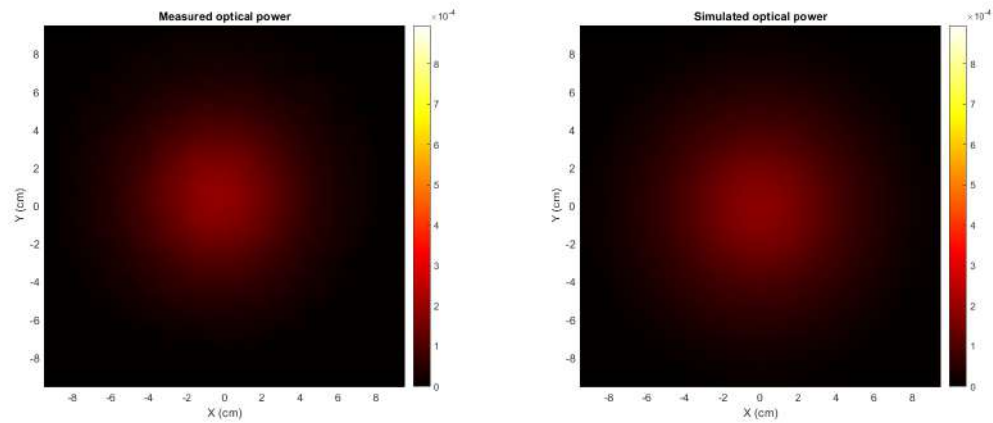Figure B.22: Comparison between the experimental and simulated power with a 13.78° occluder at 8.39 cm.

Figure B.23: Comparison between the experimental and simulated power with a 13.78° occluder at 10.39 cm.

Figure B.24: Comparison between the experimental and simulated power with a 13.78° occluder at 12.39 cm.

B.2   LED array

B.2.1   Measurement of the exitance with a 0.5° occluder

The exitance of the diffuser excited by the LED lamp was measured using the 0.5° occluder that is shown in Figure 6.4 with a different colour.
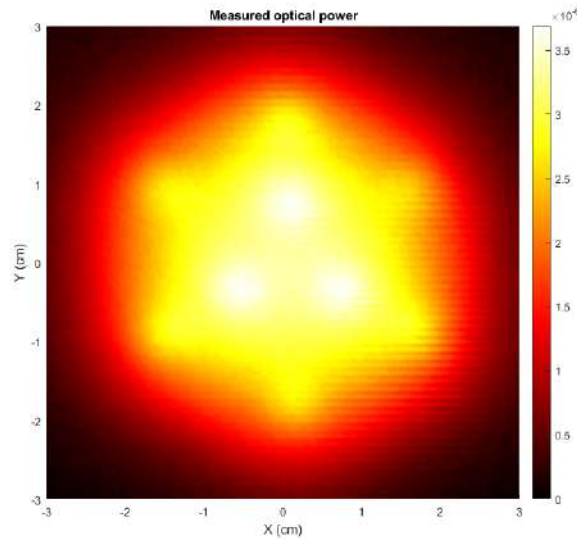
Figure B.25: Power density near the diffuser excited with the LED lamp described in 6.

B.2.2   Receiver without occluder

Figure B.26: Comparison between the experimental and simulated power without occluder at 0.45 cm for the LED lamp

Figure B.27: Comparison between the experimental and simulated power without occluder at 2.45 cm for the LED lamp

Figure B.28: Comparison between the experimental and simulated power without occluder at 4.45 cm for the LED lamp
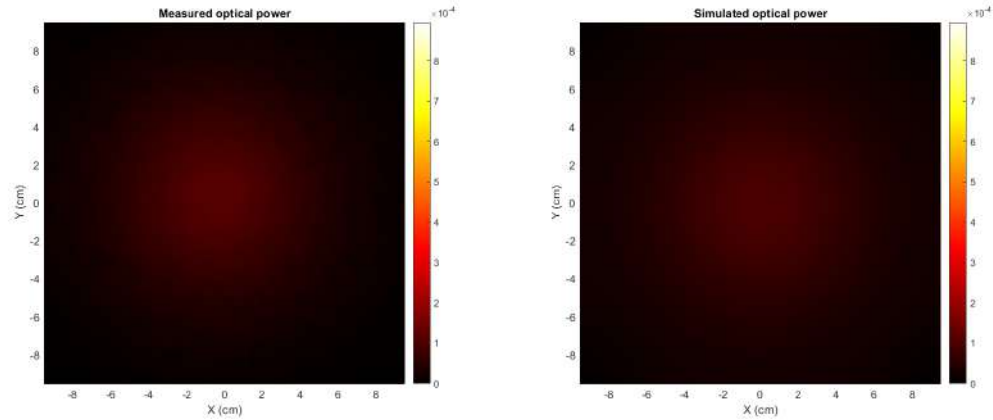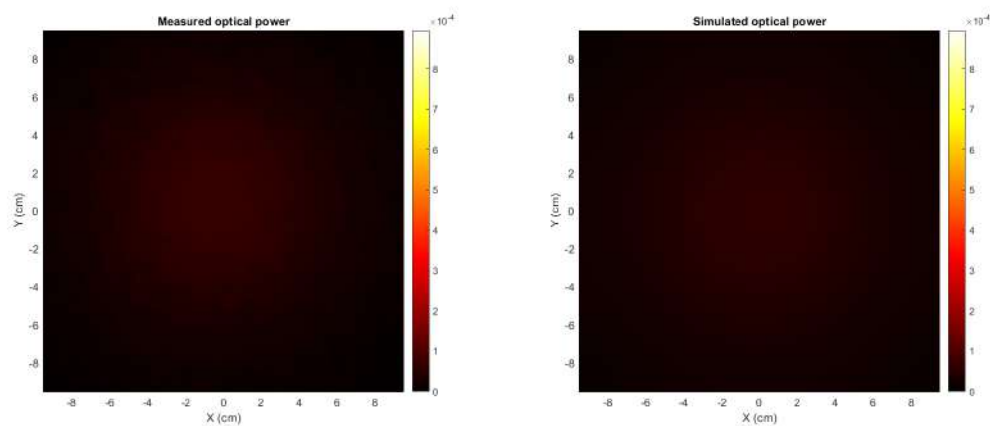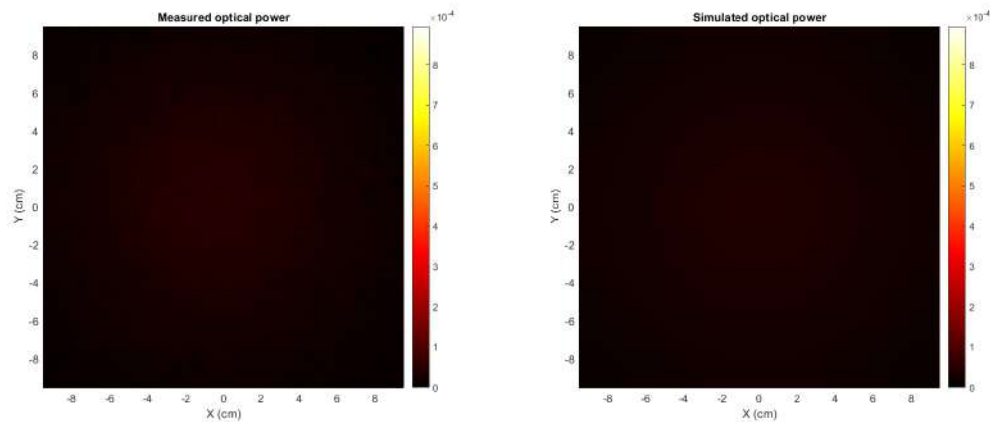

Figure B.29: Comparison between the experimental and simulated power without occluder at 6.45 cm for the LED lamp

Figure B.30: Comparison between the experimental and simulated power without occluder at 8.45 cm for the LED lamp

Figure B.31: Comparison between the experimental and simulated power without occluder at 10.45 cm for the LED lamp

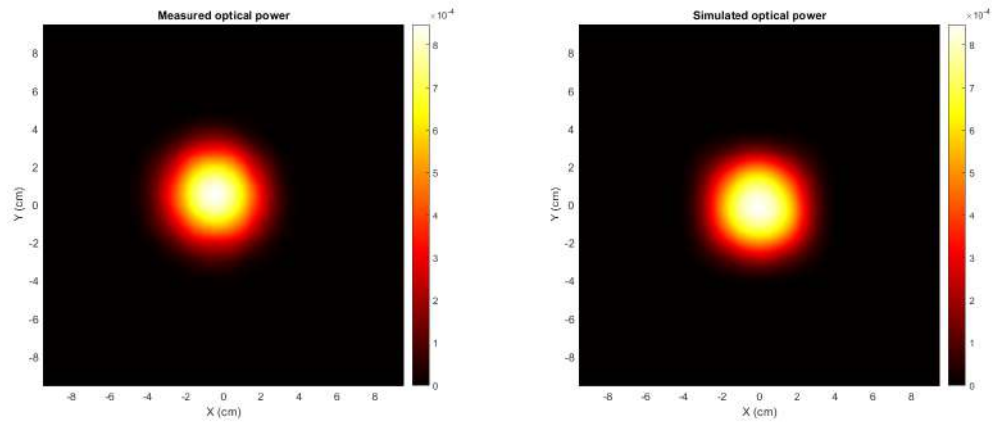## B.2.3   Receiver with 41° occluder

Figure B.32: Comparison between the experimental and simulated power with a 41.49° occluder at 1.52 cm for the LED lamp
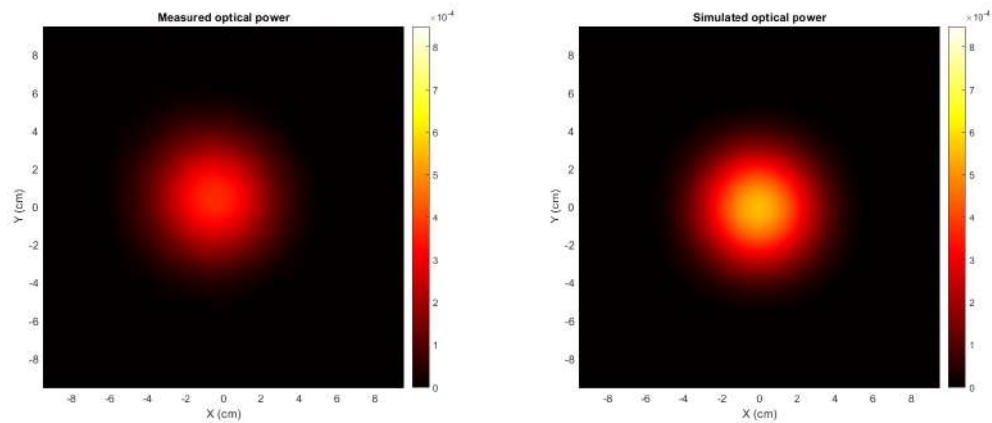

Figure B.33: Comparison between the experimental and simulated power with a 41.49° occluder at 3.52 cm for the LED lamp
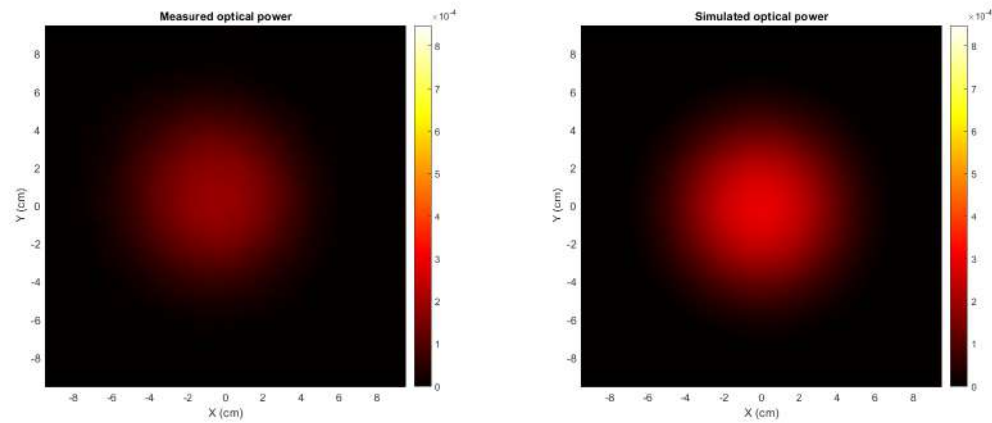
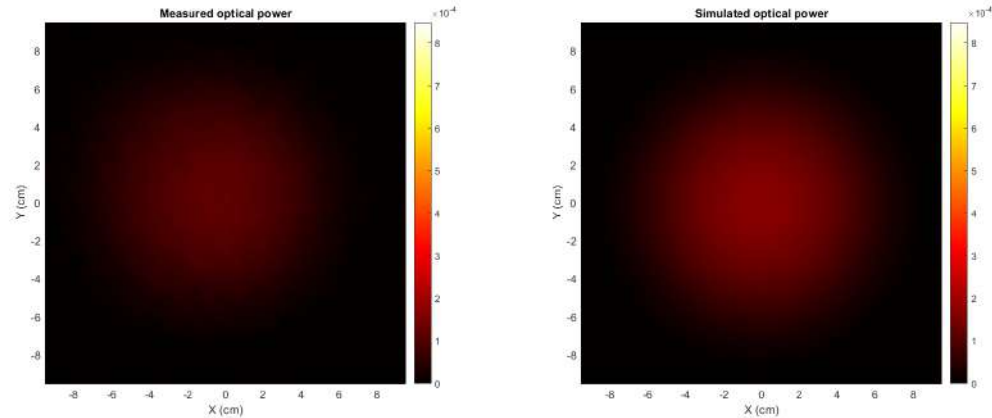Figure B.34: Comparison between the experimental and simulated power with a 41.49° occluder at 5.52 cm for the LED lamp

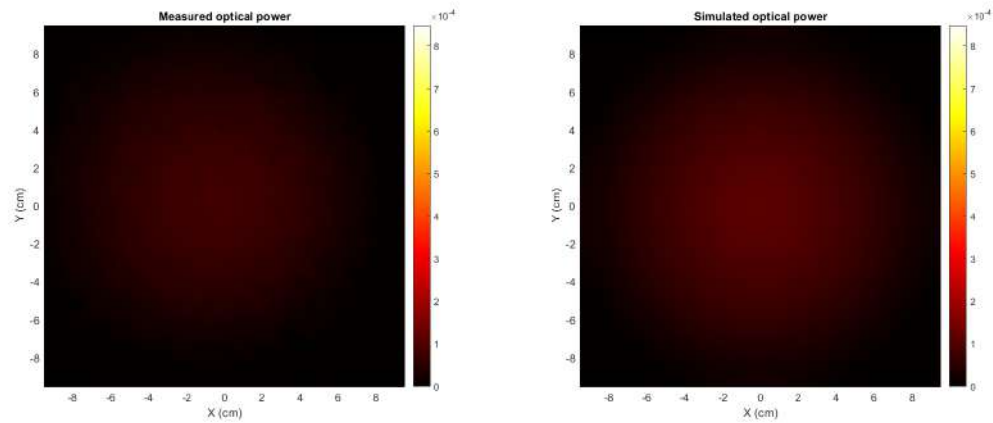Figure B.35: Comparison between the experimental and simulated power with a 41.49° occluder at 7.52 cm for the LED lamp

Figure B.36: Comparison between the experimental and simulated power with a 41.49° occluder at 9.52 cm for the LED lamp
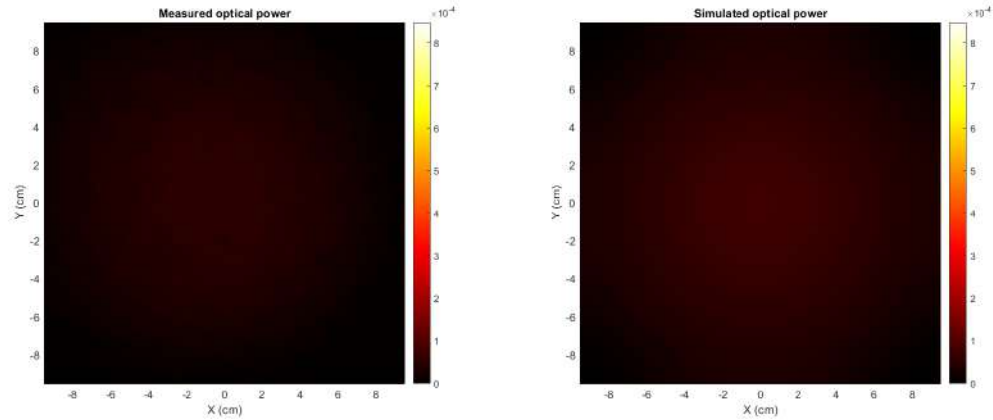

Figure B.37: Comparison between the experimental and simulated power with a 41.49° occluder at 11.52 cm for the LED lamp

B.2.4   Receiver with 23° occluder

Figure B.38: Comparison between the experimental and simulated power with a 23.52° occluder at 2.39 cm for the LED lamp

Figure B.39: Comparison between the experimental and simulated power with a 23.52° occluder at 4.39 cm for the LED lamp
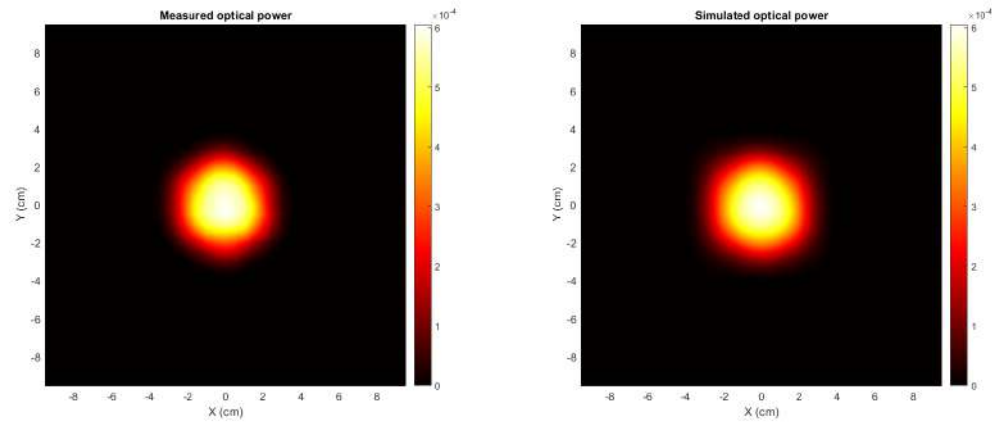
Figure B.40: Comparison between the experimental and simulated power with a 23.52° occluder at 6.39 cm for the LED lamp
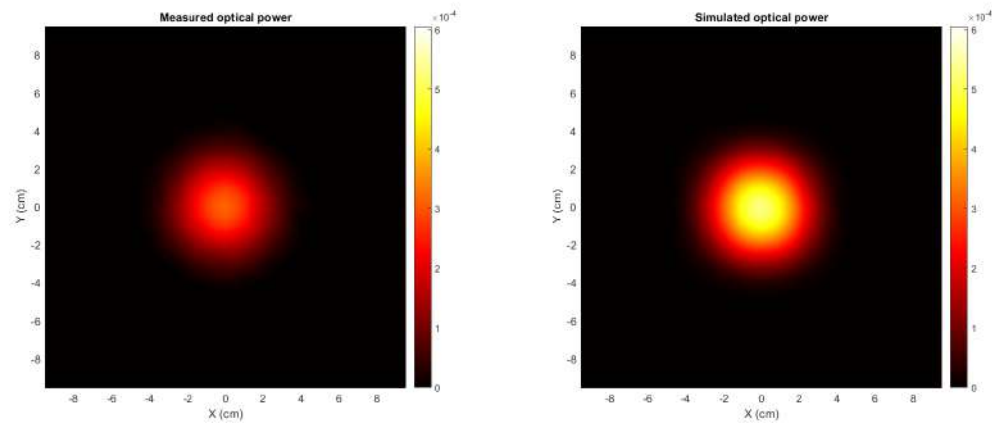

Figure B.41: Comparison between the experimental and simulated power with a 23.52° occluder at 8.39 cm for the LED lamp
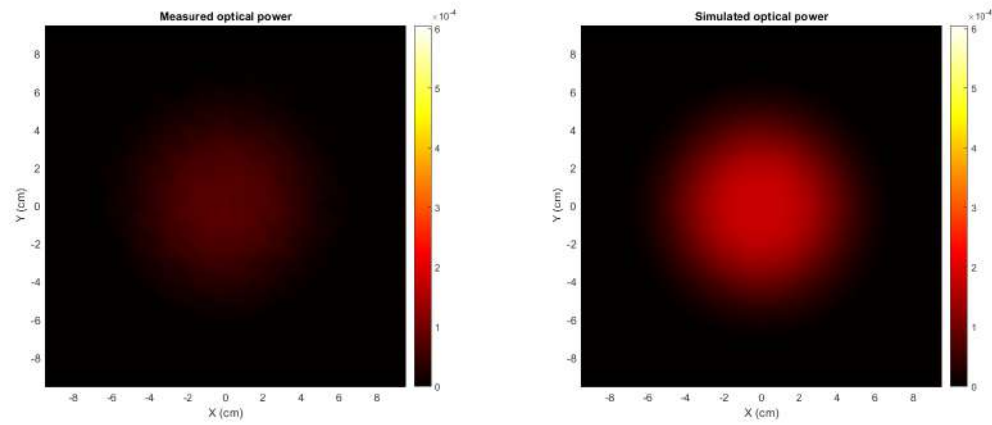
Figure B.42: Comparison between the experimental and simulated power with a 23.52° occluder at 10.39 cm for the LED lamp
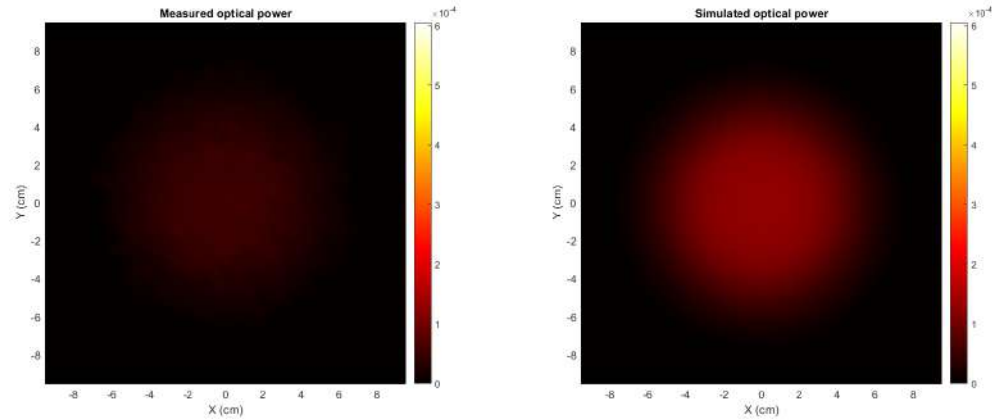
Figure B.43: Comparison between the experimental and simulated power with a 23.52° occluder at 12.39 cm for the LED lamp
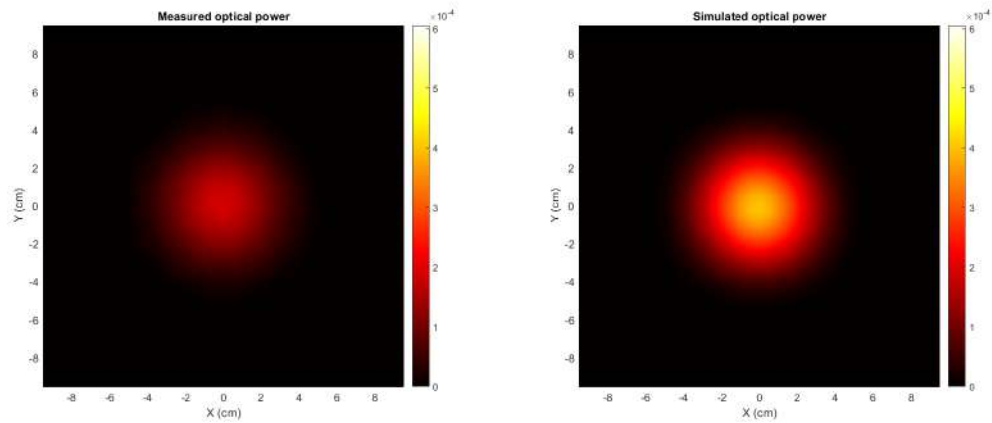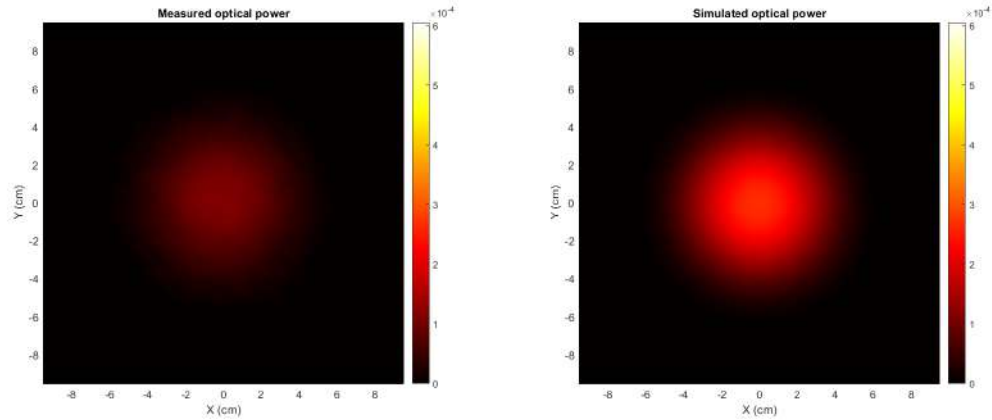
B.3   Screen with corrected occluder model

B.3.1   Receiver without occluder

Figure B.44: Comparison between the experimental and simulated power without occluder at 0.45 cm using the corrected occluder model.

Figure B.45: Comparison between the experimental and simulated power without occluder at 2.45 cm using the corrected occluder model.

Figure B.46: Comparison between the experimental and simulated power without occluder at 4.45 cm using the corrected occluder model.

Figure B.47: Comparison between the experimental and simulated power without occluder at 6.45 cm using the corrected occluder model.
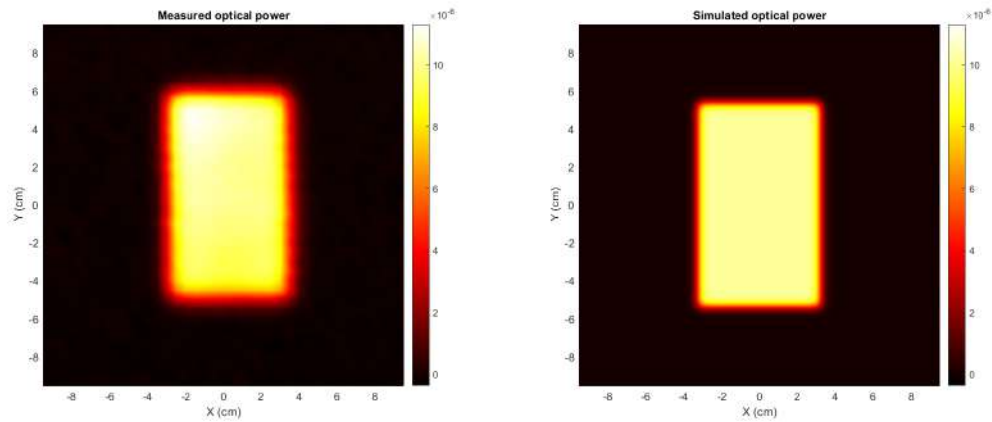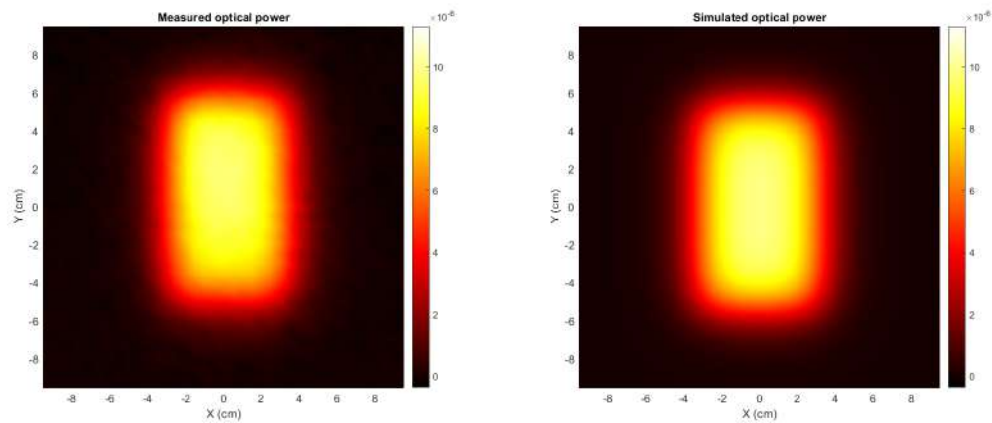
Figure B.48: Comparison between the experimental and simulated power without occluder at 8.45 cm using the corrected occluder model.

Figure B.49: Comparison between the experimental and simulated power without occluder at 10.45 cm using the corrected occluder model.

B.3.2   Receiver with 41° occluder

Figure B.50: Comparison between the experimental and simulated power with a 41.49° occluder at 1.52 cm using the corrected occluder model.

Figure B.51: Comparison between the experimental and simulated power with a 41.49° occluder at 3.52 cm using the corrected occluder model.

Figure B.52: Comparison between the experimental and simulated power with a 41.49° occluder at 5.52 cm using the corrected occluder model.

Figure B.53: Comparison between the experimental and simulated power with a 41.49° occluder at 7.52 cm using the corrected occluder model.
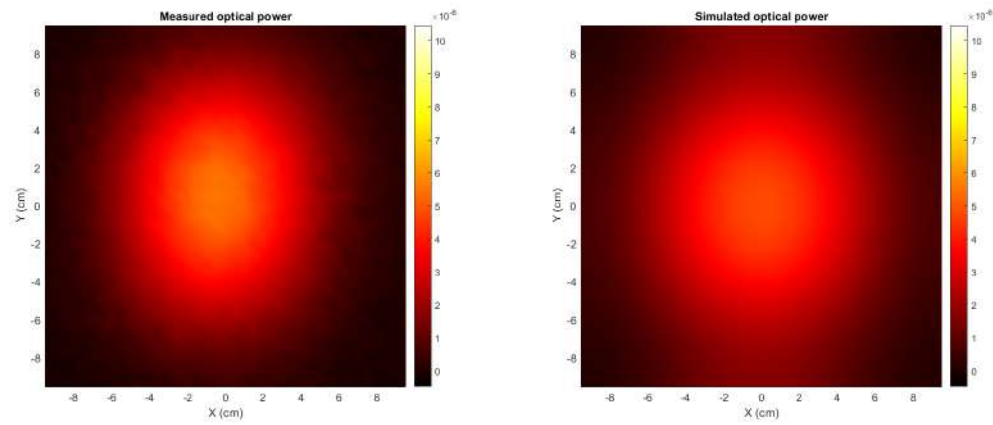
Figure B.54: Comparison between the experimental and simulated power with a 41.49° occluder at 9.52 cm using the corrected occluder model.
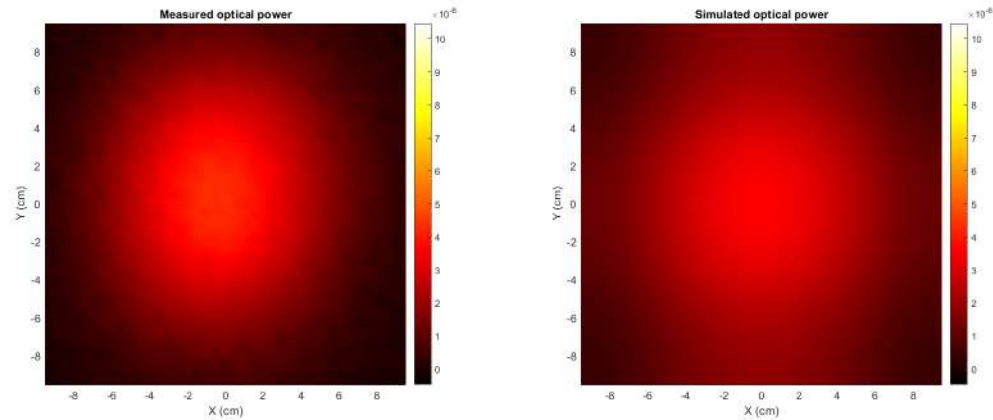
Figure B.55: Comparison between the experimental and simulated power with a 41.49° occluder at 11.52 cm using the corrected occluder model.
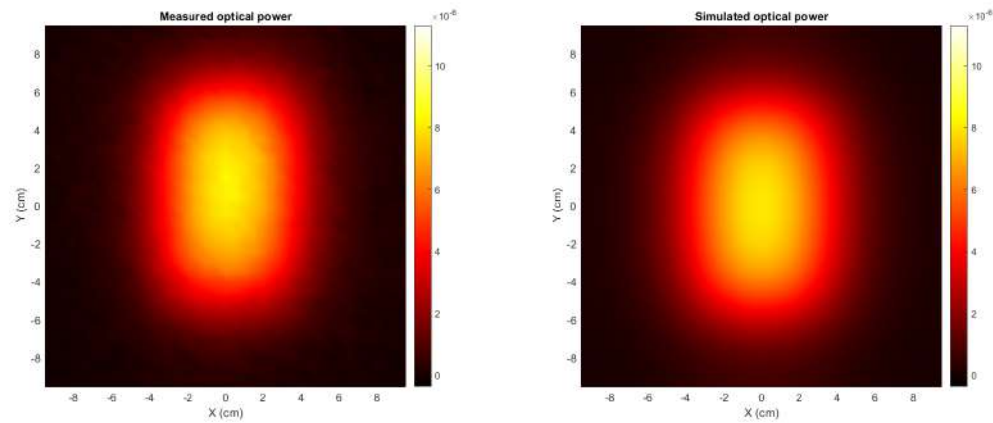
B.3.3   Receiver with 23° occluder
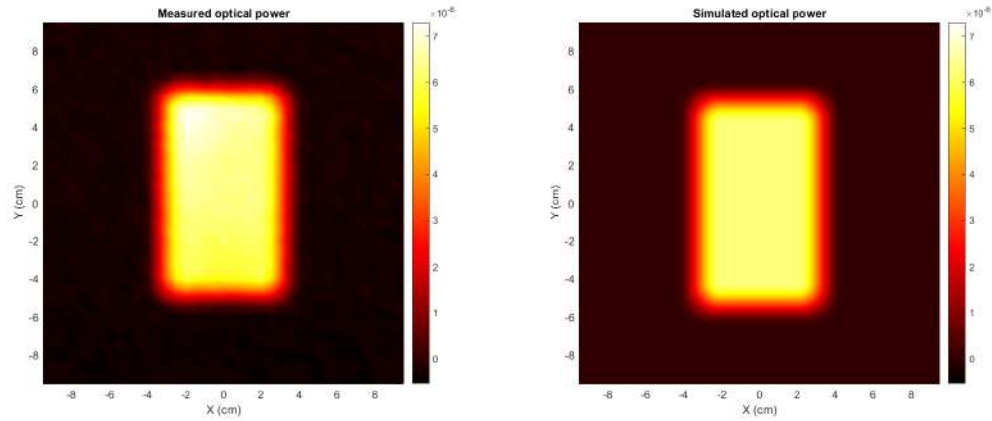
Figure B.56: Comparison between the experimental and simulated power with a 23.52° occluder at 2.39 cm using the corrected occluder model.
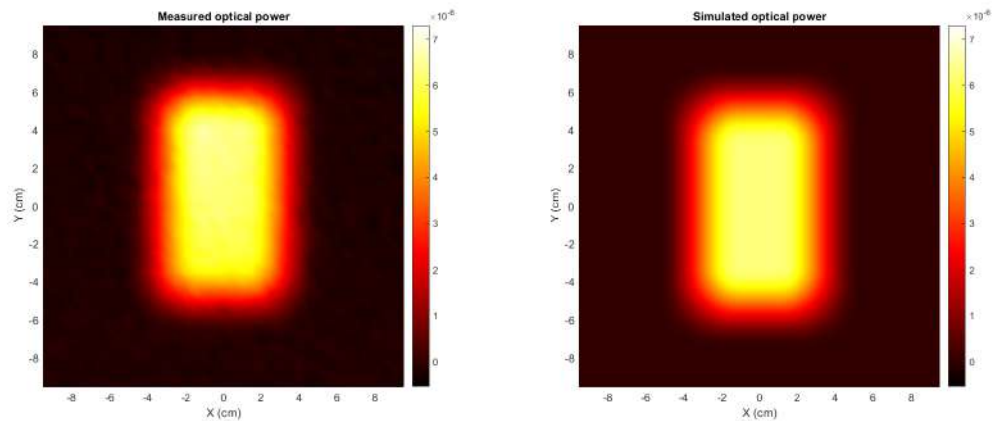
Figure B.57: Comparison between the experimental and simulated power with a 23.52° occluder at 4.39 cm using the corrected occluder model.
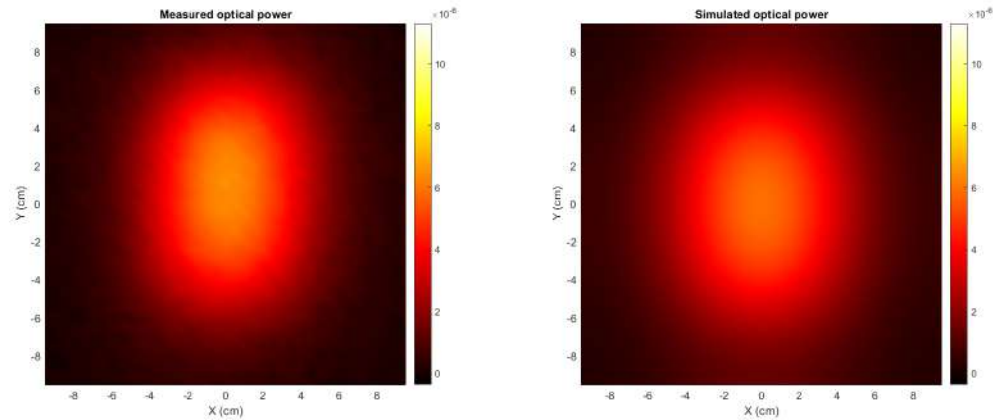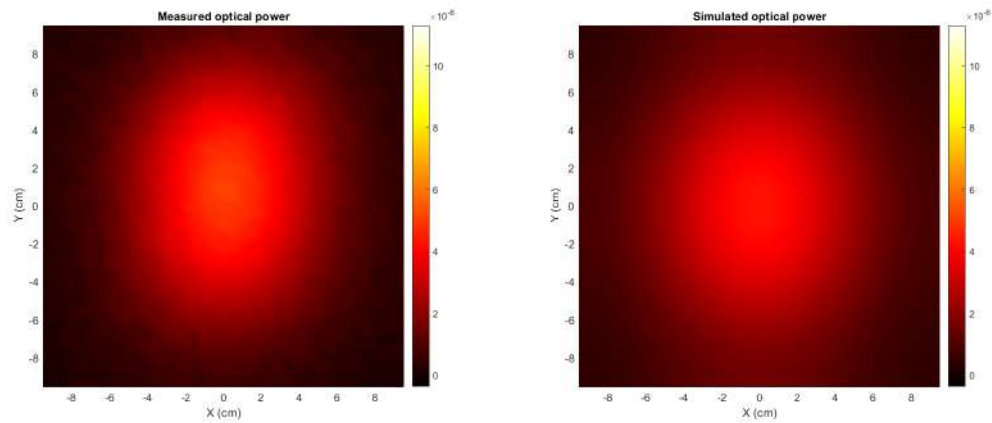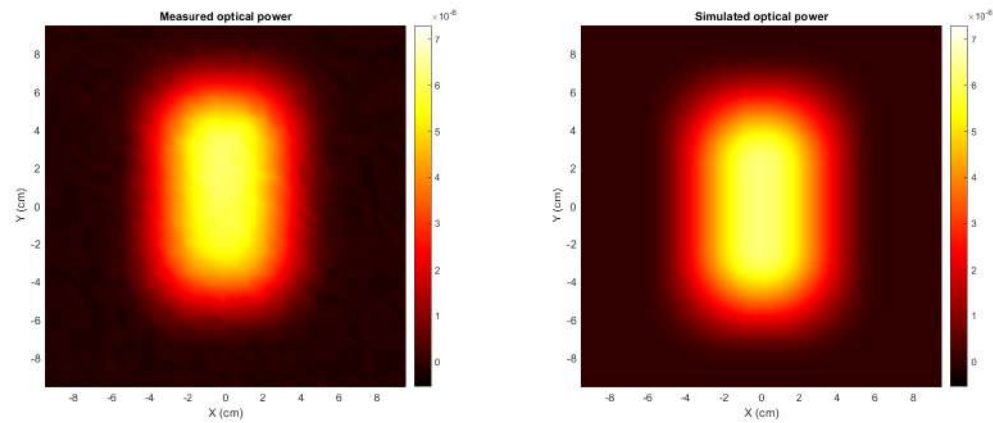
Figure B.58: Comparison between the experimental and simulated power with a 23.52° occluder at 6.39 cm using the corrected occluder model.
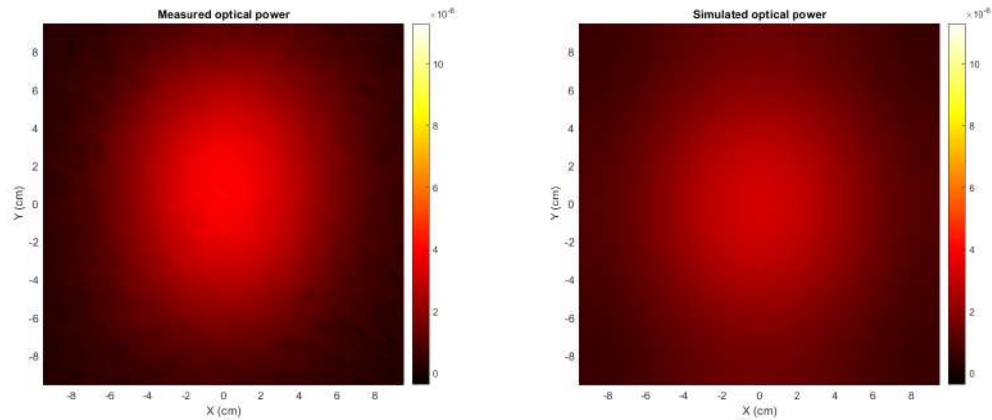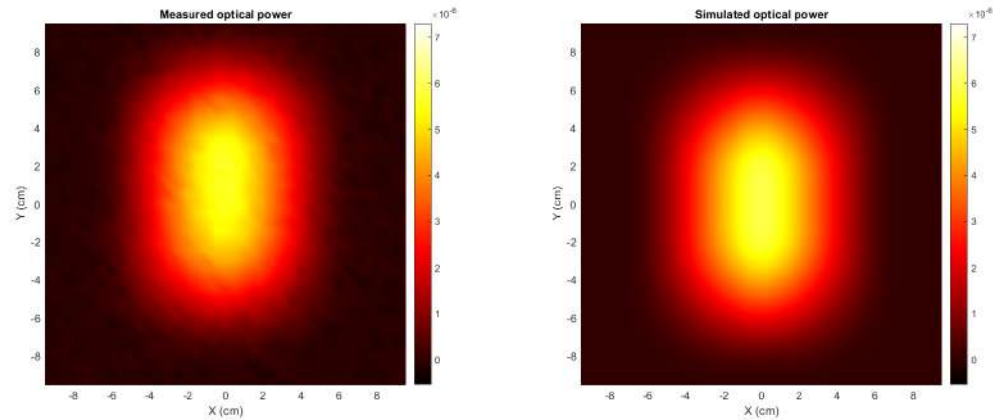

Figure B.59: Comparison between the experimental and simulated power with a 23.52° occluder at 8.39 cm using the corrected occluder model.
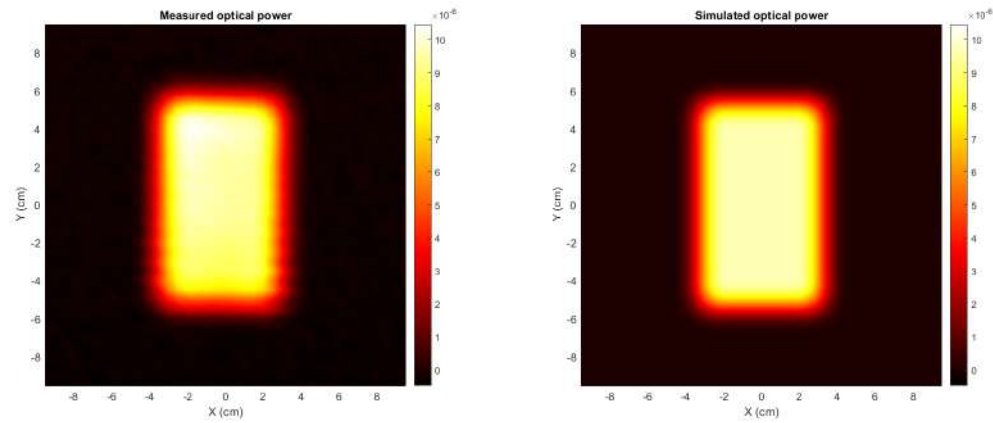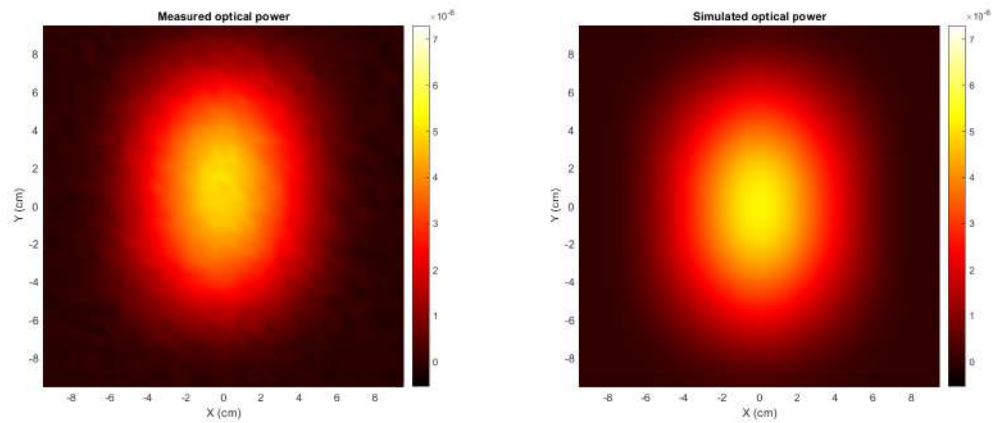
Figure B.60: Comparison between the experimental and simulated power with a 23.52° occluder at 10.39 cm using the corrected occluder model.
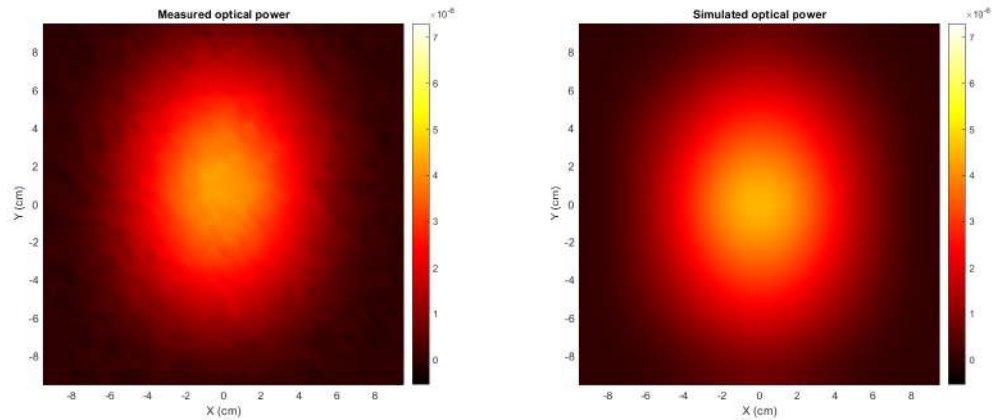
Figure B.61: Comparison between the experimental and simulated power with a 23.52° occluder at 12.39 cm using the corrected occluder model.

B.3.4   Receiver with 13° occluder
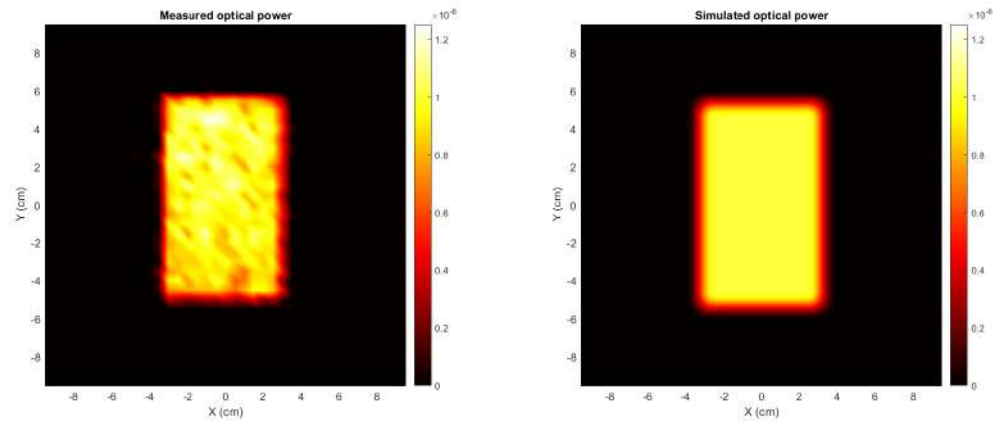
Figure B.62: Comparison between the experimental and simulated power with a 13.78° occluder at 2.39 cm using the corrected occluder model.
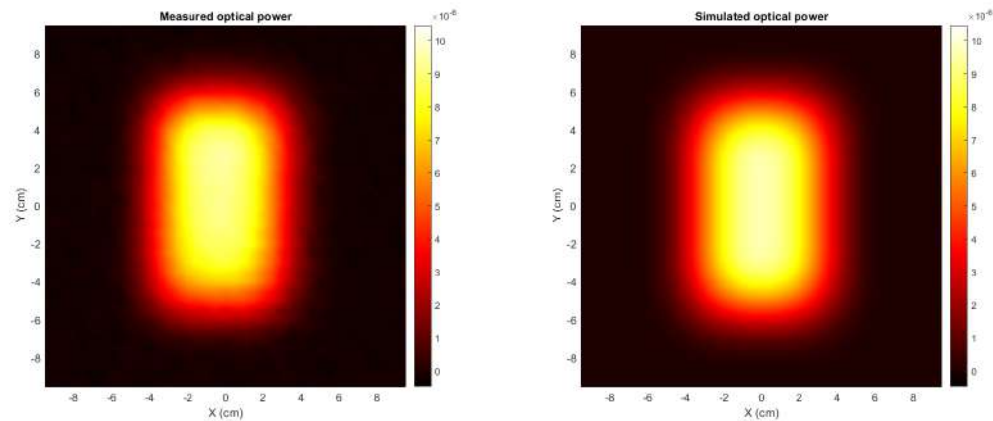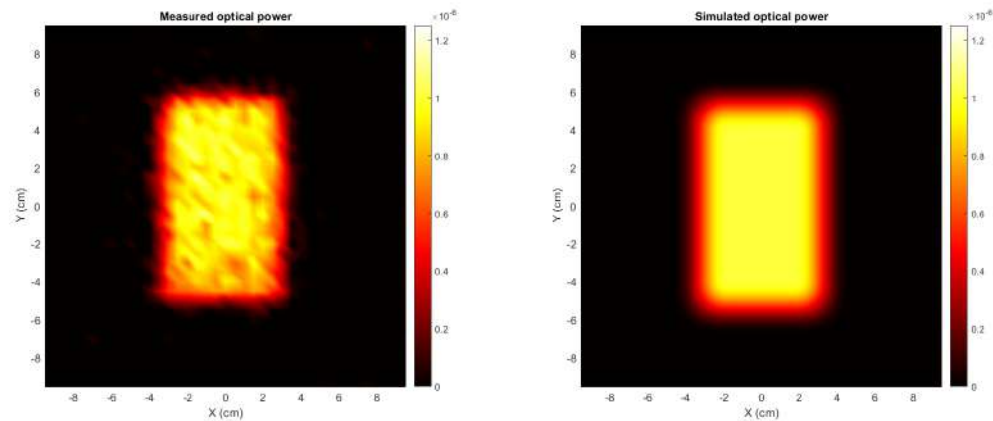

Figure B.63: Comparison between the experimental and simulated power with a 13.78° occluder at 4.39 cm using the corrected occluder model.
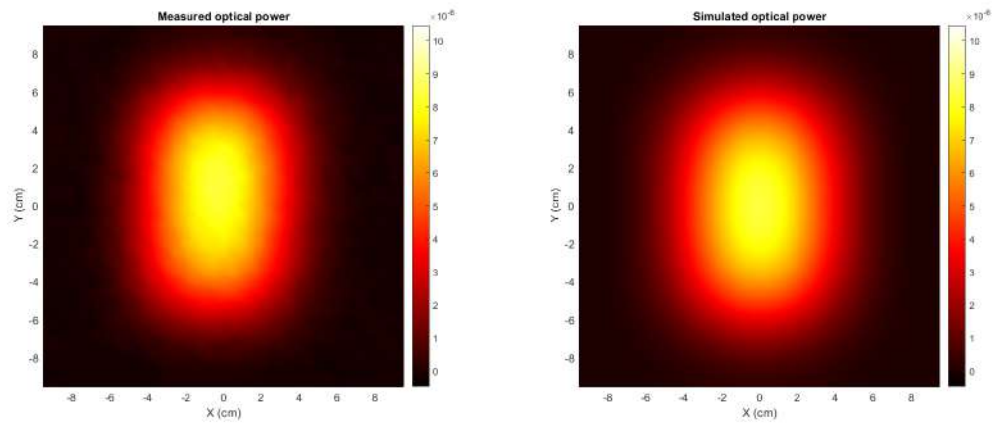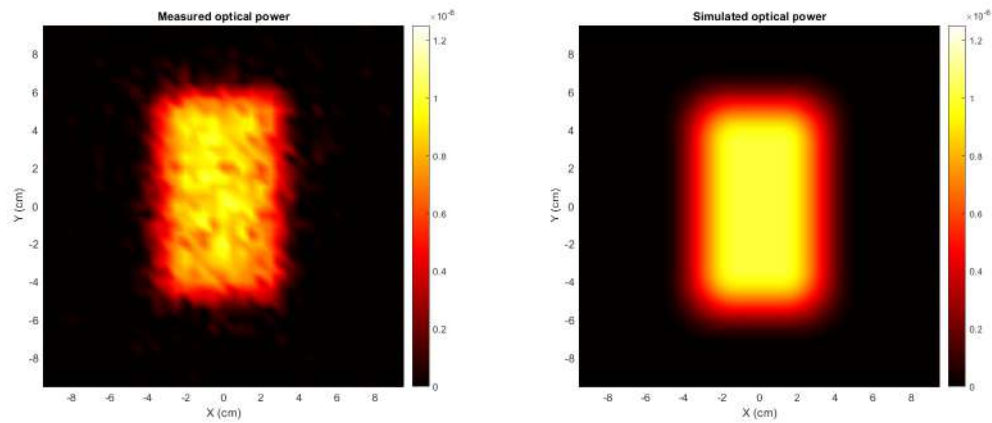
Figure B.64: Comparison between the experimental and simulated power with a 13.78° occluder at 6.39 cm using the corrected occluder model.
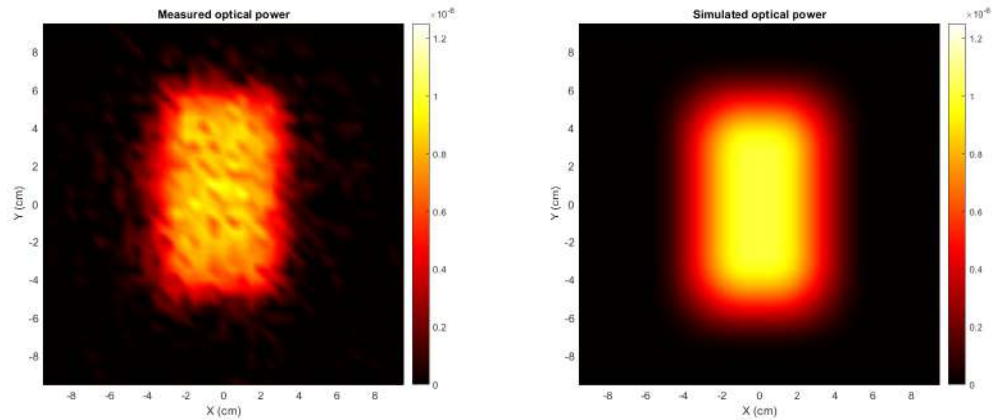
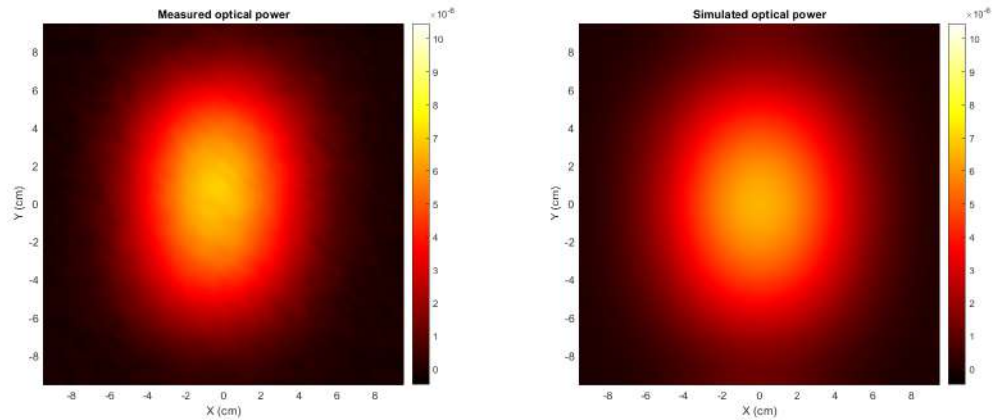
Figure B.65: Comparison between the experimental and simulated power with a 13.78° occluder at 8.39 cm using the corrected occluder model.
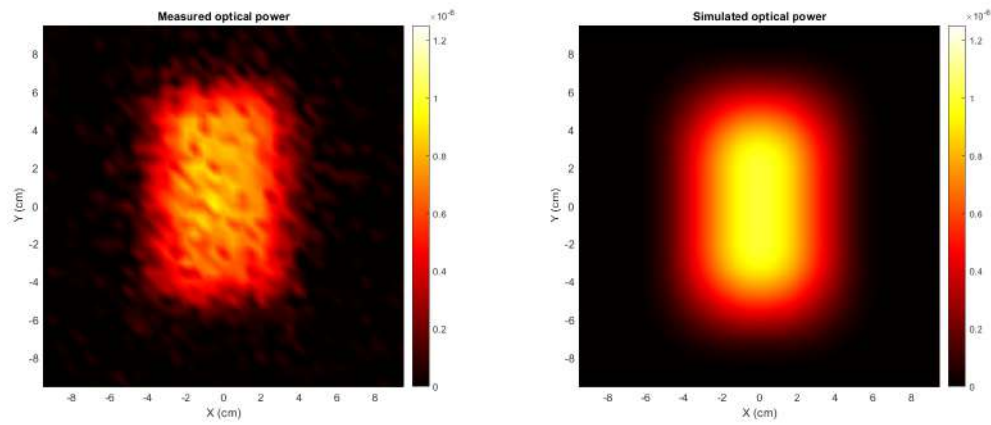
Figure B.66: Comparison between the experimental and simulated power with a 13.78° occluder at 10.39 cm using the corrected occluder model.
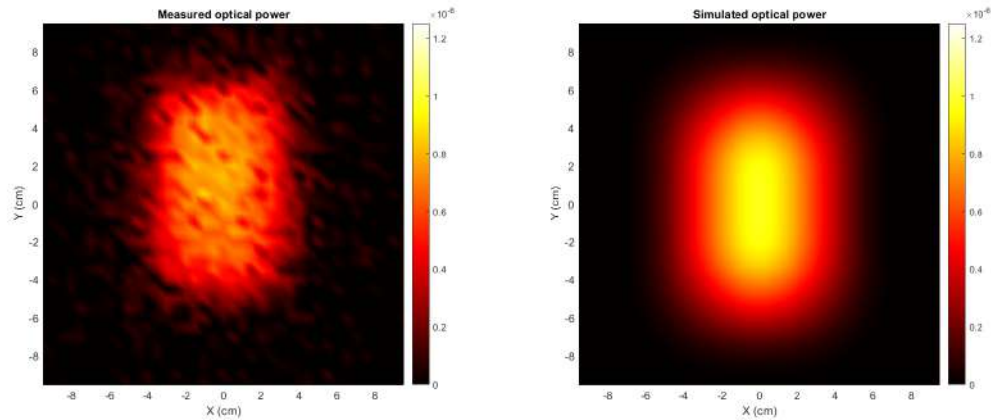
Figure B.67: Comparison between the experimental and simulated power with a 13.78° occluder at 12.39 cm using the corrected occluder model.

# Bibliography

[1] Z. Ghassemlooy, S. Zvanovec, M.-A. Khalighi, W. O. Popoola, and J. Perez, "Optical wireless communication systems," 2017.

[2] L. E. M. Matheus, A. B. Vieira, L. F. Vieira, M. A. Vieira, and O. Gnawali, "Visible light communication: concepts, applications and challenges," *IEEE Communications Surveys & Tutorials*, vol. 21, no. 4, pp. 3204–3237, 2019.

[3] S. Kumar and P. Singh, "A survey on wireless optical communication: Potential and challenges," in *Intelligent Communication, Control and Devices*, pp. 47–52, Springer, 2020.

[4] M. Z. Chowdhury, M. T. Hossan, A. Islam, and Y. M. Jang, "A comparative survey of optical wireless technologies: Architectures and applications," *IEEE Access*, vol. 6, pp. 9819–9840, 2018.

[5] T. Cevik and S. Yilmaz, "An overview of visible light communication systems," *arXiv preprint arXiv:1512.03568*, 2015.

[6] S. Kumar and P. Singh, "A comprehensive survey of visible light communication: Potential and challenges," *Wireless Personal Communications*, vol. 109, no. 2, pp. 1357–1375, 2019.

[7] I. Moreno, "Led irradiance pattern at short distances," *Applied Optics*, vol. 59, no. 1, pp. 190–195, 2020.

[8] D. Lacroix and J.-P. Javaudin, "A new channel estimation method for ofdm/oqam," in *7th International OFDM-Workshop*, 2002.

[9] B. Mielczarek and A. Svensson, "Improved iterative channel estimation and turbo decoding over flat-fading channels," in *Proceedings IEEE 56th Vehicular Technology Conference*, vol. 2, pp. 975–980, IEEE, 2002.

[10] S. F. Cotter and B. D. Rao, "Sparse channel estimation via matching pursuit with application to equalization," *IEEE Transactions on Communications*, vol. 50, no. 3, pp. 374–377, 2002.

[11] V. K. Gupta and S. Vijay, "A summative comparison of blind channel estimation techniques for orthogonal frequency division multiplexing systems.," *International Journal of Electrical & Computer Engineering (2088-8708)*, vol. 8, 2018.

[12] M. Soltani, V. Pourahmadi, A. Mirzaei, and H. Sheikhzadeh, "Deep learning-based channel estimation," *IEEE Communications Letters*, vol. 23, no. 4, pp. 652–655, 2019.

[13] O. Osemwegie, O. Obinna, O. Kennedy, and N. Nsikan, "Comparative analysis of channel estimation techniques in siso, miso and mimo systems," *International Journal of Electronics and Telecommunications*, vol. 63, no. 3, pp. 299–304, 2017.

[14] S. Fuada, A. P. Putra, and T. Adiono, "Analysis of received power characteristics of commercial photodiodes in indoor los channel visible light communication," 2017.

[15] S. Long, M.-A. Khalighi, M. Wolf, S. Bourennane, and Z. Ghassemlooy, "Channel characterization for indoor visible light communications," in *2014 3rd International Workshop in Optical Wireless Communications (IWOW)*, pp. 75–79, IEEE, 2014.

[16] F. Knobloch, "Channel gain and frame error rate for optical street lighting communication," in *2015 13th International Conference on Telecommunications (ConTEL)*, pp. 1–5, IEEE, 2015.

[17] F. Miramirkhani and M. Uysal, "Channel modeling and characterization for visible light communications," *IEEE Photonics Journal*, vol. 7, no. 6, pp. 1–16, 2015.

[18] T. Huschka, "Ray tracing models for indoor environments and their computational complexity," in *5th IEEE International Symposium on Personal, Indoor and Mobile Radio Communications, Wireless Networks-Catching the Mobile Future.*, vol. 2, pp. 486–490, IEEE, 1994.

[19] A. Gupta and P. Garg, "Statistics of snr for an indoor vlc system and its applications in system performance," *IEEE Communications Letters*, vol. 22, no. 9, pp. 1898–1901, 2018.

[20] J. Chen and T. Shu, "Statistical modeling and analysis on the confidentiality of indoor vlc systems," *IEEE Transactions on Wireless Communications*, 2020.

[21] M. A. Arfaoui, M. D. Soltani, I. Tavakkolnia, A. Ghrayeb, C. Assi, H. Haas, and M. Safari, "Snr statistics of indoor mobile vlc users with random device orientation," in *2019 IEEE International Conference on Communications Workshops (ICC Workshops)*, pp. 1–6, IEEE, 2019.

[22] Z. Zeng, M. D. Soltani, H. Haas, and M. Safari, "Orientation model of mobile device for indoor vlc and millimetre wave systems," in *2018 IEEE 88th Vehicular Technology Conference (VTC-Fall)*, pp. 1–6, IEEE, 2018.

[23] A. Srivastava, V. A. Bohara, *et al.*, "Adaptive channel estimation in vlc for dynamic indoor environment," in *2019 21st International Conference on Transparent Optical Networks (ICTON)*, pp. 1–5, IEEE, 2019.

[24] H.-S. Lee, "A photon modeling method for the characterization of indoor optical wireless communication," *Progress In Electromagnetics Research*, vol. 92, pp. 121–136, 2009.

[25] I. Moreno and C.-C. Sun, "Led array: where does far-field begin?," in *Eighth International Conference on Solid State Lighting*, vol. 7058, p. 70580R, International Society for Optics and Photonics, 2008.

[26] C.-C. Sun, W.-T. Chien, I. Moreno, C.-C. Hsieh, and Y.-C. Lo, "Analysis of the far-field region of leds," *Optics express*, vol. 17, no. 16, pp. 13918–13927, 2009.

[27] L. Svilainis and V. Dumbrava, "Led far field pattern approximation performance study," in *2007 29th International Conference on Information Technology Interfaces*, pp. 645–649, IEEE, 2007.

[28] J. Ding, Z. Xu, and L. Hanzo, "Accuracy of the point-source model of a multi-led array in high-speed visible light communication channel characterization," *IEEE Photonics Journal*, vol. 7, no. 4, pp. 1–14, 2015.

[29] I. Moreno and C.-C. Sun, "Modeling the radiation pattern of leds," *Optics express*, vol. 16, no. 3, pp. 1808–1819, 2008.

[30] A. Kumar and S. Ghorai, "Effect of led radiation pattern on ber performance in indoor multipath mimo-vlc system," *Wireless Personal Communications*, vol. 113, no. 4, pp. 2009–2026, 2020.

[31] R. Xu, H. Chen, and Z. Xu, "The near-field radiation pattern of an oled panel and its application in detection," in *2018 11th International Symposium on Communication Systems, Networks & Digital Signal Processing (CSNDSP)*, pp. 1–6, IEEE, 2018.

[32] H. Chen and Z. Xu, "Oled panel radiation pattern and its impact on vlc channel characteristics," *IEEE Photonics Journal*, vol. 10, no. 2, pp. 1–10, 2017.

[33] I. Moreno, M. Avendaño-Alejo, and R. I. Tzonchev, "Designing light-emitting diode arrays for uniform near-field irradiance," *Applied optics*, vol. 45, no. 10, pp. 2265–2272, 2006.

[34] J. Tan, K. Yang, M. Xia, and Y. Yang, "Analysis of uniform illumination system with imperfect lambertian leds," *Opt. Appl*, vol. 41, no. 3, pp. 507–517, 2011.

[35] I. Moreno, "Design of led spherical lamps for uniform far-field illumination," in *Fifth Symposium Optics in Industry*, vol. 6046, p. 60462E, International Society for Optics and Photonics, 2006.

[36] I. Moreno, J. Muñoz, and R. Ivanov, "Uniform illumination of distant targets using a spherical light-emitting diode array," *Optical Engineering*, vol. 46, no. 3, p. 033001, 2007.

[37] Z. Su, D. Xue, and Z. Ji, "Designing led array for uniform illumination distribution by simulated annealing algorithm," *Optics express*, vol. 20, no. 106, pp. A843–A855, 2012.

[38] R. Wu, Z. Zheng, H. Li, and X. Liu, "Optimization design of irradiance array for led uniform rectangular illumination," *Applied optics*, vol. 51, no. 13, pp. 2257–2263, 2012.

[39] S. Pal, "Optimization of led array for uniform illumination over a target plane by evolutionary programming," *Applied optics*, vol. 54, no. 27, pp. 8221–8227, 2015.

[40] I. Moreno, "Image-like illumination with led arrays: design," *Optics Letters*, vol. 37, no. 5, pp. 839–841, 2012.

[41] J. C. Valencia-Estrada, B. Béchadergue, and J. García-Márquez, "Full field radiant flux distribution of multiple tilted flat lambertian light sources," *IEEE Open Journal of the Communications Society*, vol. 1, pp. 927–942, 2020.

[42] E. Rosencher, *Optoelectronics*. Cambridge University Press, 2002.

[43] A. C. Parr, *Optical Radiometry*. Elsevier, 2005.

[44] Beer, "Bestimmung der absorption des rothen lichts in farbigen flüssigkeiten," *Annalen der Physik*, vol. 162, no. 5, pp. 78–88, 1852.

[45] A. Figà-Talamanca and M. A. Picardello, "Spherical functions and harmonic analysis on free groups," *Journal of Functional Analysis*, vol. 47, no. 3, pp. 281–304, 1982.

Glossary

amplitude The scalar magnitude of a periodical signal, determines the peak value that the signal takes in one period.. 3

carrier Monochromatic signal that propagates through a medium, it is modulated in order to transport information between points in the medium.. 3

channel coding Addition of redundant symbols in order to increase the robustness of a code against a noisy channel.. 1

communication channel Mathematical abstraction of the means by which an emitter sends information to a receiver.. 2, 5, 15

communication process The series of actions involved in the correct delivery of information from an emitter to a receiver.. 1, 2

communication system The set of elements used to execute a succesfull communication process.. 1–5

electromagnetic spectrum The set of all the possible frequencies of an electromagnetic wave.. 3

encryption The process of applying an encoding to some information in order to hide it from receivers that are not allowed to access it.. 1

exitance Distribution of the radiated power at every point in the surface of the source.. 12, 14, 28

far field Region of space where the electromagnetic field generated by a source behaves as a radiated wave. In OWC, it is sometimes considered to be the region of space where a source can be considered a point source.. 9

Fourier transform Projection of a signal into a complex exponential base.. 5

impulse response Dynamical behaviour of the output of a system when an impulse excitation is introduced, in LTI systems it fully characterizes its behaviour.. 4, 5

information source Entity that generates symbols at a certain rate and with a given probability distribution.. 1

information user Entity that can benefit from the knowledge of the symbols generated by a source.. 1

instantaneous phase The phase of an analytic signal.. 3

instantaneous power The rate of energy passing through a system per unit time. It corresponds to the square of the modulus of a signal modelling the flowing magnitude.. 3

irradiance The radiant flux incident to a surface per unit area.. 9

lambertian source Source whose radiance is constant.. 9

manifold Topological space that is locally similar to an euclidean space.. 6, 79

modulation Process of modification of the properties of a carrier signal in order to transport some information between points.. 3

monge coordinate Local parametrization of a manifold where one of the variables is a function of the remaining variables.. 16, 17, 19, 22

near field Region of space where non-radiative phenomena cannot be neglected. In OWC, near field implies, among othe things, that the geometry of the source affects the behaviour of the link.. 5, 6, 9

network Set of interconnected systems that share information.. 2

optical source System that emits electromagnetic radiation in the optical spectrum.. 4–6, 9, 10, 12, 14, 16

oscilloscope Electronic instrument that allows to graphically display time-varying voltage signals.. 53

photodetector System that transforms an incident optical power into an electrical current as predicted by the photoelectric effect.. 4, 11, 43

photodiode Diode with an optical active region where incident photons are converted into electrons.. 15, 32–34, 40, 42, 43, 47, 53, 54

radiance Ratio of power flux per solid angle and per projected area.. 5, 11, 12

radiation pattern Dimensionless function that represents how radiated energy from a source is distributed along every spatial direction.. 9, 10, 12

random variable Function that assigns a value to the result of a random experiment.. 54

receiver System that captures the energy of incoming signals and outputs symbols (after demodulating, decrypting and decoding).. 4, 6

reliability Quantitative characterization of the degree of consistency of a set of calculations or specifications.. 2

source coding Process of assignment of codes to the symbols of an information source.. 1

transmitter Device that transforms symbols from an information source into signals that are emitted through a medium.. 5

wavelength Spatial length of a complete oscillation of a wave. It is related to the frequency and the phase velocity of the wave.. 4, 11, 13, 15

Acronyms

AI Artificial Intelligence. 9

AoA Angle of Acceptance. 31, 36, 43, 45

AoV Angle of View. 45, 47, 56, 72, 73

ASK Amplitude-Shift Keying. 4

DoF Degrees of Freedom. 74

FFT Fast Fourier Transform. 26

FoV Field of View. 72

FSOC Free Space Optical Communications. 4

IM/DD Intensity Modulation / Direct Detection. 4, 11

LED Light Emitting Diode. xiii, 9, 10, 45, 59, 65, 66, 72, 73, 81

LiDAR Light Detection And Ranging. 4

LiFi Light Fidelity. 4

MIMO Multiple Input Multiple Output. 9, 36

MISO Multiple Input Single Output. 9

NLoS Non-Line of Sight. 5

OCC Optical Camera Communications. 4, 27, 74

OFDM Orthogonal Frequency Division Multiplexing. 4

OLED Organic Light Emitting Diode. 10

OOK On-Off Keying. 4

OWC Optical Wireless Communications. 4–6, 8–10, 27, 34, 73

RF Radiofrequency. 4

SISO Single Input Single Output. 9

V2V Vehicle-to-Vechicle. 4

VLC Visible Light Communications. 4, 8, 9

VLP Visible Light Positioning. 27

WDM Wavelength Division Multiplexing. 4

WLAN Wireless Local Area Network. 4

Budget

The budget can be divided into human resources costs and material costs.

Human resources costs

According to the retribution table of the ULPGC, a project technician under the TCP4 category will cost 35,5952 euros per hour of work. The duration of this project has been of 300 hours. The total human resources costs amount to 10678,56 euros.

Material resources costs

The following hardware equipment has been used in the development of the project

- Personal Computer: 750,00 euros

- InfiniiVision MSO7034A oscilloscope: 5785,15 euros

- Robo3D R1+ 3D printer: 420,00 euros

- PDA36A-EC photodiode: 270,91 euros

- Cables and other laboratory equipment: 100 euros

The total cost of the material resources amounts to 7326,06 euros

Total cost of the project

The total cost of the project, considering human and material resources amounts to **eighteen thousand and four euros and sixty two cents**.

Specifications

The veracity of the obtained data can only be guaranteed by the use of the same set of instruments and configurations, as well as exactly the same control algorithms. If those specifications are not met, there could exist discrepancies of the experimental results with the data exposed in this document. On the other hand, the operation of the optical receivers and emitters used could be altered by the changes of climate conditions, so that similar results can only be expected in regions where the climate conditions are similar to those in Las Palmas de Gran Canaria.